Global atmospheric CO_2 distributions from satellite observations

by

Dorit M. Hammerling

A dissertation submitted in partial fulfillment
of the requirements for the degree of
Doctor of Philosophy
(Environmental Engineering)
in The University of Michigan
2012

Doctoral Committee:

Associate Professor Anna M. Michalak, Chair
Professor Christopher S. Ruf
Associate Professor Christian M. Lastoskie
Senior Scientist Brian J. Thelen

To the OCO and GOSAT instrument teams

ACKNOWLEDGEMENTS

First of all, I thank my advisor Professor Anna Michalak for her manifold support and inspirational guidance throughout the completion of this dissertation. I sincerely appreciate the exciting research opportunities that were offered to me, and the intellectual freedom that I was given in their pursuit. This line of research has truly become my passion.

I further thank my committee members Professor Christian Lastoskie, Professor Christopher Ruf, and Dr. Brian Thelen for their encouragement and valuable comments.

It has been a great pleasure to be part of the PUORG research group, and I thank the group's current and former members for much valuable collaboration and input.

I am thankful to Randy Kawa, Chris O'Dell, Dave Crisp, Scott Doney, Gregg Marland, Kevin Schaefer, and to many other individuals at CSU, JAXA, JPL, NASA, NCAR, NIES, and other institutions for our scientific collaboration, sharing of information and data, and their valuable advice.

I am grateful to Amy Braverman, Noel Cressie, Matthias Katzfuss, Douglas Nychka, Richard Smith, and many other individuals in the statistics community for insightful discussions.

I thank Mario Bonk for countless hours of excellent editorial help; man dankt!

Finally, I am deeply indebted to my family, my partner and my friends for their immeasurable support and their loving and inspiring presence in my life.

TABLE OF CONTENTS

LIST OF FIGURES

Figure

CHAPTER I

Introduction

Given its potentially severe consequences, including an increase in extreme weather events, rising sea levels and accompanying displacement of people, climate change is one of the largest challenges facing mankind. The leading cause of anthropogenic climate change is the increasing concentration of carbon dioxide (CO_2) in the atmosphere resulting from anthropogenic CO_2 emissions [e.g. *American Meteorological Society*, 2012; *Solomon et al.*, 2007], which have been steadily rising since the Industrial Revolution [e.g. *Olivier et al.*, 2012; *Peters et al.*, 2011]. A mitigating factor has been the fact that less than half of these emissions have remained in the atmosphere, with the majority of the CO_2 released from anthropogenic emissions being taken up again by physical and biogeochemical processes partaking in the carbon cycle [e.g. *Field et al.*, 2007; *Peters et al.*, 2011]. Were it not for these uptake mechanisms, the concentrations of atmospheric CO_2 in the atmosphere would have risen even faster, and subsequently the effects of climate change would be much more severe [e.g. *Denman et al.*, 2007]. There are, however, some indications that these uptake mechanisms might be weakening and a higher percentage of emitted CO_2 might be remaining in the atmosphere [*Canadell et al.*, 2007b; *Le Quéré et al.*, 2009]. We lack detailed quantitative information of where uptake of carbon takes place, what the relative contribution of different processes to the carbon exchange is, and how sus-

tainable uptake processes will be in the future. This lack of quantitative knowledge of carbon exchange processes, of their future functioning and their climate feedbacks, is one of the main sources of uncertainty in future climate projections [e.g. *Friedlingstein et al.*, 2006] and limits our ability to optimally manage and mitigate climate change. This dissertation presents arguments and methodologies, which establish how high resolution geostatistical mapping of newly available satellite CO_2 observations can enhance our knowledge of global atmospheric CO_2 concentrations, and how this enhanced characterization of the concentration fields can indirectly contribute to a better understanding of the underlying carbon fluxes which give rise to the gradients in atmospheric CO_2 concentrations.

Current approaches to infer carbon sources and uptake ("sinks"), and hence quantify carbon exchange processes, include inverse modeling ("top-down"), process-based surface modeling and inventory based calculations ("bottom-up"). Inverse modeling describes procedures where atmospheric CO_2 observations are used in combination with atmospheric transport models to infer carbon fluxes, whereas process-based models are models that are based on our understanding of carbon exchange processes [e.g. *Field et al.*, 2007; *Huntzinger et al.*, 2012]. There are large differences in the modeled flux distribution between top-down and bottom-up approaches and also among models using the same approach [*Battin et al.*, 2009; *Gurney et al.*, 2008]. The carbon cycle is a highly complex, dynamical system, consisting of a broad variety of processes [e.g. *King et al.*, 2007]. Many of these processes occur at widely different temporal and spatial scales, and partially compensate each other in terms of overall carbon fluxes [e.g. *King et al.*, 2007]. These scale discrepancies and the potential compensating effect of fluxes from different processes, contribute to the challenge of quantifying carbon fluxes, which is reflected in the spread of modeling results mentioned above. Another cause for these discrepancies is a lack of observational data that would allow us to better constrain these models and improve the underlying model formulation and

parameterization [*Nisbet and Weiss*, 2010]. While the ground-based atmospheric CO_2 measuring network has been growing, it is still rather limited and heavily weighted towards measurement locations in developed countries [*Tans and Conway*, 2005].

Space-based observations of CO_2 offer the prospect of providing observations at much higher global density than the ground-based network. To provide such observations, Japan and the United States have commissioned the first two satellite missions specifically designed for the measurement of greenhouse gases including CO_2. A defining feature of these two missions is their sensitivity to the near-surface CO_2 concentrations, where most of the carbon exchange processes take place. The Japanese Greenhouse Gas Observing Satellite (GOSAT) was successfully launched in January 2009, while NASA's Orbiting Carbon Observatory (OCO) [*Crisp et al.*, 2004] experienced a launch failure in 2009 and will be re-launched as OCO-2 in 2015.

A future mission, which is in planning stage, is the Active Sensing of CO_2 Emissions over Nights, Days and Seasons (ASCENDS) mission. The term "active" refers to the measurement technology employed, which is based on lidar technology, where the instrument itself emits and receives light. Passive missions such as GOSAT and OCO-2, on the other hand, infer the amount of CO_2 in the atmosphere by means of reflected sunlight. This eliminates the opportunity to observe at night, in cloudy regions and at low solar zenith angles, i.e. at high latitudes; circumstances in which active missions will in principle still be able to observe. The mission goals of ASCENDS are hence linked to contributing insights to open carbon cycle questions that will specifically benefit from the lidar measurement technology. These questions include changes in the Northern High Latitude and the Southern Ocean [*ASCENDS Workshop Steering Committee*, 2008], which are both are among the largest and most vulnerable carbon pools. More broadly, it is anticipated that ASCENDS, and other active missions, will provide a more comprehensive set of global observations and might improve inversion results [*Hungershoefer et al.*, 2010].

The current and future availability of satellite observations of CO_2, however, is no panacea for pinning down the carbon cycle. One aspect is that, while the spatial coverage of satellite data is large compared to the land-based CO_2 monitoring network, the daily spatial coverage is still relatively sparse [e.g. *Buchwitz et al.*, 2007; *Schneising et al.*, 2008] with gaps due to orbit configuration and measurement limitations such as clouds and aerosols. In a recent article on the role of OCO and GOSAT, the potential of monthly atmospheric CO_2 maps to serve as benchmarks for models and to provide insights in seasonal carbon cycle dynamics has been pointed out [*Heimann*, 2009]. Monthly atmospheric CO_2 maps, compared to, for example, weekly or daily maps, were mentioned by *Heimann* [2009], as a temporal resolution of one month is considered the achievable status quo due to gaps in the satellite data. Some characteristics of satellite observations, namely that they are instantaneous in time without frequently reoccurring measurements at the same location, and that they often occur in clusters and have high measurement errors, have further proven challenging for inversions [*Hungershoefer et al.*, 2010].

This dissertation presents a novel and complementary approach to capitalize on CO_2 satellite observations; the satellite observations are employed to map global atmospheric CO_2 concentration fields with associated uncertainties at high spatial and temporal resolution. Temporal resolution is a critical factor as it determines which types of insights can be gained from, and what types of subsequent studies can be conducted with, the inferred concentration fields. Ideally, the inferred concentration fields feature a temporal resolution similar to the dynamics of atmospheric CO_2, which is on the order of a few days. If such high resolution concentration fields can be inferred, they can be used in a wide variety of subsequent studies to gain direct knowledge about the atmospheric CO_2 concentration fields at synoptic time scales, as well as indirectly to gain knowledge about carbon sources and sinks. Examples demonstrated in this dissertation include model comparison and carbon flux signal

detection studies. In this context, model comparison refers to studies that assess the degree to which transport and flux models are consistent with observation-based CO_2 concentration fields. Signal detection refers to studies that assess the ability of observing systems to detect gradients in atmospheric CO_2 concentrations, which result from carbon flux perturbations.

The mapping approach presented in this thesis has certain advantages compared to the mapping approaches that are currently in use and that are described in detail in section 2.5.1. The current mapping approaches do not use the information content of the satellite observations to their full potential by either applying averaging procedures in binning approaches that eliminate high resolution information or by combining the information content of the satellite observations with flux and transport modeling assumptions, which render it difficult to distinguish the origins of the signals contained in the resulting products. This in turn limits the ability to use these products as validation data sets or in model comparisons.

The approach taken in this dissertation is to conceptualize and model global atmospheric CO_2 concentrations as a realization of a stochastic process or random field [e.g. *Cressie*, 1993; *Gelfand*, 2010]. A stochastic process is characterized by the presence of statistical correlation. In the application to CO_2 concentration fields, this translates to spatial correlation. The basic idea is to leverage the fact that spatial correlation is present in the CO_2 concentration field, and hence in the observations, to infer, and map, global concentration fields using a geostatistical framework without invoking flux estimates or transport modeling assumptions. Using a geostatistical framework also naturally leads to uncertainties along with the concentration fields.

Geostatistical mapping draws a balance between using only the observations on one hand and modeling approaches that invoke flux and transport assumptions on the other hand; it infers observation-derived mapping products based on spatial correlation. The main challenges associated with using individual satellite observations

directly in, for example, model comparison studies are that they contain large gaps and their measurement noise levels are very high. The existence of large gaps implies that comparisons can not be conducted in a spatially comprehensive way using the observations directly. The high measurement errors lead to uncertainties associated with individual observations that are often so large that they preclude meaningful comparisons that could provide new insights. Geostatistical mapping has the advantage that it can leverage the information content from many observations simultaneously and can thereby provide spatially continuous concentration fields with uncertainties that are often lower than those of the observations, which in turn facilitates potentially more insightful comparisons.

In summary the goal of the method developed in this dissertation is to obtain atmospheric CO_2 concentration maps that are not based on flux estimates or atmospheric transport models, can be created at synoptic time scales and provide uncertainties. Once derived, these maps and their uncertainties can be used to gain insights in the carbon cycle through a variety of subsequent studies. To this end, this thesis has three main objectives: 1) Developing and evaluating a mapping methodology for deriving global atmospheric CO_2 concentrations and uncertainties from satellite observations, 2) Deriving high resolution CO_2 concentration maps from GOSAT observations and using the mapped products for model comparison studies and 3) Evaluating the ability of the ASCENDS mission to detect signals in atmospheric CO_2 concentrations resulting from changes in carbon fluxes.

Objective 1: High resolution mapping of CO_2

The objective is to develop a methodology to infer CO_2 concentrations, and associated uncertainties, at high spatial and temporal resolution without invoking flux or atmospheric transport assumptions. The conceptual idea is to leverage the spatial correlation present in the atmospheric CO_2 concentration field by employing a spatial

statistical framework to infer atmospheric CO_2 concentration maps and uncertainties at high spatial and temporal resolution. This objective also addresses the specific question of the optimal temporal resolution to create such maps, which is explored by means of a simulation study. The simulation study uses highly realistic OCO-2-like observations, which will represent an interesting challenge as their precision will be relatively high, but the spatial coverage for a given day will be limited. So making optimal use of future OCO-2 observations requires a careful evaluation of the choice of temporal resolution. In addition to addressing the question of optimal temporal resolution, the simulation study assesses the performance of the mapping methodology for a range of conditions, such as varying levels of measurement noise and seasonal variations in the spatial and temporal heterogeneity of the CO_2 concentration fields.

Objective 2: Global GOSAT CO_2 maps and model comparison

The objective is to derive the global GOSAT CO_2 concentration maps at high spatial and temporal resolution with uncertainties to gain knowledge about the synoptic scale changes in the CO_2 concentration field and to assess to which degree the GOSAT-derived concentration fields are consistent with a state-of-the-art coupled carbon flux and transport model. The time period considered is the second half of 2009, the first time period for which GOSAT observations are available. The model used in the model comparison is the PCTM/GEOS-5/CASA-GFED model and the methodology developed in objective 1 is used to infer the global concentration fields. The comparison is conducted using a probabilistic framework, which takes the spatially and temporally varying uncertainties of the GOSAT-derived mapped concentrations into consideration. In addition to assessing the consistency between the PCTM/GEOS-5/CASA-GFED model with the mapped GOSAT products, the objective is to also provide a prototype application of a probabilistic comparison study using mapping products.

Objective 3: Signal detection for the ASCENDS mission

The objective is to assess the capability of the ASCENDS mission to detect gradients in atmospheric CO_2 concentrations resulting from changes in carbon fluxes whose detection is of high scientific and societal relevance. The specific proto-typical scenarios investigated are: carbon release from the melting of permafrost in the high Northern latitudes, the shifting of fossil fuel emissions from Europe to China and El Nino Southern Oscillation (ENSO) related changes in the sources/sink characteristics in the Southern Ocean. These scenarios fall within the key ASCENDS mission goals and can specifically benefit from the ASCENDS measurement technology. The detection study applies the methodology developed in objective 1 to create mapping products that are then used in a probabilistic comparison framework for signal detection. Using mapping products in a signal detection setting can potentially lead to better detection performance than using individual high noise observations as the information content of many observations can be leveraged concurrently. Besides investigating to which degree the ASCENDS mission can detect changes in gradients in the atmospheric CO_2 concentration field stemming from changes in carbon fluxes, this objective also provides an illustration how mapping can be advantageously used for signal detection.

CHAPTER II

Background

2.1 Anthropogenic climate change

Our climate is changing; it is getting warmer, and quickly so. The global temperature of the Earth has increased by 0.8 degrees in the last century, with more than half of the increase occuring in the last thirty years [*Blunden and Arndt*, 2012]. Further observational evidence of a changing climate includes an increase in global averaged ocean temperature, rising global averaged sea levels and decreasing global volumes of snow and ice [*American Meteorological Society*, 2012].

Along with an increase in global temperature, other characteristics of our climate, such as weather patterns and the occurences of extreme events, as well as circulation patterns in the atmosphere and in the oceans are also showing signs of change [*Trenberth et al.*, 2007]. Some of the consequences, we are already seeing evidence for, are more frequent extreme events such as severe storms and droughts [e.g. *American Meteorological Society*, 2012; *Trenberth et al.*, 2007]. Another example includes changes in snow accumulation in mountainous areas. Although there are regional variations, in most locations freezing elevations have gone up and the onset of spring melting occurs earlier, leading to lower levels of winter snow pack and subsequently less spring runoff, which affects downstream water supplies [*American Meteorological Society*, 2012; *Lemke et al.*, 2007]. The polar regions are some of the areas most

affected by climate changes [*American Meteorological Society*, 2012]. Arctic sea ice extent has been shrinking for the last few decades [*Lemke et al.*, 2007], setting a new record low in 2012 (http://nsidc.org/arcticseaicenews/2012/08/arctic-sea-ice-breaks-2007-record-extent/). The Greenland and Antarctica ice sheets have lost a significant portion of their volumes [*American Meteorological Society*, 2012]. In addition, most of the world's glaciers are retreating [e.g. *American Meteorological Society*, 2012; *Lemke et al.*, 2007]. This melting of snow and ice has contributed to about half of the sea level rise over the last decades, with the other half due to thermal expansion of the water in the oceans [*American Meteorological Society*, 2012]. Sea level rise has severe impacts on coastal areas, where the majority of the world's population lives [*Nicholls et al.*, 2007].

While there is natural variability in the Earth's climate, there is broad consensus in the scientific community that the climate change we are experiencing now is, at least in part, brought about by human actions [e.g. *American Meteorological Society*, 2012; *Denman et al.*, 2007]. The key drivers of anthropogenic climate change are the increasing concentrations of greenhouse gases in the atmosphere. The Fourth Assessment of the Intergovernmental Panel on Climate Change specifically states that "most of the observed increase in global average temperatures since the mid-20th century is very likely due to the observed increase in anthropogenic emissions" [*IPCC*, 2007]. The anthropogenic greenhouse gases include carbon dioxide, methane, nitrous oxides, among others. Of these, carbon dioxide and methane are the largest contributors to climate change and their concentrations are increasing due to human activities, mainly the burning of fossil fuels and land use changes (e.g. deforestation) [e.g. *Peters et al.*, 2011]. Their increasing concentrations cause a higher percentage of the earth's outgoing thermal radiation to be absorbed and re-radiated, which leads to an increase in global temperature [e.g. *Forster et al.*, 2007].

Of all the greenhouse gases in the atmosphere, carbon dioxide (CO_2) is the most

important anthropogenic greenhouse gas contributing to climate change [e.g. *Forster et al.*, 2007]. In addition to its role as a greenhouse gases, atmospheric CO_2 is in exchange with, and influences, other components of the Earth System. For example, higher atmospheric concentrations of CO_2 have led to increased absorption of CO_2 by the oceans, which subsequently causes ocean acidification [e.g. *Field et al.*, 2011]. Ocean acidification refers to a reduction in the pH of the oceans over an extended period. The rapidly evolving field of ocean acidification research is just starting to attribute the effects of increasing atmospheric CO_2 concentrations on ocean chemistry, and the subsequent impact on biological processes and ecosystems in the oceans such as coral-reef systems [e.g. *Field et al.*, 2011]. Ocean organisms that form their shells using aragonite, a form of calcium carbonate, might be at the risk of extinction, as projections indicate that they will be unable to form their shells in a more acidic ocean [e.g. *Field et al.*, 2011]. Furthermore, more acidic oceans can put ecosystem services, such as fisheries and tourism, at risk. Another example of a direct influence of increasing atmospheric CO_2 concentrations is carbon fertilization, defined as the enhancement of the growth of plants as a result of increased atmospheric CO_2 concentrations [e.g. *Canadell et al.*, 2007a]. One of the effects of carbon fertilization is a change in the relative competitive advantage of plants species [e.g. *Michalak et al.*, 2011], which could have a variety of consequences ranging from effects on the world's food supply to loss of species.

While anthropogenic CO_2 emissions have been rising since the Industrial Revolution [e.g. *Peters et al.*, 2011], only about half of these emissions have remained in the atmosphere [e.g. *Denman et al.*, 2007]. The remainder of the anthropogenic CO_2 emissions have historically been taken up again by so-called carbon sinks; mainly the oceans and the land biosphere [e.g. *Peters et al.*, 2011]. This uptake, however, varies significantly from year to year, and our understanding is limited to what causes these inter-annual variations [e.g. *Field et al.*, 2007; *King et al.*, 2004]. Some of the factors

that contribute to the interannual variability include changes in fossil fuel emissions, natural variability in climate and weather patterns, fires and volcanic eruptions. For example, it has been shown that interannual variability is correlated with the occurence of El Nino/Southern Oscillation (ENSO) [*Gurney et al.*, 2008]. However, many fundamental questions about the driving mechanisms and the resulting carbon fluxes remain open [e.g. *Michalak et al.*, 2011; *Pacala et al.*, 2007b]. We do not know in enough detail what the driving mechanisms are, how large the resulting carbon fluxes are, and how they vary, on regional scales. Our lack of detailed understanding of the driving mechanisms is reflected in the fact that one of the largest factors contributing to the uncertainty in the prediction of future climate is the future of carbon sinks [e.g. *Friedlingstein et al.*, 2006]. Given our limited mechanistic and quantitative understanding, it is not certain how these uptake mechanisms will function in the future, and most importanly, if they will continue to provide the removal service they currently do [e.g. *Pacala et al.*, 2007b]. If these removal services became less efficient, climate change would be accelerated and its effects much more severe [e.g. *Denman et al.*, 2007].

Carbon sinks are but one component in the complex dynamical system of exchange and transformation of carbon within the Earth System referred to as the carbon cycle, which is discussed in the following section. The behavior of carbon sinks can only be fully understood, and quantified, in the larger context of a quantitative understanding of the carbon cycle within the Earth system.

2.2 The Global Carbon Cycle and its characterization

The global carbon cycle is the biogeochemical cycle by which carbon is exchanged and transformed among different carbon reservoirs, namely the atmosphere, biosphere, geosphere, hydrosphere, pedosphere, and human systems of the Earth [*King et al.*, 2007]. The global carbon cycle is a highly complex dynamical system consist-

ing of many components. The quantitatively largest exchanges occur between the atmosphere and the oceans and between the atmosphere and the terrestrial biosphere [e.g. *King et al.*, 2004, 2007].

The oceans constitute, after the lithosphere, the second largest reservoir of carbon in the Earth System, holding about 50 times as much carbon as the atmosphere [e.g. *Denman et al.*, 2007; *King et al.*, 2004; *Prentice et al.*, 2001]. Both physical and biogeochemical processes, mainly ocean circulation and carbonate chemistry, contribute to the ocean carbon exchange [e.g. *Prentice et al.*, 2001]. Carbon enters the ocean primarily through dissolution of atmospheric CO_2 in the top layer of the ocean, with a much smaller contribution from dissolved organic carbon that enters the ocean through river discharge [e.g. *Prentice et al.*, 2001].

The physical carbon exchange is driven, among other factors, by the partial pressure difference of CO_2 between air and water and the solubility of CO_2, which is a function of ocean temperature [e.g. *Prentice et al.*, 2001]. Ocean phytoplankton converts dissolved inorganic CO_2 to organic matter via photosynthesis [*Prentice et al.*, 2001]. Some of the dissolved carbon is also converted to calcium carbonate shells [e.g. *King et al.*, 2007]. When these organisms die, they sink and decay, during which most of the carbon is redissolved, but a small fraction reaches the sediments of the deeper oceans, thereby sequestering carbon for long time periods [e.g. *King et al.*, 2007]. This process is referred to as the biological pump [*Prentice et al.*, 2001].

The oceans have acted as a net carbon sink since the increase of atmospheric CO_2 concentrations in the last two and a half centuries, as the rate of exchange with the top layer of the ocean is driven by the atmosphere-ocean difference in partial pressure of CO_2 [e.g. *Denman et al.*, 2007; *Prentice et al.*, 2001]. With increasing CO_2 concentrations, however, the fractional rate of uptake declines due to a reduced buffer capacity of the ocean carbonate system and the limited rate of mixing between deep ocean and surface water [*Prentice et al.*, 2001]. Increasing ocean water temper-

atures further contribute to a reduction in uptake due to lower solubility of CO_2 with increasing temperature [*Prentice et al.*, 2001].

The key processes that characterize the carbon exchange in the terrestrial biosphere are related to vegetation and microbial organisms. Through photosynthesis, plants convert atmospheric carbon into organic carbon. About half of this organic carbon is stored in wood and other plant tissue [e.g. *King et al.*, 2007], while the other half is converted back to atmospheric CO_2 during plant respiration. When plants die and decay, most of the stored carbon is released again to the atmosphere [e.g. *Denman et al.*, 2007]. A very small fraction is converted to inert forms and amasses in the soil [e.g. *King et al.*, 2007; *Prentice et al.*, 2001]. Fires and the transfer of soil carbon back to the atmosphere through heterotrophic respiration, i.e. the mineralization of organic carbon to CO_2 by microbes [e.g. *Canadell et al.*, 2007a], further influence the carbon exchange between the terrestrial biosphere and the atmosphere [e.g. *Denman et al.*, 2007]. A range of human-influenced processes modify the natural terrestrial biospheric exchange processes. Key such modifications include CO_2 fertilization, woody encroachment, reforestation, change in agricultural practices,the melting of permafrost and the subsequent release of carbon, drainage of peatlands, deforestation and fires [*Canadell et al.*, 2007a; *Field et al.*, 2007; *King et al.*, 2007]. They can be roughly categorized in processes directly influenced by human activities such as land use change related processes, and those indirectly influenced by humans via the effects of climate change such as CO_2 fertilization and the melting of permafrost.

While the mechanisms of some of terrestrial carbon exchange processes are reasonably well known, it is not clear what the relative contributions of these processes are to carbon exchange in a given region [e.g. *Field et al.*, 2007]. Having a quantitative understanding of the processes contributing to carbon exchange is especially important when evaluating the future direction of carbon exchange in the region. For

example, the sink contribution of reforestation is limited in space and time and will eventually taper off, which needs to be accounted for accordingly when assessing future sinks [e.g. *Pacala et al.*, 2007b]. Hence, understanding the relative importance of these driving processes, and evaluating their future functioning, are key objectives in carbon cycle science. One aspect that makes a quantitative description of the individual processes contributing to the carbon cycle difficult is that only the net difference in fluxes can be observed. So even though the gross carbon flux associated with a given carbon exchange mechanism might be large, the net difference in fluxes from all processes contributing to carbon exchange combined is small in many ecosystems as the fluxes partially compensate each other. This renders it difficult to assess the contributions of individual flux processes.

In addition to human activities that modify natural carbon exchange processes, anthropogenic emissions, mainly from the burning of fossil fuels, play an important role in the carbon cycle. The flux associated with fossil fuel emissions is relatively small compared to the gross fluxes associated with natural oceanic and terrestrial exchange processes, approximately 9 Pg carbon per year compared to approximately 90 Pg and 57 Pg associated with oceanic and terrestrial exchange [e.g. *Field et al.*, 2007]. However, the net contribution of fossil fuel emissions is large and fossil fuel emissions are the main driver for increasing CO_2 concentrations in the atmosphere [e.g. *Solomon et al.*, 2007]. Fossil fuel emissions have been rising since the onset of the Industrial Revolution reaching their highest level yet in 2011 with global emissions of approximately 9.3 Pg of carbon [*Olivier et al.*, 2012]. While fossil fuel emissions vary to some degree in response to economic conditions [e.g. *Olivier et al.*, 2012; *Peters et al.*, 2011], their average annual increase over the last two decades was 3% [*Olivier et al.*, 2012]. Were this trend to continue, achieving the widely cited target of limiting maximum global warming to 2 degrees, seems unattainable [*Olivier et al.*, 2012].

The carbon cycle is also inter-related with the nitrogen and the hydrological cy-

cles, the Earth system's two other main cycles. A climate-relevant example of an interaction between the carbon and the hydrological cycle is that observations now indicate that rising atmospheric CO_2 concentrations have led to increased globally averaged water vapor in the atmosphere, which in turn amplifies warming of the earth [*American Meteorological Society*, 2012]. One factor that adds to the complexity of the carbon cycle is that different carbon exchange processes happen at vastly varying scales [e.g. *Denman et al.*, 2007]; spatial scales range from the oceans to individual small organisms, temporal scales from millions of years to quasi-instantaneous. Scale also plays a role in assessing how well-understood components of the carbon cycle are. Carbon fluxes of individual entities, such as trees, might be well understood, but how to use this understanding to upscale to local and regional scales remains challenging [*Canadell et al.*, 2007a]. Eddy covariance towers, which infer CO_2 fluxes, have led to much progress in the understanding of the role and seasonal behavior of different ecosystems [e.g. *Pacala et al.*, 2007a]. However, the spatial range of fluxes that can be observed by eddy covariance towers is limited, and, analogous to process-based understanding, it has been challenging to upscale the findings to larger regional scale [*Field et al.*, 2007].

Complementary to direct carbon flux measurements, other approaches to assess the carbon exchange include inventory calculations, inverse or top-down modeling using atmospheric CO_2 concentrations and process-understanding based models. [*Field et al.*, 2007]. Inventory calculations are based on assessments of carbon stocks contained in various carbon reservoirs, such as forest inventories and measurements of carbon in the oceans, and their change over time. Inverse modeling uses atmospheric CO_2 observations in conjunction with a transport model to estimate carbon fluxes. Process-based models are numerial models that are based on our understanding of carbon exchange processes. They vary widely with respect to the number of processes incorporated, their level of detail and resolution, and the use of observational

constraints [e.g. *Huntzinger et al.*, 2012]. In residual calculations a flux component is calculated as the difference between estimated total net flux and estimates of other flux components [e.g. *Field et al.*, 2007]. Reconciling the findings using different approaches has proven challenging. This challenge is manifested in the large differences of regional flux estimates that exist between process-understanding based models and those using atmospheric CO_2 observations to infer carbon fluxes [e.g. *Battin et al.*, 2009]. Even using only the top-down modeling approaches, where observations of atmospheric CO_2 concentrations are used to infer carbon fluxes, results show wide spreads [e.g. *Baker et al.*, 2006; *Gurney et al.*, 2008].

In addition to uncertainties associated with the contribution of individual driving mechanisms to carbon exchange, the state of knowledge of fluxes over larger regions varies by region. Carbon exchange between the oceans and the atmosphere is generally known fairly accurately, with the exception of the Southern Ocean [e.g. *Gruber et al.*, 2009]. The large uncertainties in the Southern Ocean, primarily caused by a lack of observations, have led to large differences in the assessment of the temporal trend of the carbon sink in the Southern Ocean, and subsequently in its future projection [*Gruber et al.*, 2009; *Le Quéré et al.*, 2007]. Land areas where carbon flux estimates have very large uncertainties are the tropics and the Northern hemisphere extratropics [*Baker et al.*, 2006; *Gurney et al.*, 2003]. The coastal regions, where land and oceans interface, are also areas where large uncertainties remain in our understanding of carbon exchange [e.g. *Pacala et al.*, 2007b].

Besides direct flux measurements, in a complex, interlinked dynamical system such as the carbon cycle many different types of observations can contribute to further our understanding of the system. Observations that can directly or indirectly contribute to improving our understanding of the carbon cycle cover a broad range and include observations of the oceans, of atmospheric constituents, properties and dynamics, earth surface characteristics and their interactions, characteristics of the terrestrial

biosphere such as leaf area index (LAI) and other vegetation indices, properties of the hydrological cycle as well as variables describing solar dynamics and subsequent changes in incoming radiation [e.g. *Solomon et al.*, 2007]. Observing these properties can help improve our process-understanding by characterizing the variability of the observed system component and their effect on carbon fluxes. To successfully do that, the observations need to be made at a temporal and spatial resolution that is high enough to capture the variability of the component in time and space. For some processes this is most effectively done as part of field campaigns where a variety of observations are taken for a limited duration with the goal of improving our process understanding of the system component. The final goal is to advance scientific understanding and potentially incorporate the improved characterization of a system component in models.

2.3 Observations of atmospheric CO_2

Observations of atmospheric CO_2 hold a unique position among all the indirect observations of carbon fluxes; they reflect the net result of all carbon exchange processes with the atmosphere. For instance, the global net sum of all the carbon exchange processes with the atmosphere over a time period is captured in the change of the global mean in concentrations over the same time period. It is not the mean, but the spatial and temporal gradients in the atmospheric CO_2 concentrations, however, that contain the information that enables inference on the spatial and temporal distribution of the carbon fluxes. Inferring carbon fluxes at high spatial and temporal resolution, i.e. knowing how carbon fluxes vary over small regions and time periods, is an important step towards disentangling the relative contributions of various carbon exchange processes. Ideally, inventory-based and process-based methods work in conjunction with methods based on atmospheric concentrations, where the atmospheric methods provide a constraint and verification tool for the other methods [e.g. *Pacala*

et al., 2007b]. The ultimate goal is to understand carbon exchange processes at scales that will enable us to assess the future contribution of these exchange processes, and to make carbon cycle management decisions.

The following sections discuss atmospheric CO_2 observations, and their use to enhance our understanding of the carbon cycle, in more detail. Given the subject of this dissertation, the discussion will be geared towards satellite observations of atmospheric CO_2 concentrations.

Observations of atmospheric CO_2 exist in many forms including discrete flask, continuous tower, aircraft, ship, and satellite observations. The most iconic observations are arguably those from the Mauna Loa observatory in Hawaii, which were started by C. David Keeling in 1958 and constitute the longest record of direct measurements of CO_2 in the atmosphere [*Keeling et al.*, 1976]. These various types of observations all have their unique characteristics, which often suggest in which type of subsequent study they are used.

2.3.1 Ground-based and airborne observations of atmospheric CO_2

One feature that is common to all the atmospheric CO_2 observations described in this section is that they are accurate and precise, especially compared to satellite observations of atmospheric CO_2 [e.g. *Chevallier et al.*, 2009; *Nassar et al.*, 2011]. While the number of ground-based and airborne observation sites has been steadingly increasing, the global spatial coverage of these observations is still sparse. In addition, the distribution of the observation locations is far from uniform. Most of the observation sites are located in North America and Europe, and coverage is limited in the Southern hemisphere, and is especially sparse in South America and Africa (for a summary of observation locations see the webpage of the World Data Center for Greenhouse Gases: http://ds.data.jma.go.jp/gmd/wdcgg/).

The longest-operating of the ground-base networks is the Carbon-Cycle Green-

house Gases (CCGG) cooperative air sampling network, which is directed by the National Oceanic and Atmospheric Administration (NOAA). It was started in 1967 and today represents an international network which includes regular discrete samples from the NOAA baseline observatories, cooperative fixed sites, and commercial ships (http://www.esrl.noaa.gov/gmd/ccgg/flask.html). Other in situ tower networks of atmopsheric CO_2 observations have since emerged in North America, Brazil, Europe, Japan and Australia and are operated by various entities (an overview of most of these networks and their data products is available at the World Data Center for Greenhouse Gases: http://ds.data.jma.go.jp/gmd/wdcgg/). These networks provide continuous observations of atmospheric CO_2.

Atmospheric CO_2 measurements are also obtained from aircrafts. An example is the Comprehensive Observation Network for Trace Gases by Airliner (CONTRAIL) [e.g. *Machida et al.*, 2008]. The CONTRAIL project measures atmospheric CO_2 concentrations covering altitudes between the earths surface to the lower stratosphere at latitudes between the boreal high latitudes to the austral mid-latitudes [*Machida et al.*, 2008]. NOAA also conducts aircraft observations at different sites in North American at regular intervals. Aircraft observations have been used in numerous studies of vertical variation and transport of CO_2 [e.g. *Stephens et al.*, 2007], and for the validation of inverse and carbon cycling modeling results [e.g. *Tiwari et al.*, 2006] as well as the validation of satellite observations [e.g. *Chevallier et al.*, 2009].

Another observing network is the Total Carbon Column Observing Network (TCCON), a network of ground-based Fourier Transform Spectrometers (FTS) that record direct solar spectra in the near-infrared. From these spectra, column-averaged abundances of a variety of atmospheric constituents including CO_2 are retrieved. FTS are remote-sensing instruments, and therefore fundamentally different than the other observations described in this section. Satellite observations of atmospheric CO_2 also observe column averages and, for that reason, FTS observations are well suited for

the validation and calibration of satellite observations. The limited extent of the network (there are currently 18 stations worldwide) has led to very few studies using the TCCON observations directly to characterize global carbon fluxes or atmospheric concentrations [*Chevallier et al.*, 2011], while most published research utilizes the TCCON observations of CO_2 for the validation of satellite observations [e.g. *Crisp et al.*, 2012; *Thompson et al.*, 2012].

2.3.2 Satellite observations of atmospheric CO_2

The measurement of atmospheric CO_2 concentrations by satellites is a fairly recent endeavor. The first two satellite missions dedicated to measuring greenhouse gases, including CO_2, were the Greenhouse Gas Observatory (GOSAT) launched in January 2009 [e.g. *Yokota et al.*, 2009] and the Orbiting Carbon Observatory (OCO) [e.g. *Crisp et al.*, 2004], which failed at launch in February 2009. In addition, atmospheric CO_2 distributions are inferred from satellite measurements that were not originally intended to measure CO_2. These include the Scanning Absorption Spectrometer for Atmospheric Chartography (SCIAMACHY), the Atmospheric Infrared Sounder (AIRS), the Tropospheric Emission Spectrometer (TES) and the Infrared Atmospheric Sounding Interferometer (IASI). CO_2 satellite missions in planning stages include OCO-2 [e.g. *Boland et al.*, 2009], the replacement satellite for OCO, and the Active Sensing of CO_2 Emissions over Nights, Days, and Seasons (ASCENDS) mission, among others.

Satellite observations of CO_2 are based on the fact that CO_2 molecules absorb energy at known frequencies of the electro-magnetic spectrum. The amount and spectral characteristics of the energy being absorbed can be used to estimate the abundance of CO_2 molecules in the atmopsheric column. Measurements using near infrared (NIR) spectral absorbance have high sensitivity near the surface while measurements using the thermal infrared have the highest sensitivity in the mid to upper

troposphere. OCO-2, GOSAT, ASCENDS and SCIAMACHY are all missions with near-surface sensitivity, while AIRS, IASI and TES use the thermal infrared and are hence most sensitive to higher layers of the atmosphere. With the exception of air traffic, all notable sources and sinks for CO_2 are located at the surface; therefore measurements with near-surface sensitivity are of most interest to the carbon cycle science community.

The following sections list some of the satellite missions in order of their launch date and provide some basic operational characteristics. Unless noted otherwise, the missions are still operational and delivering CO_2 observational products.

2.3.2.1 Current and past missions

SCIAMACHY is an imaging spectrometer on the European Space Agency's ENVISAT satellite [e.g. *Buchwitz et al.*, 2007]. ENVISAT was launched in March 2002. Its mission was declared ended in April 2012 after the contact with the satellite was permanently lost (http://www.esa.int/esaCP/SEM1SXSWT1H_index_0.html). ENVISAT operated in a sun-synchronous mode orbit with an equator crossing time of 10:00am local time, a repeat-cycle of 35 days and a swath width of 960 km. Single measurements have a resolution of 60km across track and 30km along track [e.g. *Buchwitz et al.*, 2007]. Full longitudinal coverage at the equator was reached within six days, and faster at higher latitudes [e.g. *Buchwitz et al.*, 2007]. Single measurement retrieval precision was approximately 1.5% [e.g. *Schneising et al.*, 2008].

AIRS is an instrument on the NASA Aqua satellite [e.g. *Aumann and Gaiser*, 2005], which was launched in May 2002. TES is one of four science instruments aboard NASA's Aura satellite, which was launched in July 2004 [e.g. *Kulawik et al.*, 2010]. Both AIRS and TES are part of NASA's Earth Observing System (EOS) and operate in sun-synchronous orbits with equator crossing times of approximately 1:30pm and 1:45pm, respectively, and have a repeat-cycle of 16 days. AIRS has a

swath width of approximately 1650km. while the TES swath width varies depending on operating mode [e.g. *Kulawik et al.*, 2010]. The horizontal resolution of AIRS measurements is 90km $\times$ 90km at nadir. AIRS measurements provide almost global coverage every day and the reported accuracy is better than 2ppm [e.g. *Chahine et al.*, 2008]. TES measurements have a much smaller horizontal resolution of approximately 5km $\times$ 8km. TES delivers $2000 - 3000$ observations every other day, and its coverage is limited to $\pm 40^\circ$ latitude as the retrieval algorithm is based on the thermal contrast between the surface and the atmosphere, which is too low for successful retrievals outside of this range [e.g. *Kulawik et al.*, 2010; *Nassar et al.*, 2011].

IASI was launched on the European MetOp satellite in October 2006 [e.g. *Crevoisier et al.*, 2009]. It flies in sun-synchronous orbit with a 9:30am equator crossing time and has a repeat-cycle of 29 days. The swath width is about 2000km and the single measurement horizontal resolution is 12km^2. The estimated precision is about 2ppm for a $5^\circ \times 5^\circ$ spatial resolution, and the number of observations within each $5^\circ \times 5^\circ$ grid box varies between 10 and 400 depending on cloud coverage *Crevoisier et al.* [2009].

The GOSAT project is a joint effort of the Japanese Ministry of the Environment, the Japanese National Institute for Environmental Studies, and the Japanese Aerospace Exploration Agency. GOSAT was successfully launched on January 23, 2009, and is thereby the first operational satellite mission dedicated to measuring Greenhouse gases, specifically CO_2 and CH_4 [e.g. *Yokota et al.*, 2009]. GOSAT flies in a sun-synchronous orbit with an approximate 1pm equator-crossing time and has a three-day repeat-cycle. For each three-day repeat-cycle there approximately successfully retrieved 900 observations. The footprint size at nadir is a 10.5 km circle and the swath width is approximately 800km [e.g. *Crisp et al.*, 2012]. A more detailed description of the GOSAT mission is given in sections 4.1 and 4.2.

2.3.2.2 Future missions

The Orbiting Carbon Observatory 2 (OCO-2) is NASA's first mission dedicated to observing atmospheric CO_2 [e.g. *Crisp et al.*, 2004]. OCO-2 is a replacement for the first Orbiting Carbon Observatory (OCO) that failed upon launch in February 2009. The instrument design of OCO-2 is almost identical to OCO allowing for a quick schedule to launch with an anticipated launch date as early as November 2014. The characteristic features of OCO-2 measurements are its near-surface sensitivity, a very small footprint of about 3 km^2, and an anticipated precision of 0.3% (1ppm) on regional scales [*Crisp et al.*, 2004]. OCO-2 will fly in a sun-synchronous orbit as part of NASA's Earth Observing System Afternoon Constellation (A-Train) with an approximate 1:15pm equator-crossing time. OCO-2 will have a repeat-cycle of 16 days and will collect approximately 500,000 samples a day leading to very large data sets with detailed, but sparse global coverage for individual days. A more detailed description of the OCO-2 mission is given in chapter III.

The ASCENDS mission is an active CO_2 sensing mission in planning stage with a launch date of 2022 or later [e.g. *Abshire et al.*, 2010]. Notable features of this mission include the ability to sample at night and at extreme latitudes, conditions which are prohibitive to passive missions due to their reliance on reflected sunlight. The lidar measurement technique proposed for the ASCENDS mission will further enable observing through some clouds and aerosols, which represent obstacles to passive missions due the impact of cloud and aerosol scattering [e.g. *Abshire et al.*, 2010; *Kawa et al.*, 2010]. Proof of concept and validation studies indicate that ASCENDS will be able to provide unbiased observations with improved spatial coverage compared to active missions [e.g. *Abshire et al.*, 2010; *Kawa et al.*, 2010; *Spiers et al.*, 2011]. A more detailed description of the ASCENDS mission is provided in chapter V.

2.4 Inversion modeling using atmospheric CO_2 observations

2.4.1 Inverse modeling using ground-based atmospheric CO_2 observations

Inversions are the most frequently applied methodology to gain knowledge about carbon flux distributions from atmospheric CO_2 observations. In inversions, atmospheric CO_2 observations are used in combination with an atmospheric transport model to infer carbon fluxes [e.g. *Enting*, 2002; *Tarantola*, 1987] and, in most recent applications, also the uncertainties associated with these fluxes [e.g. *Gourdji et al.*, 2012; *Gurney et al.*, 2008]. There are a variety of different approaches used to conduct CO_2 inversion studies, most of which employ a Bayesian setup where atmospheric CO_2 observations are used, in combination with an atmospheric transport model and a prior flux distribution, to infer CO_2 fluxes by updating the prior flux distribution [e.g. *Baker et al.*, 2006; *Gurney et al.*, 2008, 2003]. A modification to the Bayesian setup are geostatistical inversions where the atmospheric observations are used to infer a spatial and/or temporal dependence structure among the fluxes[e.g. *Michalak et al.*, 2004]. This eliminates the requirement for explicit prior flux estimates [e.g. *Gourdji et al.*, 2012; *Michalak et al.*, 2004]. Inversion studies are conducted both regionally and globally, where regional inversions typically provide flux estimates at finer spatial scales [e.g. *Gourdji et al.*, 2012]. While inversion setups have become more sophisticated over time [e.g. *Gourdji et al.*, 2012; *Schuh et al.*, 2010], there are still large differences remaining among estimates, and estimated uncertainties, from different studies [e.g. *Baker et al.*, 2006; *Gourdji et al.*, 2012; *Gurney et al.*, 2008, 2003]. Factors that have been cited as leading to these differences include the sparsity of the observational network, the transport model employed, and implementation details of the inversion such as the choice of priors [e.g. *Engelen et al.*, 2002].

Despite these differences, inversions have led to important insights on carbon

fluxes. It has been consistently shown among a multitude of models that the oceans have provided a net carbon sink [e.g. *Gruber et al.*, 2009; *Gurney et al.*, 2008] over the last two decades. Inversions have also highlighted that the interannual variability is larger on the land than on the oceans, and that climatic modes (e.g. El Nino) influence carbon fluxes [e.g. *Gurney et al.*, 2008]. It has further been substantiated that the damped atmospheric CO_2 growth rate following large volcanic eruptions can be detected in inversions [e.g. *Gurney et al.*, 2008].

2.4.2 Inverse modeling using atmospheric CO_2 satellite observations

The unique characteristics of satellite observations of CO_2 are their high spatial density and global coverage compared to the ground-based network. These features will ideally give rise to CO_2 flux fields at high spatial and temporal resolution obtained through inverse modeling. While the spatial coverage is a highly attractive feature, some of the other features of satellite observations can lead to challenges in inversions. These features include that satellite observations of CO_2 have comparatively high measurement errors [e.g. *Crisp et al.*, 2012; *Kulawik et al.*, 2010], often an order of magnitude higher than the measurement errors of ground-based observations, and that these measurement errors can be strongly correlated [e.g. *Hungershoefer et al.*, 2010]. These characteristics of satellite observations have proven challenging for inversions, whose current setups are geared towards using observations from the surface network [*Hungershoefer et al.*, 2010]. In addition, atmospheric CO_2 inversions are in general highly dependent on the choice of the atmospheric transport model used in the inversion [e.g. *Baker et al.*, 2006]. This has recently also been shown to be an important consideration in the case of satellite data based inversions [*Houweling et al.*, 2010].

Most published inversion studies using satellite CO_2 observation are based on synthetic data [e.g. *Baker et al.*, 2010; *Feng et al.*, 2009], while very few studies have

employed actual satellite CO_2 observations in inversions so far. This can partially be attributed to the fact that observing CO_2 from space is still a new field, so limited data are available, and retrieval algorithms of satellite observations of CO_2 are still in development. It is likely that most satellite observations still contain regional biases [e.g. *Crisp et al.*, 2012; *Nassar et al.*, 2011; *Yokota et al.*, 2009]. How these regional biases might translate into errors in the flux estimates is not readily apparent, and could lead to difficulties in the interpretation of these estimates [e.g. *Yokota et al.*, 2009].

One fact that underlines the statement made above is that only one inversion study using GOSAT CO_2 observations has been published during the more than three and a half year period since the launch of the GOSAT satellite in early 2009 [*Yokota et al.*, 2009]. The primary goal of this study was to evaluate to which degree the GOSAT observations can reduce the uncertainty in the flux estimates obtained from inversions using the ground-based network. To this end, the study compared the flux uncertainties obtained from an inversion using only the ground-based network and an inversion using the ground-based network and the GOSAT observations jointly. The GOSAT observations stemmed from the first year of available GOSAT data, ranging from June 2009 to May 2010. The inversion used 64 regions globally and a temporal resolution of one month. Before the use in the inversion, the GOSAT data was averaged to a $5° \times 5°$ monthly grid. The results found uncertainty reductions of up to 50%, with the highest reductions in Africa, Asia and South America, where the ground-based network is sparse. The study, however, cautions regarding potential biases in the data, which were not specifically evaluated in this study [*Yokota et al.*, 2009].

Another study that has been published so far has used AIRS CO_2 observations in an inversion setup. *Chevallier et al.* [2009] compare the results of an inversion using AIRS CO_2 measurements to independent aircraft measurements by transporting the

fluxes obtained in the inversion to the location of the aircraft measurements. As a relative measure, they performed the same comparison for two other inversion setups, namely one based on the atmospheric CO_2 measurements from the surface network and the other one using only on a simple global trend of the annual increase in atmospheric CO_2. The AIRS-based inversion showed improved results in comparison to the prior estimates, but performed worse than the other two inversion setups [*Chevallier et al.*, 2009].

Nassar et al. [2011] investigated using satellite observations from TES and the surface flask measurements jointly in a time-independent Bayesian inversion for 40 regions for 2006. Due to certain aspects of the retrieval methodology, TES CO_2 observations were limited to 40°N–40°S. The study found accordingly that the TES observations provided the highest incremental benefit over a flask-only inversion in the tropics. However, the constraint provided by the satellite observations was still limited such that the uncertainties of the fluxes estimates for the tropical forest of South America and Africa were too large to identify whether this regions were sources or sinks.

Overall, satellite-based inversions of atmospheric CO_2 show significant promise, but have not yet lead to significant advances in our understanding of the carbon cycle.

2.5 Mapping of atmospheric CO_2 satellite observations

The mapping of atmospheric CO_2 concentration fields is a rather direct way of interpreting and making use of satellite CO_2 observations. In this context, the goal of mapping is typically to obtain a continous global concentration field from noisy satellite observations, which enables identifying the structure of the global CO_2 concentration field and to analyze trends with time. Maps can further serve as validation and comparison tools for atmospheric CO_2 concentration fields derived from transported process-based and inventory based flux estimates. For these types of applica-

tions, maps are ideally created at high spatial and temporal resolution to allow for detailed comparisons. CO_2 mapping products should also contain uncertainty measures to identify if differences are indeed indicative of true differences, which exceed the uncertainty inherent in the mapping products. Another situation where mapping is a well-suited approach is in the early stages of a satellite mission, where retrieval algorithms are typically still being improved and biases might exist [e.g. *Crisp et al.*, 2012; *Nassar et al.*, 2011; *Yokota et al.*, 2009]. At these early stages, comparison and validation studies are often mainly targeted at assessing the retrieval algorithm. In these early stages, it is prudent to use observations only in studies where the effect of potential errors in the retrievals is easily perceptible and traceable, which is the case for mapping products.

2.5.1 Current mapping approaches and findings from mapping

The current approaches to mapping of CO_2 satellite observations can be summarized in two broad categories: 1) spatial and temporal averaging/smoothing and 2) data assimilation. Spatial and temporal averaging means defining spatial and temporal bins and averaging all the measurements falling within the bin resulting in, for example, monthly maps with a $5^\circ \times 5^\circ$ latitude/longitude resolution [e.g. *Crevoisier et al.*, 2009]. The resulting averages are sometimes further smoothed by applying a kernel smoothing function such as a boxcar or Gaussian function [e.g. *Schneising et al.*, 2008]. Variants of this approach have been applied in the majority of studies deriving and comparing atmospheric CO_2 concentrations (e.g. [*Crevoisier et al.*, 2004; *Tiwari et al.*, 2006, for AIRS], [*Crevoisier et al.*, 2009, for IASI], [*Schneising et al.*, 2008, for SCIAMACHY]). While these averaged maps allow for the detection of long-term and large-scale features such as the annual increase in atmospheric CO_2 concentration and the seasonal cycle for each hemisphere, they cannot be used to gain insights in the short-term dynamics of the carbon cycle. These monthly or seasonally

averaged maps are also not well suited to serve as detailed validation and parameter tuning tools for forward and atmospheric models, which operate at much shorter time scales.

The challenges with data assimilation derived mapping approaches are of a somewhat different nature. Data assimilation in the context of satellite CO_2 observations refers to methods that incorporate satellite CO_2 measurements within the framework of often highly sophisticated atmospheric models [e.g. *Baker et al.*, 2010; *Engelen et al.*, 2009; *Feng et al.*, 2009]. The CO_2 measurements are used to update the model-derived prior state of the CO_2 concentration or to derive CO_2 flux estimates. Data assimilation methods can incorporate and merge a variety of measurements from different sources, such as other satellite measurements, to derive the state of the atmosphere, which makes them potentially very powerful. They do, however, rely on atmospheric transport models as the core of their model formulation. That fact implies that the CO_2 concentration maps created by data assimilation approaches are not only based on the CO_2 measurements, but also on the atmospheric transport model. This makes it difficult to use these CO_2 maps as independent comparison and improvement tools for process-based and atmospheric transport models. As an illustrative example: if atmospheric CO_2 concentration fields resulting from two different process-based models were to be compared to atmospheric CO_2 maps derived from data assimilation methods, the results might be influenced by the similarity, or lack thereof, of the model formulation of atmospheric transport models used in the process-based model and the data assimilation model.

Findings from studies using mapping of satellite CO_2 observations include those from global comparisons of monthly or bi-monthly averaged maps of AIRS observations with model data [e.g. *Chahine et al.*, 2008; *Tiwari et al.*, 2006]. These comparisons generally indicated higher variability in the AIRS-derived CO_2 distributions than in the CO_2 distributions calculated by the models, possibly indicating

incorrectly-modeled vertical transport of CO_2 [*Chahine et al.*, 2008]. The coarse temporal and spatial averaging of the AIRS CO_2 concentrations used in these studies, however, made it difficult to pin-point the exact causes for these differences. In a different study, *Tiwari et al.* [2006], using zonally and monthly averaged AIRS CO_2 concentration, could not detect the annual increase in the global atmospheric CO_2 concentrations for 2003. The AIRS CO_2 concentrations, sampled at the location of high altitude tower measurements, did, however, exhibit an annual increase and a good match to the trend of the tower measurements [*Tiwari et al.*, 2006]. *Tiwari et al.* [2006] specifically mention that their temporal and zonal averaging procedure may hide some of the information contained in the retrievals that would show the annual increase in global CO_2 concentrations.

Mapping approaches have also been applied to evaluate SCIAMACHY CO_2 observations. While large-scale features such as the annual increase in CO_2 could be verified through SCIAMACHY satellite measurements [*Buchwitz et al.*, 2007], seasonal and monthly maps indicate discrepancies with model data that might at least be partially the result of retrieval algorithm problems [*Schneising et al.*, 2008]. Currently, the only mapping study using IASI CO_2 measurements is limited to ocean surfaces in the tropics. The maps shown in this study are seasonal and show good agreement with seasonally averaged aircraft measurements [*Crevoisier et al.*, 2009].

Overall, mapping of satellite observations has served to assess the quality of CO_2 satellite products, but has not yet been employed in a manner to use satellite observations of atmospheric CO_2 to enhance knowledge of the processes driving the carbon cycle. An improved mapping approach that can optimally use the information content of the satellite observations to map CO_2 concentration fields at high spatial and temporal resolution with uncertainties could achieve that through, for example, probabilistic comparisons of the satellite observation-based mapping products with CO_2 concentrations from process-understanding based models.

2.5.2 Geostatistical approach to mapping of atmospheric CO_2

The goal of an alternative mapping method is to provide atmospheric CO_2 concentration maps that are not based on any process-based or atmospheric transport models, but can still be created at temporal and spatial resolutions that are much higher than those typically required for binning approaches (described in Section 2.5.1). Maps of atmospheric CO_2 are ideally created at a temporal resolution of a few days, i.e. synoptic time scales, so they can be used to gain insights in the short-term dynamics of atmospheric CO_2 distributions, can serve as data-driven independent validation datasets for atmospheric and carbon cycle models, and can be used in a variety of other studies discussed in subsequent chapters of this dissertation.

One approach to achieve this goal is to conceptualize and model global atmospheric CO_2 concentrations as a realization of a stochastic process or random field. This viewpoint implies the assumption of the existence of spatial correlation in the atmospheric CO_2 concentration field, which is an assumption independent of any process-based or atmospheric transport model. Once derived, the spatial correlation structure of the CO_2 concentration field can be used to obtain maps of the global CO_2 concentration field. The framework of geostatistics is a common toolset to estimate properties of random fields for geolocated data [e.g. *Chiles and Delfiner*, 1999; *Cressie*, 1993]. Attractive features of a geostatistical approach include the ability to use only the data itself to derive the correlation structure, to incorporate measurement noise information, and to provide location-dependent best estimates and associated uncertainties. The following paragraphs provide an overview of geostatistical concepts, with a focus on aspects of geostatistics relevant to the mapping of atmospheric CO_2 concentrations. Details of the methodology developed and employed in this dissertation are discussed in section 3.2.

2.5.2.1 Introduction to geostatistics and basic definitions

In a broad sense, the term geostatistics describes statistical methods to conduct inference and prediction for spatially-referenced data [e.g. *Chiles and Delfiner*, 1999; *Cressie*, 1993]. Geostatistical methods have developed somewhat independently in several fields ranging from meteorology to mining (see Chapter 1 in *Gelfand* [2010] for a historical overview). With the growing maturity of the field various applications in different areas have merged into the by now well-established framework of geostatistics [e.g. *Chiles and Delfiner*, 1999; *Kitanidis*, 1997], which is itself a subdomain of the field of spatial statistics [*Gelfand*, 2010].

In its most general form, the underlying statistical model is a random field

$$\{Y(\mathbf{s}) : \mathbf{s} \in D\}; \tag{2.1}$$

where $Y(\mathbf{s})$ is a random variable at spatial locations $\mathbf{s}$, which vary over the index set $D \subset \mathbb{R}^d$ [e.g. *Cressie*, 1993]. If $\mathbf{s}$ vary continuously over D, the resulting data are referred to as point-referenced, or geostatistical, data [e.g. *Cressie*, 1993]. The associated random field or process $\{Y(\mathbf{s}) : \mathbf{s} \in D\}$ is then referred to as a stochastic or spatial process [e.g. *Cressie*, 1993]. In this dissertation, the global CO_2 concentrations are represented by a spatial process. In principle the spatial locations $\mathbf{s}$ vary continuously over D. In real applications, however, data (such as satellite observations of CO_2) are collected at a finite number of locations. Hence, the observations constitute a partial realization of the spatial process, i.e. of the global CO_2 concentration field, plus any noise. This partial realization is denoted as $\{y(\mathbf{s}) : \mathbf{s} \in D\}$ [e.g. *Cressie*, 1993]. The goal of geostatistical methods is to infer the spatial process $Y(s)$ and predict the best estimate of process values at new locations based upon this partial realization [e.g. *Cressie*, 1993]. In this dissertation, the goal is hence to infer the global CO_2 concentration field from the satellite observations.

2.5.2.2 Stationarity, semivariogram and covariance functions

In order to allow for inference based on a partial realization of the process, i.e. the satellite observations of CO_2, some additional assumptions on the spatial process need to be made. A very strong assumption is strict stationarity, which states that the joint distribution function is invariant to translation [e.g. *Banerjee et al.*, 2004]. Formally, a process is strictly stationary if for any subset $\{s_1, \ldots, s_n\}$ and any $\mathbf{h} \in D$, the probability distribution of $(Y(\mathbf{s_1}), \ldots, Y(\mathbf{s_n}))$ is equal to the distribution of $(Y(\mathbf{s_1}+\mathbf{h}), \ldots, Y(\mathbf{s_n}+\mathbf{h}))$ [e.g. *Banerjee et al.*, 2004]; here $\mathbf{h}$ represents the separation vector between two locations in D. A weaker assumption is second-order stationarity which states that $Cov(Y(\mathbf{s_1}), Y(\mathbf{s_2})) = C(\mathbf{s_1} - \mathbf{s_2})$, implying that the covariance between values at two locations depends only on their separation vector [e.g. *Banerjee et al.*, 2004]. A special case of a second-order stationary process is an isotropic process where the covariance between values at two locations is a function of their separation distance, so $Cov(Y(\mathbf{s_1}), Y(\mathbf{s_2})) = C(\|\mathbf{s_1} - \mathbf{s_2}\|)$ [e.g. *Banerjee et al.*, 2004].

Another form of stationarity is intrinsic stationarity which is defined through differences. The assumptions are $E(Y(\mathbf{s}+\mathbf{h}) - Y(\mathbf{s})) = 0$ and $Var(Y(\mathbf{s}+\mathbf{h}) - Y(\mathbf{s})) = 2\gamma(\mathbf{h})$, where the function $\gamma(\cdot)$ is called the semivariogram [e.g. *Cressie*, 1993]. A distinguishing feature of intrinsic stationarity compared to second-order stationary is that the mean throughout the field is assumed constant, but not known [e.g. *Cressie*, 1993]. This difference is important for practical applications, where the mean value is often unknown, but the assumption of a constant mean is reasonable. Second-order stationarity implies intrinsic stationarity. If the semivariogram, which is defined as $\gamma(Y(\mathbf{s_1}), Y(\mathbf{s_2})) = \frac{1}{2}Var(Y(\mathbf{s_1}) - Y(\mathbf{s_2}))$, is only a function of the distance, so $\gamma(\cdot)$ can be written as $\gamma(\|\mathbf{h}\|)$, the process is called homogeneous [*Banerjee et al.*, 2004]. The physical interpretation of homogeneity is that the correlation structure is the same throughout the field irrespective of direction and location within the field. Atmospheric CO_2 concentration fields are not homogeneous globally [*Alkhaled et al.*,

2008], but, as is shown in Chapter III, can be successfully modeled assuming local homogeneity. As such, classical geostatistical estimation tools, which are based on the assumption of a homogeneous process and which are outlined below, form the base methodology used in this dissertation. These tools are then further developed to infer global CO_2 concentration fields from satellite observations (see Chapter III).

Under the assumption of a homogeneous process, the semivariogram $\gamma(\cdot)$ characterizes the random field and needs to be determined for the subsequent modeling steps [e.g. *Cressie*, 1993]. The conceptual idea is to define parametric functions as candidates to represent the semivariogram $\gamma(\cdot)$. The parametric function, which is referred to as the theoretical semivariogram function, is typically chosen based on process knowledge or based on characteristics of the data [e.g. *Chiles and Delfiner*, 1999; *Kitanidis*, 1997]. An overview of variogram functions is given in *Gelfand* [2010]. The variogram function used in this work, based on prior findings [*Alkhaled et al.*, 2008] and analysis of the data used in this dissertation, is the exponential variogram function defined as:

$$\gamma(h) = \sigma^2 \left[1 - \exp\left(-\frac{h}{l} \right) \right], \tag{2.2}$$

where the parameters l and σ^2 are referred to as the range and variance parameters and where h is the distance between two locations [e.g. *Chiles and Delfiner*, 1999]. A modified version of this approach is applied in this dissertation and described in Section 3.2.

One approach to determine the parameters of the theoretical semivariogram function is to use the raw semivariogram of the data, defined as:

$$\gamma(h) = \frac{1}{2}[Y(s_i) - Y(s_j)]^2; \tag{2.3}$$

for all pairs of measurement values $Y(s_i), Y(s_j)$, where h is the distance between s_i and s_j [e.g. *Chiles and Delfiner*, 1999].

Second-order stationary processes have a covariance function $C(\cdot)$ corresponding to the semivariogram $\gamma(\cdot)$ function [e.g. *Chiles and Delfiner*, 1999]. For these processes, the covariance function can be derived from from the semivariogram function based on the following relationship: $C(h) = C(0) - \gamma(h)$ [e.g. *Chiles and Delfiner*, 1999]. The covariance function for the exponential model used in this disseration is:

$$C(h) = \sigma^2 \exp\left(-\frac{h}{l}\right). \tag{2.4}$$

For a covariance function to be valid, it needs to be positive-definite for the corresponding dimension of the random process (see *Stein* [1999] for a detailed discussion), which is an important modeling consideration. The atmospheric CO_2 concentrations considered in this thesis are measured globally, and require therefore a covariance function that is valid on the sphere. The exponential covariance function applied in this thesis has proven to be valid on the sphere [*Huang et al.*, 2009].

2.5.2.3 Kriging

Kriging refers to predicting the process value at a specified location s_0 in the domain D of the spatial process [e.g. *Cressie*, 1993]. Here, kriging refers to predicting global CO_2 concentration fields. The classic geostatistical derivation is based on finding the best linear unbiased estimator given the data under the assumption of intrinsic stationarity [e.g. *Cressie*, 1993]. A best linear unbiased estimator is an estimator that minimizes the squared error, is linear in the data values and has an expected value identical to the true value to be estimated [e.g. *Cressie*, 1993]. In the case of an unbiased estimator, minimizing the squared error of the estimator corresponds to minimizing the variance of the estimator [e.g. *Cressie*, 1993]. The unbiasedness condition leads to a constrained optimization problem. The solution to this optimization problem (using for example the technique of Lagrange multipliers)

provides the so-called ordinary kriging estimates and uncertainties [e.g. *Chiles and Delfiner*, 1999; *Cressie*, 1993]. No distributional assumptions other than intrinsic stationary are required. An example of such a linear kriging system is shown in equation 3.5.

2.5.2.4 Nonstationarity

Nonstationary means that the spatial dependence structure, which describes the correlation among values as a function of their locations, is not constant throughout the random field. In the case of nonstationarity, the covariance function is not only a function of the separation vector $\mathbf{h}$ or the distance $\|\mathbf{h}\|$ between two locations as assumed in stationary and isotropic models, respectively, but a function of the locations themselves [e.g. *Gelfand*, 2010]. Formally, $Cov(Y(s_1), Y(s_2)) = C(s_1, s_2)$ where $C(\cdot, \cdot)$ is symmetric in its arguments and a positive definite function. Many geophysical phenomena, including atmospheric CO_2 concentrations [*Alkhaled et al.*, 2008], measured over large areas or globally exhibit nonstationarity, which needs to be accounted for in the modeling procedure for proper inference. The presence of nonstationarity invalidates the use of classical variogram fitting to estimate the covariance structure, which is based on the assumption of a homogeneous process, where spatial dependence is only a function of distance, but not location. However, to allow for inference, some assumptions on the process or the structure of the covariance need to be made [e.g. *Gelfand*, 2010]. The following paragraphs provide an overview of modeling approaches for nonstationary spatial processes, with a focus on computational feasibility for large data sets such as satellite observations of CO_2.

A straight-forward approach is the moving window covariance estimation and kriging methodology using the assumption of local stationarity [*Haas*, 1990]. The covariance parameters are derived and prediction is performed using only data points within a window of specified size around each estimation location using the classical

estimation and prediction procedure outlined in the previous sections. While this method is computationally efficient and accounts for nonstationarity, it does not lead to a globally valid positive definite covariance matrix over all sites [e.g. *Clark and Gelfand*, 2006], which implies that the underlying model is only point-wise valid. A modified version of the moving window covariance estimation and kriging methodology specifically targeted to satellite observations of CO_2 has been developed and applied in this dissertation and is described in detail in Chapter III.

More complex approaches, falling in the category of dimension-reduction techniques, model the process through a low-dimensional random vector, and introduce spatial dependency through the covariance matrix of the random vector. One example of this approach is Fixed Rank Kriging [*Cressie and Johannesson*, 2008], where the random vector used for incorporating the spatial dependency is of much lower dimension than the data. In an alternative approach, *Stein* [2005] parameterizes the covariance matrix as a function of latitude and achieves computational efficiency through the use of Fast Fourier Transforms. This approach, however, requires measurement data on a regular grid, which is not the case for satellite CO_2 data.

Mathematically more involved approaches include transformation and kernel convolution. Transformation, also called deformation, is based on the idea to transform the model region D to a new region where the process becomes stationary [*Sampson and Guttorp*, 1992]. The main limitation of the transformation approach is that the implementation requires independent repeated measurements at the same location, which are often not attainable [*Banerjee et al.*, 2004]. Kernel convolution methods are based on the fact that a Gaussian process can be constructed through the convolution of independent random variables and a kernel function [e.g. *Higdon et al.*, 1998] for a detailed description of the approach). Nonstationarity can be introduced by defining the kernel function through location-dependent parameters [e.g. *Zhu and Wu*, 2010]. The main limitation of this approach is that the derived covariance function is, apart

from special cases, in the form of an integral expression that does not have a closed form solution and needs to be evaluated numerically. This numerical evaluation is computationally very intensive and, considering the size of satellite CO_2 data sets, in its current form not feasible.

CHAPTER III

High resolution mapping of CO_2

3.1 Introduction

Atmospheric carbon dioxide (CO_2) is the most important anthropogenic greenhouse gas [*Solomon et al.*, 2007]. While data from the existing CO_2 monitoring network have been crucial to gaining important insights into the functioning of the carbon cycle, the mechanisms controlling the inter-annual variability and the spatial distribution of carbon uptake and emissions are still not fully understood [e.g. *Feng et al.*, 2009; *Heimann*, 2009; *Nevison et al.*, 2008; *Yang et al.*, 2007]. The accurate prediction and mitigation of climate change requires a better understanding of these processes and the carbon cycle in general [*Friedlingstein et al.*, 2006].

Satellite observations of CO_2, because of their global coverage and high measurement density, offer new opportunities to improve this understanding. Observations from several satellites are already being used to infer atmospheric CO_2 concentrations, including the Japanese Greenhouse Gases Observing Satellite (GOSAT) [*Hamazaki et al.*, 2004], which is the first satellite dedicated to the measurement of greenhouse gases. NASA's Orbiting Carbon Observatory 2 (OCO-2) is the first American mission designed specifically for making high precision measurement of CO_2 [*Crisp et al.*, 2004], and is expected to be launched in 2015.

Despite their high measurement density, however, satellite CO_2 observations have

gaps due to their orbit configurations and due to geophysical limitations such as cloud cover and are subject to substantially higher measurement uncertainties relative to in situ observations. Using statistical techniques to leverage the spatial correlation in the CO_2 concentration field and to predict full-coverage global CO_2 concentration distributions from satellite observations (i.e. creating Level 3 data products) is one way to gain new information about the carbon cycle.

Once derived, such maps can be used for comparison studies with carbon flux estimates coupled with an atmospheric transport model to generate modeled CO_2 fields, or with other available atmospheric measurements. If the satellite-derived Level 3 products were to include rigorous uncertainty measures, such comparisons could be conducted probabilistically, making it possible to assess whether and where, for example, a given set of flux estimates coupled with a specific transport model differ significantly from the satellite-derived Level 3 maps. Such Level 3 products are not intended to be used in inversion studies directly, but instead provide a useful complement to such studies. Beyond point-wise comparisons with individual observations, comparisons with global CO_2 concentration distributions make it possible to identify spatially continuous areas of mismatch, providing indicators for potential discrepancies with other datasets and their dependence on the atmospheric or surface characteristics. Ideally, such comparison studies should be done at high temporal resolution, so that mismatches are not missed through temporal averaging and so that the underlying causes for any mismatches can be tracked in detail. Such comparison studies could, among other applications, inform the growing need to verify and track reported CO_2 emissions [*Committee on Methods for Estimating Greenhouse Gas Emissions, National Research Council*, 2010; *Nisbet and Weiss*, 2010].

There are currently several approaches for creating Level 3 products from CO_2 satellite observations, ranging from simple methods such as spatial and temporal averaging [e.g. *Crevoisier et al.*, 2009; *Kulawik et al.*, 2010; *Tiwari et al.*, 2006] to

sophisticated data assimilation approaches [*Engelen et al.*, 2009]. Spatial and temporal averaging entails binning and averaging the data to relatively coarse spatial and temporal grids to obtain smoother maps and to average out the measurement errors. Temporal averaging over months or seasons is commonly applied to satellite data representing properties that vary on seasonal or interannual timescales, such as land cover and phenology. The impact of such temporal averaging on atmospheric CO_2 concentrations, which vary on synoptic timescales, has not been explored. It is obvious, however, that any of the dynamic information, operating at time scales shorter than the temporal averaging time step, is lost. The same applies to spatial variability at scales smaller than the resolution of the spatial averaging grid. Another disadvantage of binning and averaging the data is that the uncertainties associated with the binned data are typically not quantified, which eliminates the option of making probabilistic comparisons.

Data assimilation approaches, on the other hand, require boundary conditions such as carbon flux estimates and transport models to obtain full-coverage global atmospheric CO_2 concentrations. While incorporating this additional information can be powerful, it also implies that the assimilated atmospheric CO_2 fields are sensitive to any misspecification in these prior assumptions. This strong dependence on prior assumptions can especially affect comparison studies: it can be difficult to establish the degree to which apparent similarities or differences between the data-assimilation-derived CO_2 distributions and, for example, coupled biospheric- and atmospheric-transport-model derived CO_2 concentrations are based on similar or dissimilar prior assumptions.

In this chapter we present and evaluate an alternative method for generating global Level 3 CO_2 products from satellite observations (this is based on [*Hammerling et al.*, 2012]). The method leverages the fact that atmospheric CO_2 concentrations exhibit spatial correlation, by characterizing this spatial correlation and using this

information to statistically derive global CO_2 concentrations and their associated uncertainties. This proposed geostatistical approach accounts for measurement errors and does not require estimates of fluxes or an atmospheric transport model, which is advantageous for comparison studies because the Level 3 products can serve as independent validation data sets.

We use OCO-2 as a prototypical example application for evaluating the method, because making the best use of future OCO-2 observations will represent an important challenge. While the observations will have high precision and a small field of view, their spatial coverage for a given day will be limited. As a result, the length of the time period over which observations are aggregated represents a trade-off between the spatial coverage that the observations can provide and the loss of any information about temporal variability that is masked by combining observations over longer periods. Finding a balance between these effects, and being aware of the consequences of the choice of the length of the aggregation time period, is critical to creating and interpreting global CO_2 maps based on the anticipated data from OCO-2. The presented sample application therefore quantifies the quality of global CO_2 Level 3 products based on simulated OCO-2 observations for time periods ranging from 1 to 16 days.

3.2 Mapping Methodology

The geostatistical mapping method applied here accounts for and exploits the spatial correlation of CO_2 between different locations [e.g. *Chiles and Delfiner*, 1999; *Cressie*, 1993; *Gelfand*, 2010]. First, it infers the spatial covariance structure of the CO_2 concentrations. Second, CO_2 concentrations and associated uncertainties are predicted globally, using the available observations and the spatial covariance structure inferred in the first step. Note that here prediction specifically refers to spatial interpolation of available data, not to temporal prediction.

Alkhaled et al. [2008] showed that global CO_2 concentrations exhibit spatial non-stationarity, such that the expected degree of spatial variability in the CO_2 field itself varies across the globe. For example, CO_2 concentrations over oceans are generally correlated over longer distances than over land. Exploratory analysis of the modeled CO_2 concentrations used here further supports this conclusion, and, as a result, the approach presented here uses a non-stationary statistical framework. The framework chosen is similar to moving window kriging [*Haas*, 1990], which is, among spatial statistical methods to treat non-stationarity, a rather simple and straightforward approach. From a theoretical point of view, a drawback of moving window kriging is that it does not enforce a globally valid spatial model [e.g. *Chen et al.*, 2006; *Zhu and Wu*, 2010], but is based on covariance functions that are only valid locally. From a computational point of view, the chosen framework is efficient, as both the estimation of the covariance structure and the prediction of the CO_2 concentrations and their associated uncertainties is executed locally and can be implemented using parallel computing approaches.

3.2.1 Estimation of non-stationary covariance structure

We estimate the global non-stationary covariance structure by using a local semi-variogram analysis based on the assumption of local stationarity. The method is similar to the approach taken by *Alkhaled et al.* [2008]. The spatial covariance structure specific to each location is estimated by using observations in a local neighborhood surrounding this location. The local neighborhood is defined here as a region within 2000-km of each location, as in *Alkhaled et al.* [2008], who found such areas to be large enough to capture most of the variability, while being small enough to preserve local phenomena. Further analysis of the neighborhood size conducted in our study confirmed these findings.

Variogram analysis is a tool for quantifying spatial variability as a function of

the separation distance between observations. As a first step the raw variogram is calculated:

$$y(h) = \frac{1}{2}\big[y(x_i) - y(x_j)\big]^2, \tag{3.1}$$

where h is the separation distance between locations x_i and x_j, defined as the great-circle distance

$$h(x_i, x_j) = r\cos^{-1}\Big(\sin\varphi_i \sin\varphi_j + \cos\varphi_i \cos\varphi_j \cos(\lambda_i - \lambda_j)\Big), \tag{3.2}$$

where r is the radius of the Earth, φ_i and λ_i are the latitude and longitude of location x_i, and $y(x_i)$ is the CO_2 value at location x_i. The local variogram analysis is implemented by including all the pairs of observations, where both observations fall within 2000-km of a given location, and a subset of the pairs for which one observation is within 2000-km and the other is further away. The number of pairs in the subset was chosen such that the number of outside observations was a quarter of the number of inside observations. This number is based on a sensitivity analysis for the effect of the selection of outside observations to ensure that the variogram parameters are robustly estimated and do not vary as a function of the randomly selected subset of outside points.

In the second step, a parametric function, the theoretical variogram, is fitted to the raw variogram using non-linear least squares. The function fitted was the exponential variogram function combined with a nugget-effect variogram model given by:

$$\gamma(h) = \left\{ \begin{array}{ll} 0 & \text{for } h = 0 \\ \sigma^2\left(1 - \exp\left(-\dfrac{h}{l}\right)\right) + \sigma^2_{\text{nug}} & \text{for } h > 0 \end{array} \right\}, \tag{3.3}$$

where σ^2 and l are the variance and correlation length parameters of the exponential variogram, and σ^2_{nug} is the nugget variance, which is representative of the retrieval/measurement errors. The choice of the exponential variogram was based on

earlier analysis by *Alkhaled et al.* [2008]. The nugget-effect component accounts for the random noise added to the observations in this synthetic-data study to represent the measurement noise (see section 3.3.1). This variance component is fixed to the variance of the noise added to the observations, and represents the variance of retrieval errors for real data applications. Variogram parameters were estimated for each location on a $1^\circ \times 1.25^\circ$ global grid to match the resolution of the model data used in the analysis (section 3.3.1), but any convenient resolution could be used with real data from OCO-2 as long as the resolution was sufficiently fine to capture the variability of the data.

The exponential variogram parameters can be used to define an exponential covariance function:

$$C(h) = \sigma^2 \exp\left(-\frac{h}{l}\right), \tag{3.4}$$

where the parameters σ^2 and l are as defined previously, such that the estimated parameters of the variogram specify the covariance function.

3.2.2 Local kriging

Kriging is a minimum variance linear unbiased prediction method for spatial data. Linear refers to the fact that the predicted value at a given location is expressed as a linear combination of the values observed at sampled locations. A notable feature of kriging, differentiating it from simpler interpolation methods such as inverse distance weighting, is that an observation is not only weighted as a function of its distance to the prediction location, but also as a function of its location relative to those of other observations. As such, clustered observations that provide redundant information receive comparatively less weight. Another attractive feature of kriging is that it can account for measurement error. Finally, kriging quantifies the uncertainty in the predicted value.

The linear system that is solved to obtain the weights $\boldsymbol{\lambda}$ for a single prediction

location given observations at n locations is

$$\begin{bmatrix} \mathbf{Q}+\mathbf{R} & \mathbf{1} \\ \mathbf{1}^T & 0 \end{bmatrix} \begin{bmatrix} \boldsymbol{\lambda} \\ \nu \end{bmatrix} = \begin{bmatrix} \mathbf{q} \\ 1 \end{bmatrix}, \tag{3.5}$$

where $\mathbf{Q}$ is an $n \times n$ covariance matrix among the n observation locations, as defined in equation (3.4), $\mathbf{R}$ is an $n \times n$ measurement error covariance matrix among the n observation locations, $\boldsymbol{\lambda}$ is a $n \times 1$ vector of weights, ν is a Lagrange multiplier and $\mathbf{q}$ is the $n \times 1$ vector of the spatial covariances between an individual prediction location and the observation locations, also defined using equation (3.4). If the measurement errors are assumed independent between observation locations, as is the case in this work, then $\mathbf{R}$ is a diagonal matrix with the measurement error variance σ^2_{nug} on the diagonal. The predicted value, $\widehat{y}$, and the prediction uncertainty, $\sigma^2_{\widehat{y}}$, at the location are:

$$\widehat{y} = \boldsymbol{\lambda}^T \mathbf{y} \tag{3.6}$$

$$\sigma^2_{\widehat{y}} = \sigma^2 - \boldsymbol{\lambda}^T \mathbf{q} - \nu, \tag{3.7}$$

where $\mathbf{y}$ are the observations at the n locations and σ^2 is the variance as shown in equation (3.4).

'Local' refers to the fact that the covariance parameters used to calculate the spatial covariances are specific to each prediction location, and that only observations within a given neighborhood of the prediction location are considered [e.g. *Haas*, 1990; *Kitanidis*, 1997]. As described in section 3.2.1, the covariance parameters are derived at each prediction location. Only observations within 2000-km were used in the kriging step, motivated by the shielding effect [*Wackernagel*, 2003]. The validity of the assumption that observations at more than 2000 km have a negligible influence on the predicted value was verified by comparing the predicted values for increasingly larger neighborhoods (results not shown).

In a small number of cases (less than 0.1% of the prediction locations on average), no observations were available within 2000 km, and the kriging procedure could not be applied. In these cases a simple imputation technique was applied using the predicted value and uncertainty of the closest location where the local kriging procedure could be executed.

3.3 Study Design and Data

Our study was designed to evaluate how well global CO_2 concentrations can be reconstructed from satellite observations using a geostatistical mapping method. The specific emphasis was on recreating global CO_2 concentrations based on future OCO-2 observations for short time periods ranging from 1 day to one repeat cycle (i.e. 16 days). OCO-2 is scheduled for launch in 2015, and is a replacement for OCO, which failed upon launch, and was to be NASA's first satellite mission dedicated to observing atmospheric CO_2. Some of the most noteworthy features of OCO-2 are the sensitivity to the near-surface CO_2 abundance, the measurement footprint of about 3 km^2, and an anticipated measurement precision of 1 ppm once soundings are averaged over regional scales [*Crisp et al.*, 2004]. OCO-2 will be part of NASA EOS Afternoon constellation (A-train) [*L'Ecuyer and Jiang*, 2010], which flies in a sun-synchronous polar orbit with a 16-day repeat-cycle.

3.3.1 Simulated OCO-2 CO_2 observations

The atmospheric CO_2 field is simulated using the PCTM/GEOS-4/CASA-GFED (referred to simply as PCTM in the discussion that follows) atmospheric model coupled with biospheric, biomass burning, oceanic, and anthropogenic CO_2 flux estimates [*Kawa et al.*, 2004, 2010]. This model uses analyzed meteorological fields to drive both the biospheric flux and atmospheric transport. The model grid is $1^\circ \times 1.25^\circ \times 28$ vertical levels with hourly output. The PCTM/GEOS-4 model has been widely tested,

and has shown good results in carbon cycling comparison studies [e.g. *Kawa et al.*, 2004; *Law et al.*, 2008b; *Parazoo et al.*, 2008]. CO_2 mixing ratios in the lowest 20 vertical layers of the model (up to 40 mbar) were pressure-averaged to simulate the vertical sensitivity of OCO-2. Prospective OCO-2 sounding locations were determined by overlaying the Cloud-Aerosol Lidar and Infrared Pathfinder Satellite Observations (CALIPSO) [*Winker et al.*, 2003] track on the CO_2 field for each day within a given repeat-cycle. The CALIPSO track was used because this satellite is also part of NASA's A-train constellation, and CALIPSO flies only minutes apart from the orbit planned for OCO-2. Differences in the OCO-2 slant path and glint location offset were not accounted for, so the CALIPSO track is only a close approximation to the true OCO-2 track.

The presence of clouds and aerosols will impede the retrieval of atmospheric CO_2 concentrations, leading to gaps in the OCO-2 observations along the satellite track. To represent the presence of these gaps in a realistic manner, the combined cloud and aerosol optical depth (532nm) from the version 2.01 5-km CALIPSO data was used to identify locations on the track where the total cloud and aerosol optical depth was below 0.3, which is a conservative estimate of the maximum optical depth that will allow for the successful retrieval of CO2 [D. M. O'Brien, personal communication]. Using this approach to account for clouds and aerosols has the advantage of matching the CALIPSO data with the PCTM output in time, which allows for a more realistic representation of the cloud-aerosol-CO_2 distribution relative to using probabilistic cloud and aerosol masks based on seasonal averages. The CALIPSO along-track horizontal resolution of 5 km was matched with the coarser PCTM $1^\circ \times 1.25^\circ$ horizontal resolution by considering a model grid box visible if at least one CALIPSO measurement with a combined optical depth of less than 0.3 fell within the grid box. The second row in Figures 3.1d–3.1f show typical patterns and amounts of visible locations (at the PCTM grid resolution) for 1-day, 4-day and 16-day time periods.

OCO-2's footprint of approximately 3 km^2 will be much finer than the PCTM horizontal resolution used in this study, and the simulated OCO-2 observations used here therefore most closely resemble a setup where the true observations would be pre-averaged to the PCTM/GEOS resolution of $1^\circ \times 1.25^\circ$. This setup has implications for the measurement error characteristics. Having multiple OCO-2 soundings within a PCTM gridbox reduces the measurement error associated with the average CO_2 value in the gridbox relative to the uncertainty of a single sounding. The relative reduction of the measurement error is a function of the number, spatial configuration, and measurement error correlation of the soundings within a gridbox. The procedure and the assumptions made to account for multiple soundings within a gridbox and characterize the measurement error associated with a grid box are described in detail in section 3.3.2.

Some other features associated with the finer resolution of the true OCO-2 observations are not directly assessed in this study; namely, the computational aspects associated with the number of OCO-2 observations, and the possibility of capturing CO_2 variability on very fine scales. OCO-2's fine resolution leads to a large total number of observations, up to hundreds of thousands each day, which could cause computational problems for traditional geostatistical gap-filling methods. The local covariance estimation and kriging setup described here (section 3.2), however, are well suited to handling a large amount of observations, and have been specifically designed to do so.

3.3.2 Experimental setup

The primary goals of the experiment were to evaluate (1) the overall performance of the proposed approach, and (2) how the temporal resolution, which is the length of the time period over which observations are accumulated to make a single map, affected the quality of the resulting map. The quality of the obtained maps was

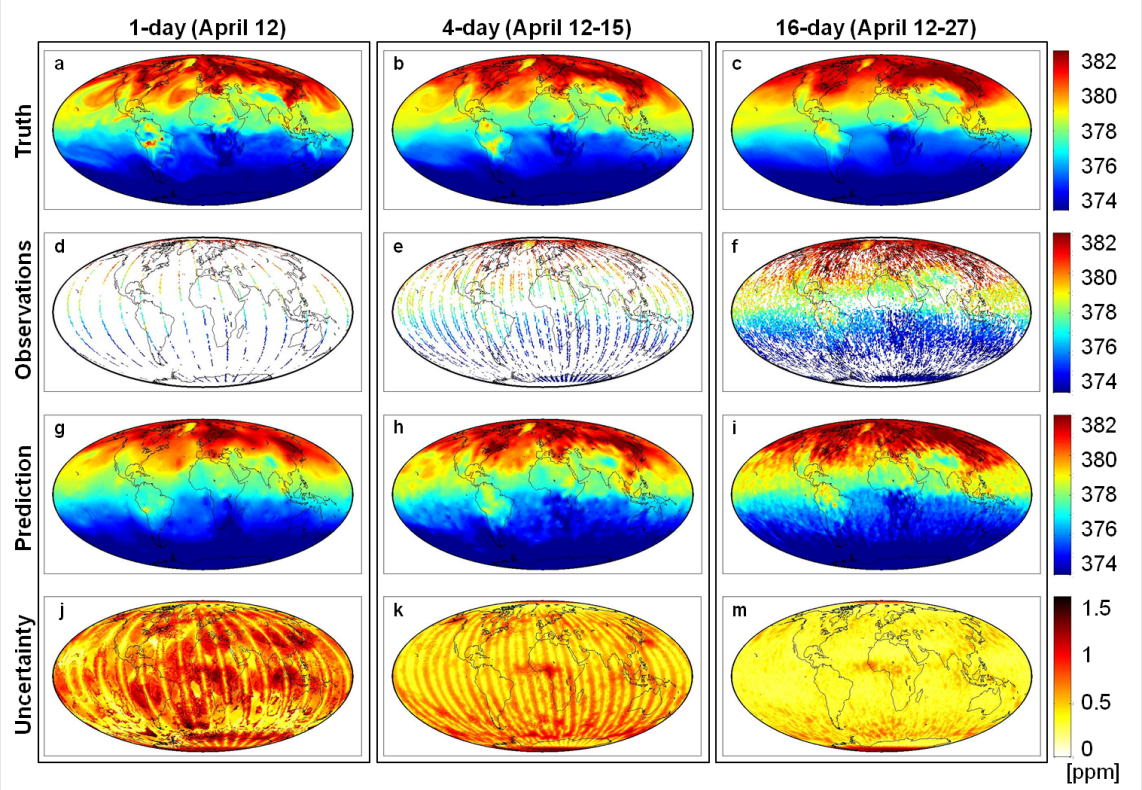

Figure 3.1: PCTM/GEOS-4 CO2 model output ("Truth"), simulated OCO-2 observations ("Observations"), gap-filled predictions ("Prediction") and estimated prediction uncertainties ("Uncertainty") expressed as a standard deviation for a 1-day, a 4-day and a 16-day time period in April 2006. The observation locations and values are derived by overlaying CALIPSO track and cloud and aerosol information on PCTM/GEOS-4 CO_2 from individual days in the repeat cycle. The gap-filled predictions are shown for the medium measurement noise scenario with the covariance estimated from observations.

evaluated by comparing these maps and their inferred uncertainties to the full model data, which were time-averaged over to the period of the observations used to create the maps. The details of the comparison measures are discussed in sections 3.4.2 and 3.4.2. The experiment was specifically designed to assemble observations in a manner that is realistic for satellite observations: the simulated observations were not taken from a time-averaged CO_2 concentration field, but were sampled from individual days at the hour nearest the local overpass time (approximately 1330 h). For example, the observations shown in Figure 3.4f are sampled from 16 different days of PCTM output, corresponding to the actual day for each sounding. This way of simulating observations results in a field that represents an aggregation of observations from different days rather than temporally-averaged observations. The true field, however, is the full 3-D model output time-averaged over the aggregation period. Figures 3.1a, 3.1b, 3.1c provide an example of the 1-day, 4-day and 16-day true fields.

In addition to the temporal resolution, the season, measurement noise level, and data used in the covariance estimation were also varied to evaluate the approach.

The temporal resolutions evaluated were 16-day, 8-day, 4-day, 2-day and 1-day intervals. These lengths were chosen to (1) identify the shortest time period for which meaningful global CO_2 maps can be obtained from OCO-2 observations and to (2) quantify the effect of temporal resolution, and thereby the amount of data and temporal variability within the time period, on prediction performance.

To explore the impact of seasonality on the heterogeneity of the atmospheric CO_2, cloud and aerosol distributions, one month was used as representative of each season (January, April, July, September). For example, April and July featured higher variability in the CO_2 concentration field than January and September.

A range of assumed measurement error levels was selected based on the expected performance of OCO-2. The levels of measurement noise are based on a single sounding expected OCO-2 measurement error standard deviation of 1.5ppm [D. M. O'Brien,

personal communication; *Crisp et al.*, 2004]), but accounting for the fact that a single model grid box may contain multiple OCO-2 soundings. Because nearby OCO-2 observations will likely have correlated errors, the effective measurement error at the grid scale will be higher relative to a case with independent measurement errors. The effective measurement error standard deviation at the grid scale is a function of the number of soundings and their spatial configuration within the grid cell, as well as the spatial scale over which the measurement errors are correlated. The number and spatial configuration of OCO-2 soundings was estimated by examining the range of the number, and the spatial configuration, of CALIPSO measurements with optical depths of less than 0.3 falling within a PCTM grid box. Simulated OCO-2 observations and measurement error correlation ranges from a few kilometers to a few hundred kilometers were used in a side study to determine the effective measurement noise at the scale of the PCTM model. Based on these results (not shown), a range of grid-scale measurement error standard deviations was applied, which were 0.2 ppm for the low level, 0.5 ppm for the medium level and 1 ppm for the high level. For all noise levels, the measurement errors were assumed to be independent zero-mean and normally distributed when applied at the scale of the model ($1^\circ \times 1.25^\circ$), and a random sample of such errors was added to the observations drawn from PCTM/GEOS-4. The nugget variance σ^2_{nug}, and therefore the diagonal elements of the matrix $\mathbf{R}$, defined in section 3.2.1 was thereby equal to the variances of these measurement errors (i.e., $(0.2 \text{ ppm})^2$, $(0.5 \text{ ppm})^2$ and $(1 \text{ ppm})^2$).

The fourth factor in the experimental setup was the data used in the covariance estimation (see section 3.2.1). Two cases were investigated. In the first case, the time-averaged full model data (e.g. Figures 3.1a–3.1c), i.e. the "truth", were used to derive the covariance parameters. In the second case, only the available observations (e.g. Figures 3.1d–3.1f) were used. Using the time-averaged full-model data represents an idealized, but not possible scenario, where the covariance structure could

be derived from the full time-averaged CO_2 concentrations. Clearly, having the true concentrations available to estimate the covariance structure for gap-filling CO_2 is not feasible and would defy the need to gap-fill, but this choice has been made to serve as an upper bound for any possible improvement over the observation-based covariance structure. The idea is that any alternative to using the observations themselves to quantify the covariance structure would be at best as good as having the "truth".

3.4 Results and Discussion

3.4.1 Qualitative features of the spatial predictions

The characteristics of the Level 3 maps as a function of the length of the examined time period, amount of measurement noise, and data used in the covariance estimation were similar across seasons (Figure 3.2). As expected, seasons with smoother CO_2 fields yielded better Level 2 maps. The large-scale features of the global CO_2 fields could be reproduced for all examined scenarios. It is surprising and encouraging that, even for the 1-day periods, the information content of the observations is sufficient to recover the main characteristics of the CO_2 field (Figure 3.1).

The third row in Figure 3.1 provides an example of gap-filled estimates for 1-day, 4-day and 16-day periods in April, which was the season with the most heterogeneous CO_2 field. As expected, some small-scale features are lost, especially in the 1-day maps, if they are not captured by observations. For example, the area of high CO_2 values over the northern part of South America is not well portrayed in the 1-day Level 3 map (Figure 3.1g). However, as is discussed in detail in section 3.4.3, the prediction uncertainties for the shorter time periods adequately reflect the true uncertainty of these predictions. So, while the predictions cannot recreate the small-scale features in areas missing observations, the associated prediction uncertainties are higher in these areas, and therefore reflect this lack of information.

The smoothness of the predicted fields varies as a function of the length of the examined time period. The 1-day and 2-day predictions are generally smoother than the truth, whereas for the longer time periods, most notably the 16-day periods, the predictions are less smooth than the truth. This can be seen in the undulating structure of the 16-day prediction map for April (Figure 3.1i). There are two different causes for this change of smoothness with temporal resolution. The reason for which the 1-day and 2-day maps appear smoother than the true fields is a general consequence of interpolating sparse data. The reason for which prediction maps for longer time periods appear less smooth than the truth is a consequence of unaccounted-for temporal variability in the CO_2 field, as reflected in the available observations. For the longer time periods, this effect dominates because the data density is relatively high, as is the amount of temporal variability that is captured by these observations. This temporal variability is introduced into the gap-filled maps because they combine observations from different days (see section 3.3.2). The amount of temporal variability that is captured by the observations increases with the time span over which observations are combined, and its effect therefore becomes more pronounced for longer time periods. In a spatial-only (compared to a spatio-temporal) geostatistical setup such as the one used here, the temporal variability translates to a perceived spatial variability on small-scales (Figure 3.1h and 3.1i). In contrast, the corresponding true fields shown in Figures 3.1b and 3.1c represent the temporal average over the examined time period and are smoother. The strength of this effect is further affected by the degree of measurement noise: the undulating structure is less pronounced in high measurement noise scenarios, where the measurement noise masks the temporal variability (see section 3.4.2).

3.4.2 Prediction accuracy

Figure 3.2 presents the Root Mean Square Prediction Error (RMSPE) for all modeled scenarios. RMSPE is a measure of the difference between the true and predicted CO_2 values. The overall range of RMSPE was 0.20 to 0.63 ppm CO_2; the lowest value resulted from a 16-day period in September and the highest from a 1-day period in July. Longer time periods and seasons with lower CO_2 variability generally had better prediction accuracies, i.e. lower RMSPE. These overall trends, however, depend on the level of measurement noise. For the 1-day periods, prediction accuracies improve as the measurement noise decreases. This ordered relationship is less evident in the 2-day periods, where the low and medium noise scenarios have similar prediction accuracies. For the 4-day periods, the medium measurement noise cases have the best prediction accuracies, but the differences are less pronounced than for other temporal resolutions. For the 8-day periods, the relationship between measurement noise and prediction accuracies starts to reverse: lower measurement noise is associated with worse prediction accuracies. This effect becomes fully evident in the 16-day periods, where higher measurement noise scenarios consistently feature the best prediction accuracies for all seasons, because temporal variability dominates the error. Overall, higher measurement noise decreases the prediction accuracies for shorter time periods, but, counter-intuitively, improves them for longer time periods.

This effect is due to the presence of temporal variability in the observations. As discussed in sections 3.3.2 and 3.4.1, temporal variability in the CO_2 distribution is captured by the observations by combining measurements from multiple days. This variability, however, is not accounted for directly by the spatial mapping approach presented here, which treats observations from different days as if they had been sampled from a static field. As a result, predictions may follow observations too closely to accurately represent the averaged field. This effect is alleviated in cases with high measurement noise, because the geostatistical modeling framework provides

leeway for the predictions to deviate from the observations to a degree consistent with the measurement error. In this way, accounting for high measurement noise implicitly also allows the method to cope with observed temporal variability. There is also an interaction between measurement error and the heterogeneity of the CO_2 field. Seasons with more spatial heterogeneity also exhibited more temporal variability. As a result, seasons with smoother CO_2 fields also yielded better prediction accuracies for longer time periods and lower measurement noise, relative to more heterogeneous seasons.

A second measure of prediction accuracy is the percentage of locations where the predicted values deviate from the truth by more than 1 ppm, with results (Figure 3.3) consistent with the RMSPE results. The lowest percentage was observed for the 16-day period with high measurement error in September, where only 0.2% of the predicted CO_2 values deviate from the truth by more than 1 ppm, and the highest percentage was for a 1-day period with high measurement error in July, where 9% of the predicted values deviated from the truth by more than 1 ppm. As seen previously, lower measurement noise improved the prediction accuracy for short periods, whereas higher measurement noise improved accuracies for long periods. For all cases, however, the percentages are quite low, indicating high accuracy predictions by the proposed method.

Surprisingly and encouragingly, whether the covariance structure was derived from the model data averaged over the examined time period, i.e. the truth that we are trying to estimate (e.g. row 1 of Figure 3.1), or from the available observations (e.g. row 2 of Figure 3.1), had little impact on the prediction accuracies (see Figure 3.2). This indicates that good predictions can be obtained without the need for prior information about the covariance structure of the underlying field. This was surprising especially for the shorter time periods, which had more limited observations, and indicated that data over short periods still contain enough information about the spatial variabil-

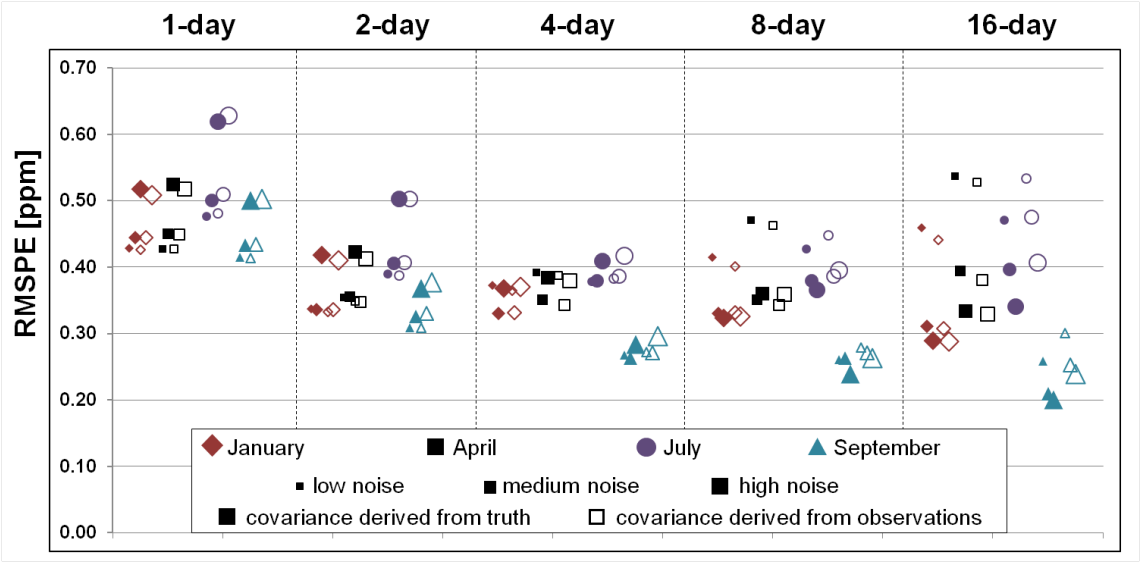

Figure 3.2: Root mean square prediction error (RMSPE) for 1-day, 2-day, 4-day, 8-day and 16-day gap-filled maps for January, April, July and September 2006. Symbols of different colors and shapes represent different seasons. The different measurement noise levels as discussed in section 3.3.2 are represented by different symbol sizes,whereas the filled and empty variations represent the two ways of calculating the covariance structure as detailed in the same section.

ity of the underlying field to yield accurate predictions. The only scenarios where deriving the covariance structure from the full model output (i.e. from prior information other than the observations) improved the prediction accuracies were some of the longer time periods; namely the 8-day and 16-day time periods for July and September. As described in detail in section 3.3.2, the averaged field over the time period investigated was defined as the truth, while the observations were aggregated from individual days, and thus did not come from an averaged field. Therefore, the observations come from a more variable field than the truth, and that variability is reflected in the estimated covariance structures, which translates into somewhat less accurate prediction accuracies for the longer time periods.

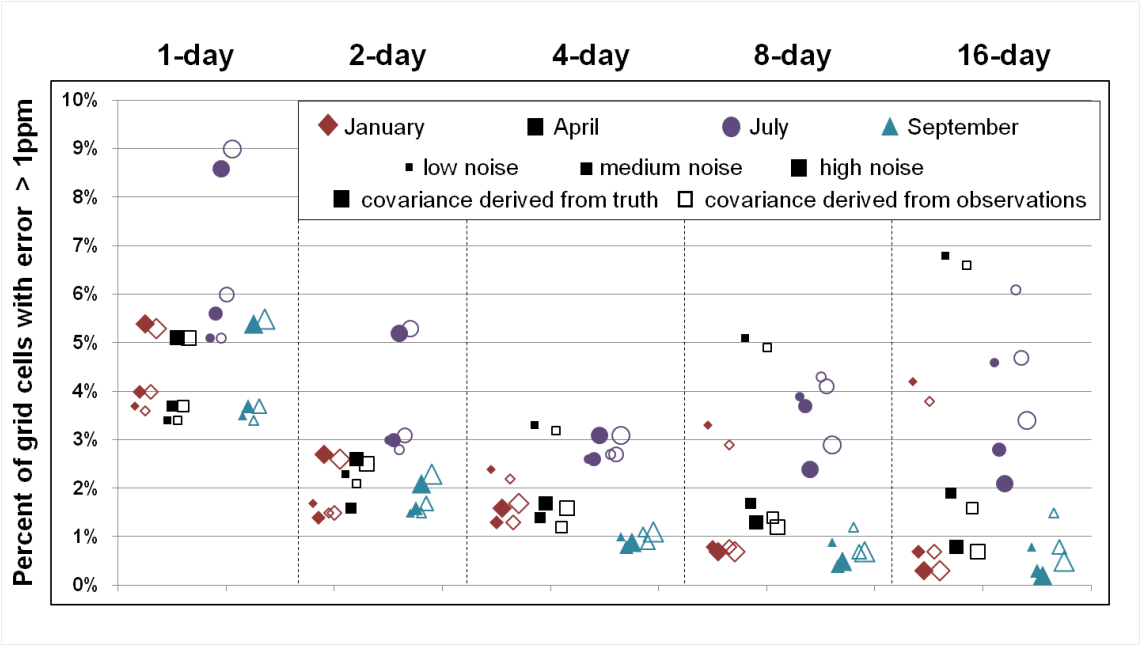

Figure 3.3: Percentage of locations where the predicted values deviate from the truth by more than 1ppm for 1-day, 2-day, 4-day, 8-day and 16-day time periods for January, April, July and September 2006. Symbols of different colors and shapes represent different seasons. The different measurement noise levels as discussed in section 3.3.2 are represented by different symbol sizes,whereas the filled and empty variations represent the two ways of calculating the covariance structure as detailed in the same section.

3.4.3 Prediction uncertainty

An attractive feature of geostatistical mapping is that each predicted CO_2 value is accompanied by a prediction uncertainty that is quantified without knowledge of the true distribution. The prediction uncertainty for a given location is a function of the location and number of observations surrounding the location, and the degree of spatial variability in the CO_2 field in the vicinity of the estimation location (equations (3.5) and (3.7)). In general, more homogeneous areas with dense observations will have lower prediction uncertainty.

The fourth row in Figure 3.1(j, k, and m) provides an example of the prediction uncertainties, as obtained from the approach implemented here, for the 1-day, 4-day and 16-day periods for April. The 1-day prediction uncertainties show clear evidence of the dependence of the prediction uncertainties on the location of observations. Locations that lie close to the satellite orbit path feature low uncertainties, while areas further away from the satellite paths have increasingly larger uncertainties. The 16-day period, which has a large number of observations distributed over the globe, features overall lower prediction uncertainties compared to the shorter time periods. Even for a temporal resolution of 16-days, however, some areas with few observations, such as West Africa and the polar regions, have higher prediction uncertainties.

Accurately assessing the uncertainty associated with predictions is valuable regardless of the ultimate use of the maps, but it is especially critical when the global gap-filled CO_2 predictions are compared to data from other sources such as model predictions. Realistic prediction uncertainties allow for probabilistic comparisons in addition to evaluating the best estimates. In order to assess how representative the prediction uncertainties were of the true uncertainty, the percentage of estimation locations where the truth fell outside of the estimated value ± 3 standard deviations (as calculated from the prediction uncertainty) was evaluated. The optimal percentage for this measure depends on assumptions about the underlying statistical distribution

of the data. As a guiding value, under the assumption of a normal distribution, this percentage should be approximately 0.3%. While achieving this exact value is not the goal, because the approach does not assume that the underlying distribution is Gaussian, we have assessed whether the percentage outside of ±3 standard deviations is reasonably low.

Figure 3.4 shows the percentage of locations falling outside of ±3 standard deviations of the prediction uncertainty for all investigated scenarios. The most striking feature of this figure is how the percentage dramatically increases with the length of the examined time period for low-noise scenarios, while the percentage stays low for high-noise scenarios. This feature is in accordance with the finding, discussed in detail in section 3.4.2, that high measurement noise can mask the temporal variability that is not otherwise accounted for by the spatial mapping. The 1-day scenarios, where temporal variability is minimal, have their lowest percentages for the low measurement noise cases. Starting with the 2-day temporal resolution, however, low measurement noise results in increasingly higher percentages of true values falling outside of ±3 standard deviations. For the high measurement error cases, accounting for the noise implicitly also accounts for the temporal variability and the percentages falling outside of ±3 standard deviations remain low.

The effect of the method used for deriving the covariance on the prediction uncertainty depends on the averaging time, but is overall small. For the 1-day periods, using only the observations to derive the covariance structure is clearly suboptimal. This is reflected in the higher percentage of locations falling outside of ±3 standard deviations (Figure 3.4). This is not such a clear-cut case, however, for the longer time-periods. While the truth-derived covariance structure still has the advantage of being based on a full field without gaps, it is possible that the observation-derived covariance results in improved prediction uncertainties by capturing some of the temporal variability present in the observations. This is indeed the case for some of the

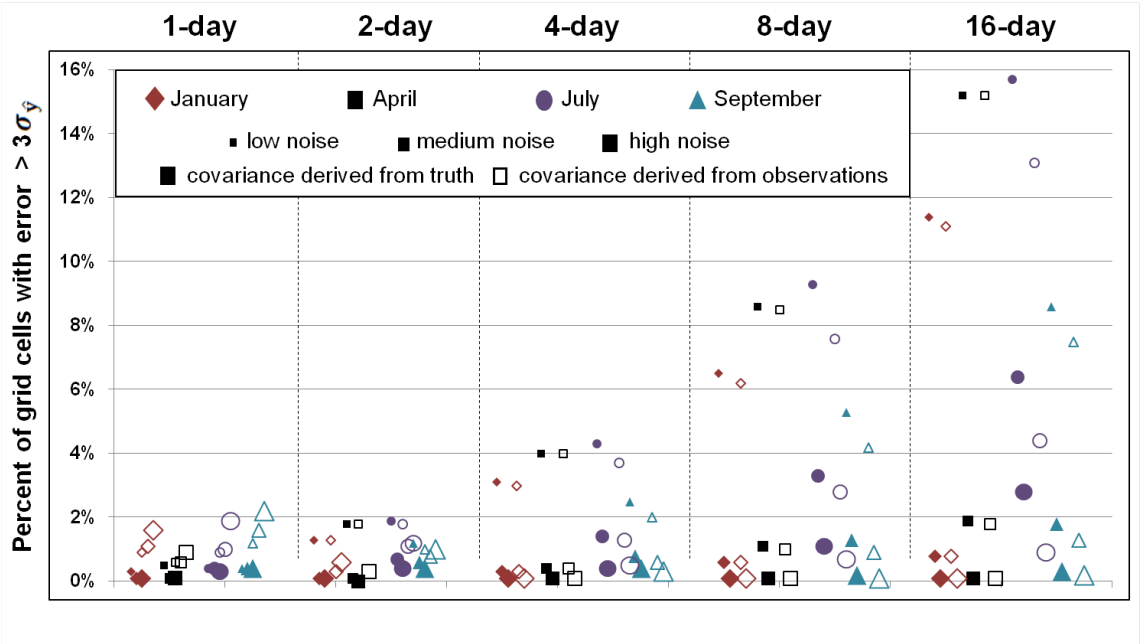

Figure 3.4: Percentage of locations where the predicted values deviate from the truth by more than ±3 standard deviations of the prediction uncertainty (eqn. (3.7)) for 1-day, 2-day, 4-day, 8-day and 16-day time periods for January, April, July and September 2006. Symbols of different colors and shapes represent different seasons. The different measurement noise levels as discussed in section 3.3.2 are represented by different symbol sizes,whereas the filled and empty variations represent the two ways of calculating the covariance structure as detailed in the same section.

8-day and 16-day. These improvements, however, were rather small compared to the differences caused by the varying degrees of measurement noise.

Overall, the prediction uncertainties are able to describe the true uncertainty accurately. This is an especially encouraging finding for the short time periods, because it indicates that satellite observations can be used to derive global CO_2 distributions with accurate uncertainties for time periods as short as one day. For longer time periods and low measurement noise scenarios, it is important to assess and incorporate the temporal variability resulting from the aggregation of observations to avoid an underestimation of the uncertainty. This could be achieved by either calculating the temporal variability and explicitly accounting for it in a geostatistical model, or by developing a spatio-temporal mapping approach.

3.4.4 Implications for the generation of Level 3 maps

It is challenging to construct Level 3 CO_2 maps that represent an average over a given time period using observations obtained on individual days, because CO_2 fields change with time. Ideally, the temporal resolution at which maps are obtained optimizes the mapping performance and provides maps that are representative over the shortest time period possible so as to capture the dynamics of the CO_2 distribution. The choice of temporal resolution thus defines a trade-off between having sufficient observations for adequate spatial coverage, while minimizing the impact of temporal variability. The findings described in sections 3.4.1 to 3.4.3 quantify this trade-off and provide guidance for choosing a temporal resolution for creating Level 3 products from satellite CO_2 observations from OCO-2.

When choosing a temporal resolution, results show that a key question is how the measurement noise compares to the temporal variability present in the estimated field. As a general guideline, the larger the measurement noise, the more advantageous it is to combine observations over a longer time period. For observations with low measurement noise, however, choosing a temporal resolution coarser than four days leads to decreased overall prediction performance.

Choosing a high temporal resolution, and thereby sacrificing spatial coverage by observations in favor of minimal temporal variability, can lead to surprisingly benign consequences in prediction performance. Even for the 1-day and 2-day periods, the RMSPE are on only the order of 0.5 ppm and 0.4 ppm, respectively. Furthermore, the accompanying prediction uncertainties accurately reflect the true uncertainty of the predictions.

Overall, for OCO-2 like observations, a temporal resolution of 4-days has the most robust prediction performance for varying seasons and measurement noise levels. Higher measurement noise shifts the optimal prediction performance towards lower temporal resolutions (i.e. longer time periods), while lower measurement noise shifts

it towards higher temporal resolutions (i.e. shorter time periods).

Whether the covariance structure is derived from the model data averaged over the examined time period (i.e. the truth that we are trying to estimate) or from the observations had very little impact on the quality of the Level 3 prediction and uncertainty maps. This finding strongly supports the use of observations for deriving the covariance structure, thereby avoiding the need for prior assumptions about the spatial structure of the CO_2 field.

3.5 Conclusions

High spatiotemporal resolution global Level 3 CO_2 products obtained from satellite observations offer new opportunities for gaining a better understanding of the distribution and dynamic behavior of atmospheric CO_2. Ideally, these Level 3 products should cover time periods that are short enough to preserve the synoptic dynamics of atmospheric CO_2concentrations. Knowledge of the uncertainties associated with statistically-derived Level 3 maps makes it possible to probabilistically evaluate CO_2 flux and atmospheric transport models, which can to help identify potential areas for improvement in model formulation and parameterization.

A common method for the generation of Level 3 maps is to obtain an aggregated field by spatial binning and averaging over long periods, which results in a loss of spatial resolution and dynamic information. While making monthly or seasonal maps might be adequate for more static properties (e.g. land cover, phenology), creating CO_2 maps over these long time periods hides the dynamics of the global CO_2 concentration field, which are critical to improving our understanding of the carbon cycle. Such averaged fields also typically lack quantitative uncertainty measures. The method presented in this study makes it possible to map CO_2 for time scales more consistent with the synoptic dynamics of CO_2, and provides a measure of the uncertainty associated with predictions. This proposed method makes minimal

assumptions, namely that the atmospheric CO_2 concentration exhibit spatial correlation, and that the statistical characteristics of this correlation can be inferred from the observations. Using only the observations themselves to infer the covariance structure eliminates the need to introduce any a priori assumptions about the distribution of atmospheric CO_2 concentrations, which in turn renders the methodology more useful for comparison purposes.

The methodology was used to evaluate Level 3 products derived from OCO-2-like data for time periods ranging from 1 to 16 days, with the dual goal of verifying the proposed method's performance and of identifying the optimal temporal resolution for Level 3 CO_2 products. The results indicate that global CO_2 concentrations can be predicted from OCO-2 satellite observations for time periods much shorter than a full repeat cycle. Even one-day prediction maps reproduce the large-scale features of the atmospheric CO_2 distribution and have realistic uncertainty bounds. Temporal resolutions of 2 to 4 days proved to have the most robust prediction performances over a wide variety of tested scenarios. The aggregation of observations over longer time periods introduces temporal variability that limits prediction performance, especially for scenarios where the measurement noise is low compared to the degree of temporal variability in the underlying CO_2 field.

CHAPTER IV

Global GOSAT CO_2 maps and model comparison

4.1 Introduction

The Greenhouse Gases Observing Satellite "Ibuki" (GOSAT) launched on January 23, 2009, and is the first space-based mission to reach orbit that was designed specifically for making high-precision measurements of carbon dioxide (CO_2) and methane (CH_4) with sensitivity in the lower troposphere [*Kuze et al.*, 2009; *Yokota et al.*, 2009]. After the launch failure of the Orbiting Carbon Observatory (OCO) mission [e.g. *Crisp et al.*, 2004], the OCO team was invited to join the GOSAT team in analyzing GOSAT observations, under the auspices of the NASA Atmospheric CO_2Observations from Space (ACOS) task. The ACOS GOSAT column CO_2 (X_{CO_2}) retrieval algorithm has now reached a level of maturity that makes it possible to use its estimates for informing carbon cycle science [*Crisp et al.*, 2012; *O'Dell et al.*, 2012]. Version 2.9 of the Level 2 data product, which represents geo-referenced X_{CO_2} observations, includes approximately 900 successful retrievals per three-day repeat cycle during the second half of 2009, the first period for which data are available. The majority of these observations are over land.

Although these data are useful in their own right, they have large gaps (e.g. Figure 4.1a and Figure A.1 in the auxiliary materials) and substantial retrieval uncertainties [*O'Dell et al.*, 2012], which makes it difficult to interpret their scientific

significance without further analysis. *Hammerling et al.* [2012] (see Chapter III) recently developed a statistical mapping approach that makes it possible to create full-coverage (i.e. Level 3) maps from satellite X_{CO_2} observations at high spatial and temporal resolutions. Unlike commonly used spatial and temporal binning and averaging procedures [e.g. *Crevoisier et al.*, 2009; *Kulawik et al.*, 2010; *Tiwari et al.*, 2006]), this approach exploits the spatial correlation among the Level 2 observations and the resulting Level 3 product describes the X_{CO_2} concentrations as a stochastic field characterized by its mean ("Level 3 estimates") and variance ("Level 3 uncertainties") structure.

Furthermore, unlike maps derived from inverse modeling or data assimilation studies [e.g. *Engelen et al.*, 2009], the *Hammerling et al.* [2012] approach draws information about the degree of spatial variability of X_{CO_2} directly from the X_{CO_2} observations, without additional information introduced from an atmospheric transport model or CO_2 flux estimates. As such, because no information from atmospheric transport models or CO_2 flux estimates is incorporated, the resulting Level 3 maps are a more direct representation of the information content of the retrievals. Rather than being intended as inputs to inverse modeling studies, these Level 3 X_{CO_2} products enable direct independent comparisons with existing models of carbon flux and atmospheric transport. The uncertainty measures provided by the approach make it possible to conduct these comparisons in a probabilistic framework.

Here we present global Level 3 X_{CO_2} products over land derived from the GOSAT ACOS X_{CO_2} retrievals, covering the second half of 2009. The Level 3 estimates and their associated uncertainties are compared to predictions for the same period from a combined CO_2 flux and atmospheric transport model using a probabilistic framework.

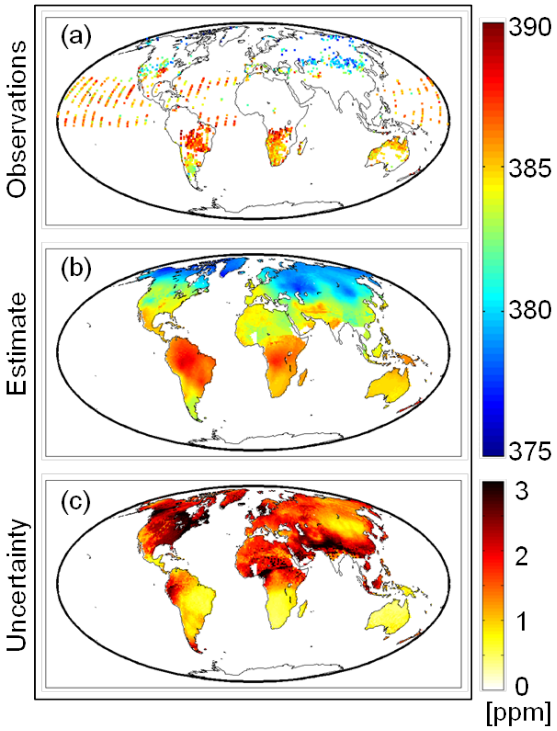

Figure 4.1: ACOS X_{CO_2} Level 2 data ("Observations"), ACOS X_{CO_2} Level 3 product ("Estimates") and estimated prediction uncertainties ("Uncertainty") expressed as a standard deviation for August 7–12 2009.

4.2 Data and Methods

4.2.1 GOSAT ACOS X_{CO_2} Level 2 data

GOSAT flies in a sun-synchronous orbit with an approximate 1pm equator-crossing time and has a three-day repeat-cycle. Version 2.9 of the GOSAT ACOS X_{CO_2} Level 2 data product is used in this study; only high (H) gain data were used as recommended in [*Crisp et al.*, 2012]. Figure 4.1a shows an example of six days (i.e., two repeat cycles) of ACOS L2 data for August 2009.

4.2.2 Method for creating global GOSAT ACOS X_{CO_2} Level 3 maps

The geostatistical methodology applied for creating Level 3 maps exploits the spatial correlation of the X_{CO_2} observations and consists of two major steps. In the first step, the spatial covariance structure of the X_{CO_2} observations is inferred from

these observations. In the second step, the inferred spatial covariance structure and the observations are used to estimate the X_{CO_2} field. The approach is described in detail by *Hammerling et al.* [2012] (see Chapter IV), and only key implementation details are presented here. Due to the currently limited availability of GOSAT ACOS X_{CO_2} observations over the oceans, the estimation has been restricted to land areas. The mapping is implemented on a 1° latitude × 1.25° longitude grid, to inform regional variability and to correspond with that of the model used for comparison in Section 4.2.1.

Based on previous work [*Alkhaled et al.*, 2008], an exponential covariance function is used to represent the X_{CO_2} spatial correlation:

$$C(h) = \sigma^2 \exp\left(-\frac{h}{l}\right), \tag{4.1}$$

where the covariance C is a function of the separation distance between locations (h), and spatially-variable variance (σ^2) and range (l) parameters that are inferred at each estimation location from the Level 2 data.

A local kriging procedure is then applied to create full-coverage maps, using a weighted average of available observations by solving the following linear system of equations once for each location on the Level 3 map:

$$\begin{bmatrix} \mathbf{Q}+\mathbf{R} & \mathbf{1} \\ \mathbf{1}^T & 0 \end{bmatrix} \begin{bmatrix} \boldsymbol{\lambda} \\ \nu \end{bmatrix} = \begin{bmatrix} \mathbf{q} \\ 1 \end{bmatrix}, \tag{4.2}$$

where $\mathbf{Q}$ is an $n \times n$ covariance matrix among the n observation locations, as defined in equation (4.1), $\mathbf{R}$ is an $n \times n$ diagonal matrix with the retrieval error variance specific to each observation on the diagonal, $\boldsymbol{\lambda}$ is a $n \times 1$ vector of weights, ν is a Lagrange multiplier and $\mathbf{q}$ is the $n \times 1$ vector of the spatial covariances between an individual estimation location and the observation locations, also defined using equation (4.1).

In our study, the measurement error variances are the squares of the reported ACOS Level 2 measurement error standard deviations adjusted by a factor of 2.1 as derived by *O'Dell et al.* [2012]. The predicted X_{CO_2} value, $\hat{y}$, and the prediction uncertainty, $\sigma^2_{\widehat{y}}$, at each Level 3 location are:

$$\widehat{y} = \boldsymbol{\lambda}^T \mathbf{y} \tag{4.3}$$

$$\sigma^2_{\widehat{y}} = \sigma^2 - \boldsymbol{\lambda}^T \mathbf{q} - \nu, \tag{4.4}$$

where $\mathbf{y}$ are the observations at the n Level 2 locations and σ^2 is the variance as shown in (4.1).

Based on previous work, a 2000 km neighborhood is required for assessing the local spatial variability ((4.1), also see *Hammerling et al.* [2012] (Chapter III) for details), and estimates can therefore only be obtained if there is a minimum of three observations within this distance of each estimation location. Estimation locations not meeting this requirement are shown as white in Figures 4.1b and A.2. It is the uncertainties in (4.4) however, that should be used as the criterion for limiting the coverage of Level 3 maps to regions where they are interpretable for a given scientific application (e.g. Figure 4.2), and one of the advantages of the method is the flexibility to dynamically define this uncertainty tolerance.

4.2.3 PCTM/GEOS-5/CASA-GFED model data

The modeled X_{CO_2} data used in the intercomparison are based on the Goddard Space Flight Center parameterized chemistry and transport model, which is driven by real-time analyzed meteorological fields from the Goddard Global Modeling and Assimilation Office, version GEOS-5, and uses biospheric fluxes produced from the Carnegie-Ames-Stanford-Approach, which incorporate biomass burning from the Global Fire Emissions Database (PCTM/GEOS-5/CASA-GFED), as well as oceanic,

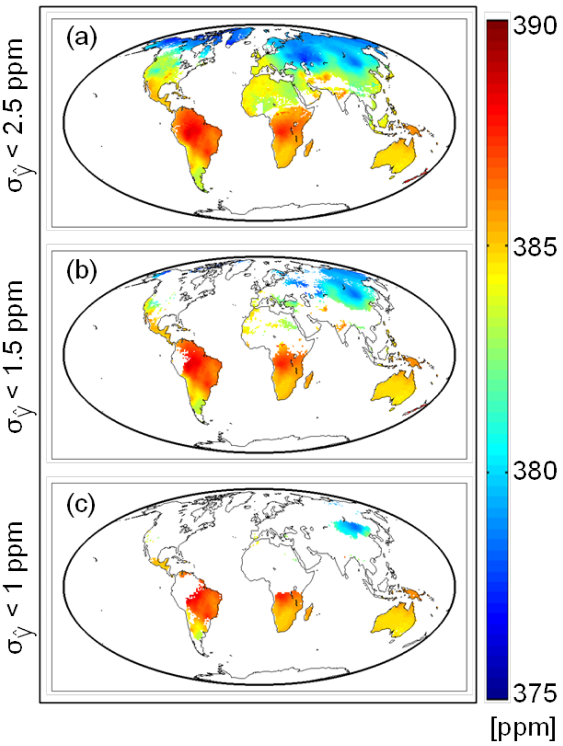

Figure 4.2: ACOS Level 3 X_{CO_2} map for August 7–12 (Figure 4.1b) filtered for locations where the standard deviations of the prediction uncertainties (Figure 4.1c) are less than 2.5ppm, less than 2ppm and less than 1ppm, respectively.

and anthropogenic CO_2 flux estimates, as described by *Kawa et al.* [2004, 2010]. The model resolution is $1° \times 1.25°$ with 28 vertical levels and hourly output. CO_2 mixing ratios were pressure-averaged to simulate the vertical sensitivity of the GOSAT observations. The PCTM/GEOS-5/CASA-GFED model has been widely tested, and has shown favorable results in carbon cycle comparison studies [e.g. *Kawa et al.*, 2010, and references therein].

4.3 ACOS GOSAT X_{CO_2} Level 3 maps

The choice of the temporal resolution, meaning the time period over which observations are aggregated, is an important decision in the creation of a Level 3 product [*Hammerling et al.*, 2012]. Ideally Level 3 products are created for the shortest time period possible to preserve as much of the short-term dynamical information as possible. However, this needs to be balanced with a minimum requirement for spatial coverage by the GOSAT observations. Based on initial investigations of temporal resolutions ranging from three days to one month, a resolution of six-days fulfilled both these objectives for all 30 six-day periods investigated from July to December 2009. Figure 4.1 provides an example of one of the investigated periods, August 7–12 2009. The Level 3 map (Figure 4.1b) for this period shows comparatively low X_{CO_2} in the Northern latitudes consistent with the knowledge of the effect of the seasonal cycle on CO_2 concentrations. The fact that the seasonal cycle in the Northern hemisphere is captured well in the GOSAT ACOS Level 3 maps becomes further evident from results from the full examined period (see Figure A.2 in auxiliary materials), which show a pronounced increase in CO_2 concentrations in the Northern latitudes in the winter months as well as a more subtle increase in the overall CO_2 concentrations. The comparatively high X_{CO_2} over South America visible in the Level 3 map for August 7–12 (Figure 4.1b) are a fairly persistent feature throughout the summer months (Figure A.2) and are further discussed in Section 4.4. An advantage of the mapping

method used in our study is that each estimate has an associated uncertainty measure (Figure 4.1c), which reflects the number of observations surrounding an estimation location, their retrieval errors, and the spatial variability in the X_{CO_2} field. Locations where the prediction uncertainties are below specific cut-off values are illustrated in Figure 4.2. For this six-day period, the predictions uncertainties are low for Australia, the southern part of Africa and eastern South America, whereas they are high for Southeast Asia, parts of India and the eastern United States and Canada. Analyzing these prediction uncertainties over extended time periods highlights the degree to which ACOS GOSAT retrievals constrain the X_{CO_2} distribution for different regions. Figure 4.3 summarizes this analysis for the 30 investigated six-day periods in 2009, identifying Australia, Southern Africa and a region in South America covering approximately eastern Brazil, Paraguay, Uruguay and central and northern Argentina and northern Chile as well-observed regions. Regions with the weakest constraint are the Sahara Desert and the high Northern Latitudes including Alaska, northern Canada, Greenland, Scandinavia and northern Russia. The interplay of how the number of observations, their retrieval errors, and the spatial variability in the X_{CO_2} field contribute to the uncertainty at each location renders it difficult to completely separate the effect of these contributing factors. The spatial coverage over the larger land masses in the Southern hemisphere, namely Australia, southern Africa and southern South America, is generally good. The number of observations decreases somewhat towards the end of the year, but these observations have lower retrieval errors and are supplemented by nearby ocean observations, which shift southwards in the second half of year as a function of the solar zenith angle. Southeast Asia and central and eastern China, on the other hand, have very poor coverage during July to October due to persistent cloudiness, but notably better coverage in November and December, leading to the mapping uncertainties being seasonally variable. The United States have generally good coverage, but the X_{CO_2} spatial variability over the Northern

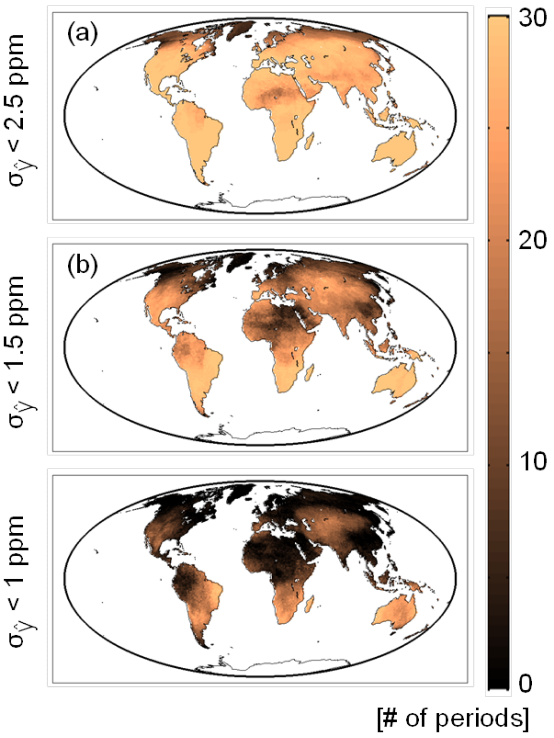

Figure 4.3: Summary of the analysis of prediction uncertainties from 30 6-day periods from July through December 2009. For each location, the number of 6-day prediction periods with prediction uncertainties below (a) 2.5 ppm, (b) 1.5 ppm and (c) 1 ppm, respectively, is shown. Lighter colors indicated regions which are better constrained by the GOSAT observations.

hemisphere land masses is rather high, yielding somewhat higher uncertainties for North America than for areas with comparable spatial coverage but less spatial variability such as Australia. There are no observations over the Sahara Desert, due to our exclusion of the GOSAT M-gain data (see [*Crisp et al.*, 2012] for details). The high Northern latitudes lack observations in November and December due to solar zenith angle restrictions; and the observations in July to October have comparatively high retrieval errors. This, coupled with the high X_{CO_2} spatial variability in the high Northern latitudes, leads to high mapping uncertainties even when data are present.

4.4 Comparison of Level 3 maps to modeled X_{CO_2}

The ACOS GOSAT X_{CO_2} Level 3 products can be used to conduct intercomparisons with models, by using the Level 3 data and their associated uncertainties to probabilistically identify areas where model outputs differ significantly from the Level 3 maps. Figure 4.4 shows an example of such an intercomparison to the PCTM/GEOS-5/CASA-GFED model for August 7–12 2009. The difference plot (Figure 4.4b) shows large differences in North America, the Amazon Region, and in a region covering the Northeastern part of India and Bangladesh. The standardized differences (Figure 4.4c), on the other hand, incorporate the Level 3 uncertainties, and can therefore be used to assess the significance of these differences given the information content of the satellite observations. For example, while the difference in North America and Southeast Asia might appear large in Figure 4.4b, they are not highly significant, as shown in Figure 4.4c. This is due to the comparatively large Level 3 uncertainties in these regions for this period. Figure 4.5 summarizes the intercomparison for July to December 2009, and reveals that discrepancies are most pronounced over South America for the Northern hemisphere summer months and shift to Asia in the Northern hemisphere fall. Although these results likely point to areas where the PCTM/GEOS-5/CASA-GFED model flux and transport processes need to be re-examined, Level 2 retrieval biases and, in the case of the sparsely-sampled Amazon region, underestimation of the Level 3 uncertainties due to low X_{CO_2} variability in surrounding well-sampled regions cannot be absolutely eliminated at this stage. It is also interesting to note that certain regions exhibit few or no limited significant differences over the entire examined period, including the high Northern latitudes, North America, Northern Africa, the Arabian Peninsula and Australia. The conclusion one can draw from an absence of statistically significant discrepancies depends on how well constrained a region is. For example, the high Northern latitudes are weakly constrained and have high mapping uncertainties. This implies that even large dis-

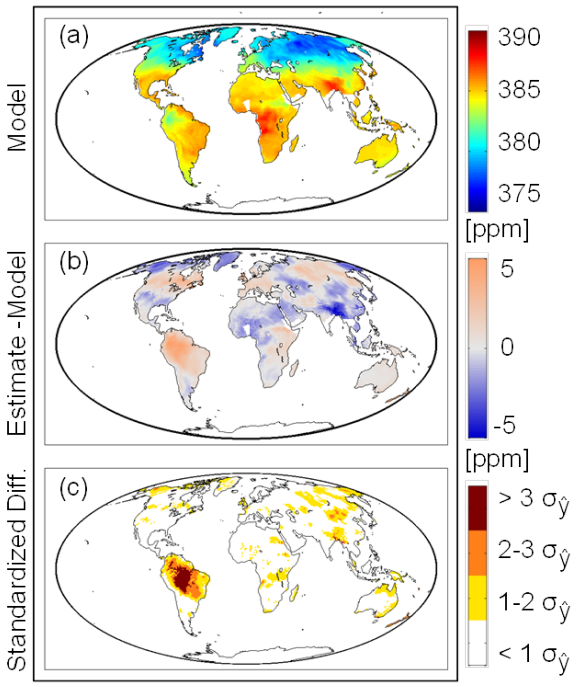

Figure 4.4: (a) PCTM model predictions for the same 6-day period as shown in Figure 4.1, (b) difference and (c) discretized standardized difference between the ACOS Level 3 map and the PCTM model. In the difference plot, values in the copper range indicate areas where the ACOS Level 3 values exceed the PCTM model predictions, values in the blue range areas where the PCTM model exceed the ACOS Level 3 values. The standardized difference is the absolute difference divided by the standard deviation of the prediction uncertainty at each location. The values are discretized to improve the visualization. Areas in yellow represent differences larger than one standard deviation of the prediction uncertainty, areas in orange larger than two standard deviations and areas in dark red larger than three standard deviations. The PCTM data has been mean-adjusted to the ACOS Level 3 predictions so that the global spatial average of the PCTM data and the ACOS Level 3 is equal.

crepancies are not conclusive because the power to detect a difference is low for that region. For Australia, on the other hand, the Level 3 uncertainties are rather low, so an absence of detectable discrepancies indicates that the Level 3 maps are indeed consistent with the model outputs.

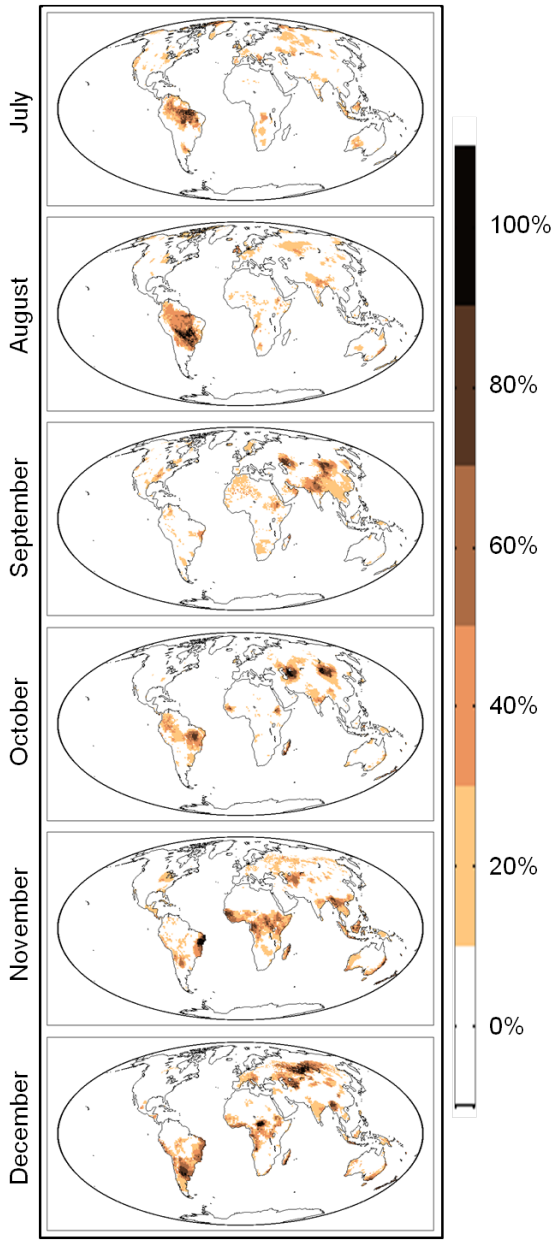

Figure 4.5: Percentage of 6-day periods within each month where the standardized differences exceed two prediction uncertainties. Given that there are only five 6-day periods in each month, a discretized color scale to visualize percentages has been chosen.

4.5 Conclusions

This section presents global X_{CO_2} Level 3 products over land based on the ACOS GOSAT X_{CO_2} data. The implemented approach [*Hammerling et al.*, 2012] yields maps at high spatial and temporal resolutions, using information derived directly from the Level 2 observations, without invoking an atmospheric transport model or estimates of CO_2 uptake and emissions. One limitation of such a purely observation-driven approach is that local enhancement phenomena that are not observed by the satellite cannot be fully captured. This results in Level 3 maps with smoother features than expected in the real X_{CO_2} concentration fields, but with uncertainty bounds that are wide enough to capture the range of likely variability. Level 3 maps for July to December 2009 at six-day resolution capture much of the synoptic scale and regional variability of X_{CO_2}, in addition to the overall seasonality. Results include robust uncertainty estimates, which reflect local data coverage, X_{CO_2} variability, and retrieval errors. Uncertainties are generally highest in the northern hemisphere in July and August, during the height of the growing season (Figure A.3), and lowest in areas with good data coverage and low CO2 variability in the Southern Hemisphere (Figure A.3). A probabilistic comparison to a state-of-the-art model reveals that the most significant discrepancies captured by the ACOS GOSAT Level 3 maps are in the South America in July and August, and central Asia in September to December (Figure 4.5). The differences in South America are significant in part because the Level 3 uncertainties are low in this region, and may reveal inaccuracies in carbon flux estimates for this region that is poorly constrained by in situ atmospheric CO_2 observations, although problems with the Level 2 retrievals and with identifying local phenomena in the Amazon region in the Level 3 products cannot be ruled out at this stage. Similarly, the significant differences in Asia appear during months when the Level 3 mapping uncertainties are lowest in this region (Figure A.3). These early results illustrate the usefulness of a high spatiotemporal resolution, data-driven Level

3 data product with uncertainty measures. Such a Level 3 data product can be used for direct interpretation of satellite observations, including those of highly dynamic parameters such as atmospheric CO_2, and for probabilistic comparison studies.

CHAPTER V

Signal detection for the ASCENDS mission

5.1 Introduction

The Active Sensing of CO_2 Emissions over Nights, Days, and Seasons (ASCENDS) mission is an active CO_2 sensing mission with an anticipated launch date of 2022. The term "active" refers to the measurement technology employed, which is based on lidar technology, where the instrument itself constitutes the light source. Passive missions such as GOSAT (see Section 2.3.2.2) and OCO-2 (see Section 2.3.2.1), on the other hand, require reflected sunlight. Notable features of this mission include the ability to sample at night and at high latitudes, conditions which are prohibitive to passive missions due to their reliance on reflected sunlight. The lidar measurement technique proposed for the ASCENDS mission further enables observing through some clouds and aerosols [e.g. *Ehret et al.*, 2008; *Mao and Kawa*, 2004], which represent obstacles for passive missions. Extensive instrument design research and development has already taken place and proof of concept and validation studies indicate that ASCENDS will be able to provide unbiased observations, i.e. observations without an offset based on atmospheric or land surface characteristics, with improved spatial coverage compared to active missions [e.g. *Abshire et al.*, 2010; *Kawa et al.*, 2010; *Spiers et al.*, 2011].

The primary goals of the ASCENDS mission as stated in "Earth Science and

Applications from Space: National Imperatives for the Next Decade" [*National Research Council*, 2007] (from hereon referred to as the decadal survey), cover some of the most relevant questions for understanding the carbon cycle, and are well aligned with the unique and advantageous capabilities of the lidar instrument CO_2 measurement technique. These goals have subsequently been refined in an ASCENDS mission NASA Science Definition and Planning Workshop [*ASCENDS Workshop Steering Committee*, 2008] and address open questions in carbon cycle science that pertain to potentially changing source/sink characteristics, which are difficult to constrain with other current or anticipated observations. These include changes in the Northern High Latitude sources and sinks, in Southern Ocean source/sink characteristics and in biospheric respiration processes [*ASCENDS Workshop Steering Committee*, 2008]. The Northern High Latitudes and the Southern Ocean are among the largest and most vulnerable carbon pools in the earth system, and it is crucial to detect and attribute changes in carbon fluxes from these pools quickly as they could lead to large increases in atmospheric CO_2 concentrations and subsequent shifts in climate dynamics [*Canadell et al.*, 2010]. Identification of human-generated CO_2 sources and sinks was also identified in the decadal survey as one of the potential benefits of the ASCENDS mission [*National Research Council*, 2007].

Guided by these stated goals, this study explores the extent to which the ASCENDS mission can indeed contribute to these pertinent carbon cycle science questions. The approach taken is to define scenarios that represent plausible changes in carbon fluxes within the time frame of the ASCENDS mission, i.e. about ten years from now, and investigate if the ASCENDS mission could detect the associated changes in atmospheric CO_2 concentrations. The scenarios are chosen to be representative of some of the key anticipated contribution areas of the ASCENDS mission. Three such prototypical scenarios have been identified: the melting of permafrost in the high northern latitudes, the shifting of fossil fuel emissions from Europe to

the P. R. of China and El Nino Southern Oscillation (ENSO) related changes in the sources/sink characteristics in the Southern Ocean. For each of these scenarios sets of fluxes have been specified by subject matter experts, which represent realistic pathways of how changes in carbon fluxes could unfold. For the remainder of this thesis these fluxes are referred to as perturbation fluxes. They are added to a set of baseline fluxes, which represent a perturbation-free scenario. The baseline fluxes are common to all three perturbation scenarios.

These three scenarios are used to design Observing System Simulations Experiments (OSSEs) to investigate if the ASCENDS mission, once operational, has the ability to corroborate the predicted unfolding of these scenarios. The approach used in this work falls under the framework of signal detection studies, i.e. experiments that investigate if the signature of the perturbation fluxes corresponding to the three investigated scenarios can be detected in the ASCENDS observations of atmospheric CO_2 concentrations. This is a two-fold approach, where the strength and location of the gradients in the atmospheric CO_2 concentrations resulting from the changes in carbon fluxes is first investigated. The presence of gradients in the atmospheric CO_2 concentrations is what carries information about the changes in carbon fluxes. Secondly, it is investigated to which degree future ASCENDS observations can detect the signal, i.e. the differences in atmospheric CO_2 concentrations between the baseline and the perturbation runs.

A signal detection study for the ASCENDS mission has been conducted previously by *Kawa et al.* [2010], who investigated the ability of the ASCENDS mission to detect differences between the day and night-time CO_2 concentrations. The objective of the *Kawa et al.* [2010] study was similar, namely to investigate if changes in atmospheric CO_2 concentrations resulting from variations in fluxes can be detected via ASCENDS observations. The scope of the investigated scenarios and the detection methodology, however, differ notably between the studies. *Kawa et al.* [2010] found that the de-

tection of the diurnal differences proved difficult due to the small magnitude of the signal. This is a feature that all three scenarios investigated in this work also have in common: the magnitude of the signal, i.e. the change in atmospheric CO_2 concentrations corresponding to the perturbation fluxes, is small; it is approximately one tenth of a percent, or less, of the background concentration. The signal detection methodology applied in this study is based on geostatistical mapping, which can leverage the information content of several observations concurrently, which potentially enhances the ability to detects signals.

5.2 Study design, data and mapping methodology

The study is designed to evaluate the ability of the ASCENDS mission to detect plausible CO_2 flux perturbations in the atmospheric CO_2 signal. The evaluation is conducted by obtaining ASCENDS-like observations globally from a baseline model run (without the flux perturbation) and from a model run with the flux perturbation and identifying if and where the resulting global CO_2 concentrations are significantly different using a geostatistical mapping and probabilistic comparison methodology.

5.2.1 Simulated ASCENDS CO_2 observations

The parameterized chemistry and transport model (PCTM) is used to produce a simulated distribution of atmospheric CO_2 variability in space and time [*Kawa et al.*, 2004]. Model transport is driven by real-time analyzed meteorology from the GEOS-5 MERRA data assimilation [*Rienecker et al.*, 2011]. CO_2 surface fluxes for the baseline run include terrestrial vegetation physiological processes and biomass burning from CASA-GFED3 [*Randerson et al.*, 1996; *van der Werf et al.*, 2010], ocean fluxes from *Takahashi et al.* [2002], and fossil fuel burning from the CDIAC database [*Andres et al.*, 2009]. CASA fluxes are driven by MERRA data and modulated 3-hourly in the method of *Olsen and Randerson* [2004]. PCTM CO_2 output has been extensively

compared to in situ and remote sensing observations at a wide variety of sites, and in most cases the model simulates diurnal to synoptic to seasonal variability with a high degree of fidelity [e.g. *Bian et al.*, 2006; *Kawa et al.*, 2004; *Law et al.*, 2008b; *Parazoo et al.*, 2008].

For the simulations here, the model is run on a $1^\circ \times 1.25^\circ$ latitude/longitude grid with 56 vertical levels and hourly output using 2007 meteorology and flux settings. Perturbation flux scenarios are described below in Section 5.3.1. Pseudo-data observations are extracted from the model output at the nearest time and interpolated in latitude/longitude to the ASCENDS sample locations (see below). A vertical weighting function, appropriate to the ASCENDS lidar wavelength, is applied to the model pseudo-data profile to produce column average mixing ratio values.

Prospective ASCENDS sampling and measurement error characteristics are derived from model output and observations in a method similar to that of *Kawa et al.* [2010] for a laser instrument operating near 1.57 um. The CALIPSO orbital track is used to simulate the ASCENDS orbit, and the CALIPSO measurements of total cloud and aerosol optical depth (OD) are used to calculate the ASCENDS laser attenuation. CALIPSO travels in the so-called 'A-train' orbit, which is a likely orbit placement for ASCENDS as well. CALIPSO OD data are reported every 5 km along track and this forms our basic ASCENDS sample set. As stated above, the synthetic CO_2 value is then derived by interpolating the model output in latitude/longitude to the ASCENDS sample locations.

Surface lidar backscatter (β), also needed for error estimation, follows from MODIS measured spectral reflectance over land and the glint formulation of *Hu et al.* [2008] over water using daily MERRA 10-m wind speeds. Surface reflectivity over land is interpolated from MODIS (Terra + Aqua) 5-km, 16-d composite nadir BRDF-adjusted reflectance data at 1.64 μm (band 6), which are available every 8 days [*Schaaf et al.*, 2002]. Land reflectance is scaled by a factor of 1.23 to account for the land hot spot

backscatter effect [*Disney et al.*, 2009], i.e., $\beta/sr = 1.23 \cdot \alpha/\pi$. Backscatter values of 0.08 and 0.01 are used to fill missing areas of MODIS data over land and over snow/ice, respectively, where ice and snow cover are determined from MERRA data.

In order to make the study method applicable for a range of possible CO_2 laser sounder instrument implementations, the errors are scaled globally to a nominal error value for clear-air conditions at Railroad Valley, NV ($\beta = 0.176$) and a 10-s sample integration. 10 seconds is the nominal averaging time of the CO_2 laser sounder [e.g. *Abshire et al.*, 2010; *Kawa et al.*, 2010]. Thus, a given instrument model can be characterized by its random error at this reference point and the global distribution of errors estimated from OD and beta. The individual sounding errors at the 5 km CALIPSO resolution are calculated using:

$$\sigma_{5\mathrm{km}} = \frac{3.667 \cdot \sigma_{\mathrm{ref}}}{\left(\dfrac{\beta \cdot T^2 \cdot sdf}{0.176}\right)^{1/2}}, \tag{5.1}$$

where σ_{ref} is the 10 second reference instrument random error at Rail Road Valley, β is the backscatter, T the transmittance, *sdf* the surface detection frequency and 0.176 the Rail Road Valley clear air transmittance and backscatter reference value at 1.57 μm, which corresponds to one of the potential ASCENDS instrument designs [*Abshire et al.*, 2010]. The transmittance is calculated from the optical depth (OD) using $T = e^{-OD}$.

Soundings with an optical depth greater than 0.3 or where the surface detection frequency equals 0 are filtered out and considered 'not retrieved' based on the limited performance of the retrievel algorithm at high optical depth values. For this study a 10-s along-track average is used as the pseudo-data measurement granule [*Kawa et al.*, 2010]. The 10 second observation errors are then calculated by summing all the 5 km errors corresponding to each 10 second time interval and dividing this sum by the square root of the number of retrieved soundings, which implies the assumption of

independence of errors between individual soundings. Using this setup the maximum number of soundings constituting one observation is 14. For the medium and high noise scenario, the reference instrument random errors (σ_{ref}) are 0.5 and 1 ppm, respectively. Once the measurement error has been determined for each location following the procedure described above, a random sample from a normal distribution with a standard deviation corresponding to the measurement error is drawn and added to the PCTM model CO_2 value to define an observation. Figure 5.1b provides an example of four days of global observations.

5.2.2 Mapping methodology

Geostatistically-derived global mapped ("Level 3") data products are used for the comparison. Individual observations contain large gaps and high measurement errors such that meaningful spatially-comprehensive comparisons at synoptic timescales are often precluded. Advantages of using mapping products compared to the observations directly include that the comparisons can be conducted globally at synoptic time scales and that the uncertainties of the mapped products are often lower by leveraging the information content of many observations concurrently, which in turn improves detectability. The geostatistical mapping methodology described in Chapter III is applied to derive global CO_2 maps with uncertainties from the simulated observations. The mapping methodology is described in detail in Chapter III and only aspects specific to this study are discussed here.

Specific to this study, the observations used in the analysis are filtered to those with a measurement error standard deviation below a certain threshold motivated by improved robustness in the covariance estimation procedures and computational efficiency in the overall procedure. Applying a measurement error threshold is analogous to imposing a quality criterion when delivering remote sensing products instead of making all retrievals available and results in improved robustness in the estima-

tion procedure and computational efficiency. For the medium (high) measurement error setup this threshold is 1.5 (3) ppm, so the same set of observation locations is used for both setups. This choice represents an balance between spatial coverage and robustness of the covariance estimation procedure and was determined in a side study (results not shown). In addition to the medium and high noise setups, there is also a "no error" setup, which is only used as a theoretical best case. In this setup, observations at the same locations as for the medium/high measurement setup are used, but without any noise added. This case is included to be able to isolate potential limitations of the methodology and the spatial coverage from those related to the instrument capabilities.

As discussed in Chapter III and Chapter IV, ideal mapping periods are at synoptic time scales between two and six days depending on measurement noise and other mission details. One of the challenges in mapping CO_2 satellite observations is that observations capture a specific instant in time whereas the mapped products are ideally representative of the average concentrations over a time period. Based on preliminary studies evaluating mapping performance for different time periods, 4-day periods have been found to lead to optimal mapping performance for ASCENDS observations. Figure 5.1 shows an example of a 4-day (August 1–4 2007) period. The full model is just shown for reference; only the observations are used in the mapping procedure. Each 4-day period is mapped independently. For January only six 4-day periods were mapped due to missing CALIPSO data, for all other months seven 4-day periods were mapped for a total of 83 4-day mapping products for each of the baseline and perturbation cases. These mapping products were then used as input data in the subsequent comparison analysis described in Section 5.3.2.

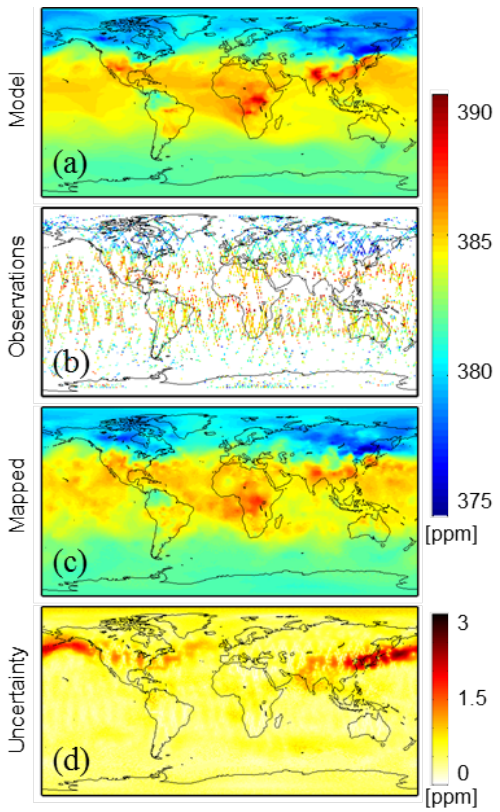

Figure 5.1: (a) Modeled CO_2 concentrations ("Model"), (b) simulated ASCENDS observations ("Observations"), (c) mapped CO_2 concentrations ("Mapped") and (d) mapping uncertainties ("Uncertainty") expressed as a standard deviation for August 1–4 2007.

5.3 Perturbation flux scenarios and comparison methodology

5.3.1 Perturbation flux scenarios

The perturbation flux scenarios are based on pertinent questions in carbon cycle science, which are connected to the ASCENDS mission goals. They represent quantitatively plausible scenarios of changes in carbon fluxes that could occur around the year 2022 based on current understanding. We use them as prototypical examples of flux patterns that give rise to the types of signals the ASCENDS mission endeavors to detect. Details on the choice of the perturbation fluxes are discussed in the individual sections below. From a methodological point of view, the perturbation fluxes represent the source of the signal we are trying to detect. They were added to the baseline fluxes described in Section 5.2 and transported analogous to the baseline fluxes using the PCTM/GEOS5 modeling framework. The atmospheric CO_2 concentrations resulting from these perturbation fluxes are the signal to be detected, i.e. the to-be-detected signal is the difference in atmospheric CO_2 concentrations between the baseline and the perturbation runs.

5.3.1.1 Permafrost carbon release

The carbon currently stored and immobilized in the permafrost soils of the high Northern latitudes represents one of the largest and the most vulnerable carbon reservoirs [e.g. *Canadell et al.*, 2010; *Lemke et al.*, 2007; *Schaeffer et al.*, 2011]. A melting of the permafrost and subsequent release of carbon could lead to large increases in atmospheric CO_2 concentrations and an abrupt shift in climate dynamics [*Canadell et al.*, 2010]. The permafrost carbon release experiment uses the fluxes described by *Schaeffer et al.* [2011]. The permafrost carbon release is based on anticipated melting of permafrost as a result of increasing temperatures in the high Northern latitudes caused by climate change [*Schaeffer et al.*, 2011]. The fluxes for the year 2022 have

been used as the perturbation fluxes, with the 2020 and 2021 fluxes used for two spin up years. A spin up period has been used to avoid an abrupt increase in fluxes and work with distribution patterns that are based on more realistic gradual increases in carbon fluxes. According to [*Schaeffer et al.*, 2011] 2020 marks the year when the tundra melting fluxes surpass the background noise; and they increase from then onwards.

Figures 5.2a and 5.2c show the average perturbation fluxes for May through July and the whole year, respectively. A year-round time series plots of the monthly flux is provided in the left panel of Figure A.4. As can be observed in Figures 5.2a, 5.2c and A.4, the sign of the perturbation fluxes is strictly positive, corresponding to the release of carbon from permafrost. The magnitude of the release picks up in June, peaks in September and ebbs down again towards the end of the year in correspondance with the seasonal change in temperature.

5.3.1.2 Fossil fuel emissions

The fossil fuel flux perturbation scenario consists of a shift of fossil fuel emissions from Europe to the P.R. of China. A shift that is in directional agreement with recent trends in these regions. Fossil fuel emissions from the P.R. of China have been increasing rapidly over the last decades, with the P.R. of China now being the largest emitter of fossil fuels worldwide [*Olivier et al.*, 2012; *Peters et al.*, 2011], whereas fossil fuel emissions from Europe have seen a 3% decrease in 2011 and an overall downward trend over the last two decades [*Olivier et al.*, 2012]. Two different settings for the emission shift were used, from here on referred to as the "lower" and "higher" signal. The lower signal represents a 20% decrease of European emissions which equates approximately to a 12% increase in China. The higher signal, a 2.5-fold amplification of the lower signal, represents a 50% decrease of emissions in Europe which corresponds approximately to a 25% increase in China. All the percentage

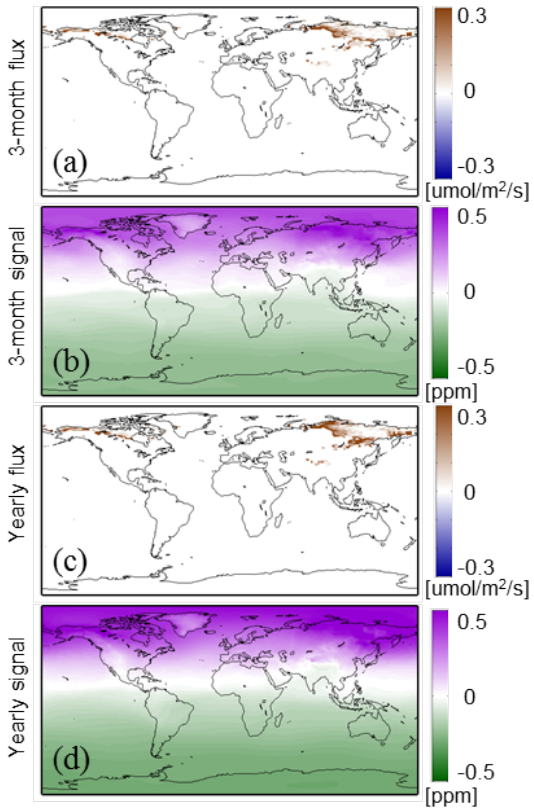

Figure 5.2: (a) 3-month average CO_2 flux("3-month flux"), (b) 3-month average CO_2 concentration ("3-month signal"), (c) yearly average CO_2 flux ("Yearly flux") and (d) yearly average CO_2 concentration ("Yearly signal") for the permafrost carbon release experiment. The 3-month period is May through July. The flux is modeled for 2022. The negative concentration values in the Southern hemisphere are a result of the global mean adjustment.

changes are in reference to 2007 emission levels. The two settings represent two points on a continuum of possible emission changes around the year 2022 and we use them as examples to draw broader conclusions on the detectability of these types of signals as characterized by their the spatial and temporal patterns and their magnitudes.

The calculations are based on the v2011 2007 fossil fuel emissions from the CDIAC data base [*Andres et al.*, 2011]. So, for example for the lower signal case, the European fluxes are reduced by 20% for each month and the total flux amount corresponding to this decrease is added to Chinese fluxes. The decrease and increase is conducted proportionally to the existing spatial pattern of the fluxes for each month, thereby preserving the spatial and temporal patterns within the European and Chinese fluxes. The setup is designed to be flux neutral globally, i.e. the difference in the global atmospheric CO_2 concentrations is zero. So the signal to be detected is a difference in the global spatial distribution of CO_2 concentrations, while the global mean remains unchanged. Figures 5.3a and 5.3c show the average higher fossil fuel perturbation fluxes for August through October and the year, respectively. Figures 5.4a and 5.4c show the analogous fluxes for the lower signal case. Year-round time series plots of the monthly fluxes for the strong and weak signal cases are provided in the left panels of Figures A.5 and A.6, respectively. In these figures, it can be seen that the fluxes vary little from month to month. They also exemplify that the strong signal is simply an amplification of the weak signal.

5.3.1.3 Southern Ocean

The Southern Ocean is a region of special interest to carbon cycle science; it is a region where carbon fluxes are highly uncertain [*Gruber et al.*, 2009], while also being a region with apparent high sensitivity to climate change [*Le Quéré et al.*, 2007] and the potential to substantially affect the carbon cycle given half of the annual ocean uptake of anthropogenic emissions occurs in the Southern Ocean [e.g. *Le Quéré et al.*,

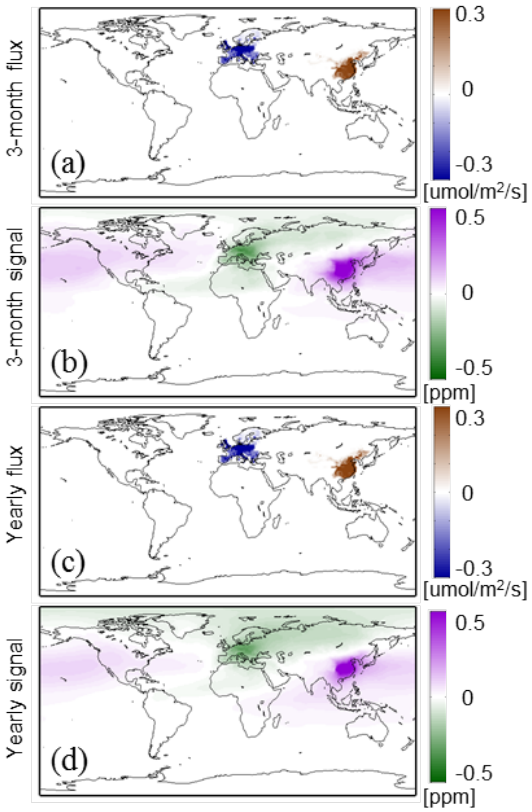

Figure 5.3: (a) 3-month average CO_2 flux ("3-month flux"), (b) 3-month average CO_2 concentration ("3-month signal"), (c) yearly average CO_2 flux ("Yearly flux") and (d) yearly average CO_2 concentration ("Yearly signal") for the higher fossil fuel experiment. The 3-month period is August through September.

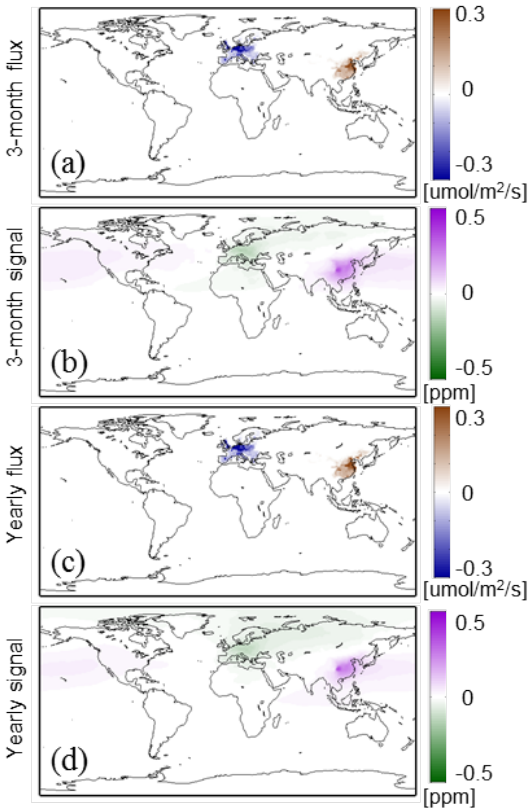

Figure 5.4: (a) 3-month average CO_2 flux ("3-month flux"), (b) 3-month average CO_2 concentration ("3-month signal"), (c) yearly average CO_2 flux ("Yearly flux") and (d) yearly average CO_2 concentration ("Yearly signal") for the lower fossil fuel experiment. The 3-month period is August through September.

2007; *Meredith et al.*, 2012]. It is also a very sparsely sampled region, where the ability of the ASCENDS mission to observe at high latitudes could provide valuable insights. Such insights can not be provided by satellites that rely on reflected sunlight, and are hence limited in their ability to observe at high latitudes. It is currently not known if the Southern Ocean is a source or sink region [*Gruber et al.*, 2009] and there is disagreement on the current and future trend of the carbon flux in the Southern Ocean [*Law et al.*, 2008a; *Le Quéré et al.*, 2007].

Variations in climatic modes are one of the key drivers of interannual variability in ocean carbon exchange [*Field et al.*, 2007]. Before attempting to address questions of a potential change in sink/source characteristics of the Southern Ocean using satellite observations, it is sensible to evaluate to which extend interannual variability due to variations in climatic modes can be detected. A natural first step is to assess if ASCENDS can detect changes in carbon flux associated with the El Nino Southern Oscillation (ENSO) mode. To that end, the years 1977 and 1979 were chosen as they represent a large difference in the ENSO phase.

The Southern ocean fluxes used for this scenario are based on a hind cast simulation of the Community Climate System Model ocean Biogeochemical Elemental Cycle model as described by *Doney et al.* [2009]. The fluxes were obtained at $1^\circ \times 1^\circ$ spatial and monthly temporal resolution. The monthly differences between the Southern ocean flux anomalies for 1977 and 1979 are considered the perturbation fluxes for this scenario. A year-round time series of these monthly perturbation fluxes is shown in the left panel of Figure A.7. Figures 5.5a and 5.5c show the average fluxes for April through June and the year, respectively. It can be observed that the magnitude of the yearly perturbation flux is very low. One other feature that distinguishes the Southern Ocean experiment from the other two experiments is that the magnitude, and even the sign, of the perturbation flux varies by month and by sub-region (see Figure A.7).

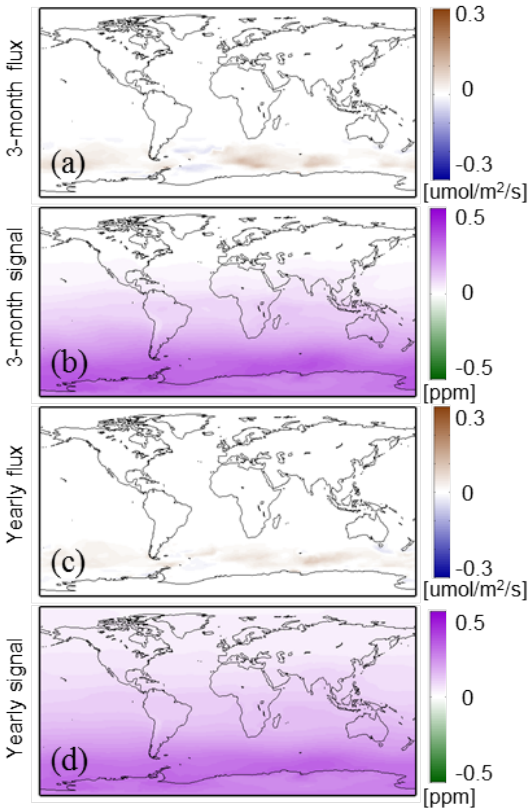

Figure 5.5: (a) 3-month average CO_2 flux ("3-month flux"), (b) 3-month average CO_2 concentration ("3-month signal"), (c) yearly average CO_2 flux ("Yearly flux") and (d) yearly average CO_2 concentration ("Yearly signal") for the Southern Ocean experiment. The 3-month period is April through June.

5.3.2 Comparison methodology

The detectability of a signal is determined by identifying if and where the mapped concentrations from the baseline run are significantly different to those from the perturbation run. First, the difference between the mapped concentrations from the baseline run and the perturbation run is calculated. Then the uncertainty of the difference is calculated; expressed as a standard deviation this uncertainty is the square root of the sum of the estimation variances of the baseline and the perturbation mapped products as shown in the following equation:

$$\sigma_{\text{diff}} = \left(\sigma^2_{\widehat{y}_{\text{base}}} + \sigma^2_{\widehat{y}_{\text{per}}}\right)^{1/2}. \tag{5.2}$$

The significance of a difference is determined by comparing the size of the difference to the uncertainty of the difference. There is considerable measurement error noise induced variability in individual 4-day mapping products, which can be reduced by averaging the mapped concentrations from multiple 4-day periods and using the resulting average in the comparison. It is important to conduct the mapping at 4-day resolution to capture synoptic scale variability rather than agglomerating observations over longer periods and mapping them than directly, which would preclude the ability to capture short-term variability. Hence, when conducting this comparison over multiple periods, the means over multiple 4-day periods of the mapped baseline concentrations and of the mapped perturbation concentrations, and their respective uncertainties are used in the comparison. Under the assumption of temporal independence the uncertainty of the temporal mean (expressed as a variance) is the mean mapping variance of the individual periods divided by the number of periods:

$$\sigma^2_{\bar{\widehat{y}}} = \frac{\overline{\sigma^2_{\widehat{y}_i}}}{n}, \tag{5.3}$$

where $i = 1, \ldots, n$ is the index for the time periods included in the mean. The assumption of temporal independence was evaluated by conducting temporal variogram analyses for sets of mapping errors at randomly selected locations, and no compelling indication to contradict this assumption was found. For the permafrost carbon release scenario the concentrations of the baseline run were mean-adjusted to the mean of the perturbation run by applying a multiplicative adjustment. This adjustment preserves the spatial patterns of the baseline run, while creating a setup where the global difference in concentrations between the baseline and perturbation run is zero, so a flux neutral scenario. This has been done to avoid simply detecting the overall increase in CO_2 concentrations as a result of the strictly positive perturbation fluxes over the two years of model spin-up and over the investigated year. Without a mean adjustment, a signal corresponding to the increase in global mean would be detected globally and overshadow other differences in gradients.

5.4 Results and Discussion

On a high level, one can view the query of detecting flux perturbations as two distinct if connected questions. The first question is to which degree characteristics of the flux perturbations are translated to, and preserved in, the atmospheric CO_2 concentrations, i.e. what is the signature (or signal) of a set of flux perturbations of interest in the atmospheric CO_2 concentrations. The second question is how well a given observing system, in our case the ASCENDS mission, can capture the presence of this flux perturbation signal. Both of these aspects are discussed in the following sections, which are organized by the three investigated scenarios.

5.4.1 Detectability of permafrost carbon release

The detectability of the presence of a significant signal per se is relatively straight forward in the case of the anticipated permafrost carbon release (Figure 5.2). The

interesting challenge is to devise a signal detection strategy that enables detection of longitudinal and latitudinal gradients compared to just detecting a signal manifested as a zonal increase. The spatial gradients in the atmospheric CO_2 concentrations carry information about the magnitude and location of the carbon fluxes. While signal detection is not directly targeted at quantifying carbon fluxes, insights on the detectability of spatial gradients are highly relevant for studies targeting flux detections, e.g. inversions. With this informational purpose in mind, signal detection is ideally done in a manner to optimally preserve the spatial gradients. One way to achieve this is through judicious choice of the temporal aggregation periods over which the comparisons are conducted. As descibed in Section 5.3.2, temporal aggregations of 4-day maps are used in the comparison. Surprisingly, gradient-preserving signal detection for the permafrost scenario is more easily achieved by using a shorter rather than longer aggregation period and choosing the right season as will be described below.

The year-round monthly time series plots of the permafrost carbon release concentration signal shown in the right panel of Figure A.7 provide a visual explanation for this phenomenon. The concentration signal is at its height around September, or even later in the year, when most of the melting has occurred. Interestingly though, the concentration signals most indicative of the spatial pattern of the tundra melting fluxes occur in the late spring/early summer months before the effects of atmospheric mixing take over. By August, atmospheric mixing, which occurs rapidly in the Arctic, causes the spatial signature of the tundra melting fluxes to be replaced by the dominating signal of a zonal increase. Some further evidence of this phenomenon can be observed by comparing Figures 5.2b and 5.2d: the 3-month signal retains more of the spatial characteristics of the source flux, whereas the yearly signal represents a zonal increase where the elevated concentrations have spread towards the pole. This phenomenon is caused by the specific combination of the temporal pattern of

the permafrost carbon release and rapid atmospheric mixing in the High Northern Latitudes.

Figure 5.6 shows a summary of the detection results for the permafrost carbon release scenario. Rows one and two show the mapped concentrations and the significance of the difference to the baseline run for May through July, respectively. Rows three and four show the analogous results for the year. While the 3-months results feature comparatively more noise, the recognition of the spatial pattern in the significance plots is also improved. Even for the high noise scenario, the pattern in the 3-months significance plot indicates that the origin of the signal is land-based compared to the purely zonal increase visible in the yearly plots. The results for the different noise levels are as expected; lower noise provides a more accurate and less noisy mapped concentration field. In summary, the permafrost melting is detectable for both levels of measurement noise considered, where spatial gradients are best detected using two to three month aggregation periods in the late spring/early summer.

5.4.2 Detectability of changes in fossil fuel emissions

Figures 5.3b and 5.3d show the atmospheric CO_2 concentration signal for August through October as well as the yearly average for the higher fossil fuel signal experiment. Figures 5.4b and 5.4d show the analogous concentrations for the lower fossil fuel signal experiment. The right panels in Figures A.5 (higher signal) and A.6 (lower signal) show year-round time series plots of the monthly atmospheric CO_2 signal. As can be seen in these figures, atmospheric transport leads to some variations in the monthly patterns of the atmospheric concentrations, but overall the nature of the European and Chinese emission signals is still local with a pronounced spatial signature even in the yearly average. This is a result of the fluxes being comparatively localized.

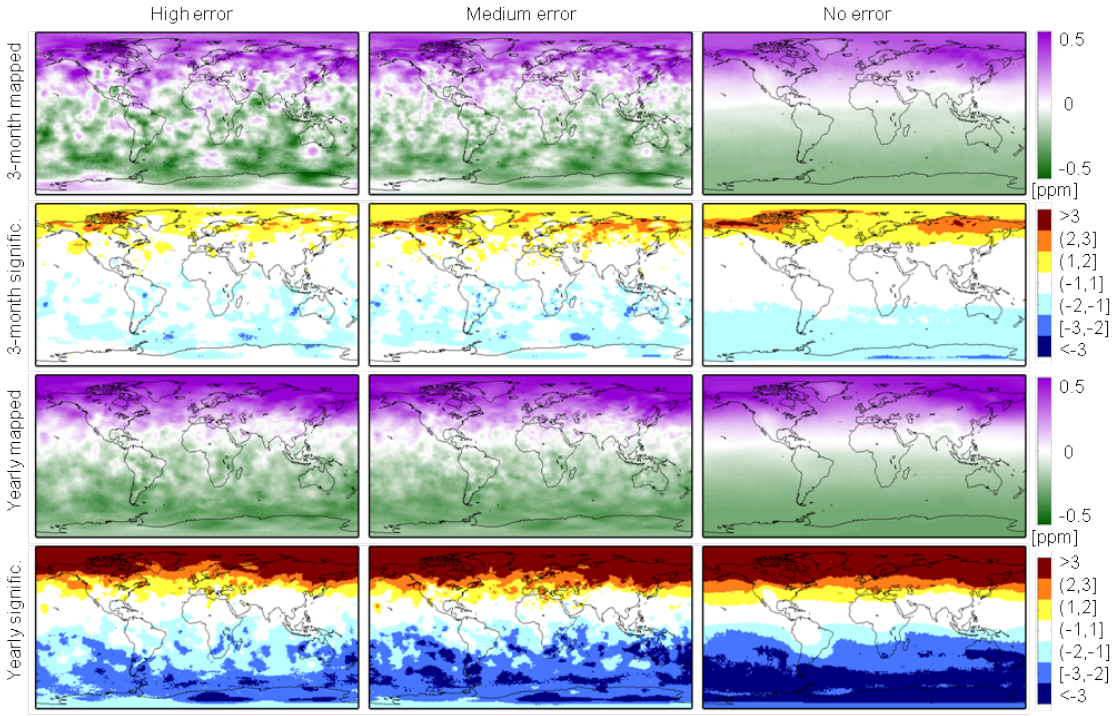

Figure 5.6: Results for the permafrost carbon release experiment. First row: 3-month mapped CO_2 signal ("3-month mapped"). Second row: Significance of the 3-month mapped CO_2 signal ("3-month signific."). Third row: Yearly mapped CO_2 signal ("Yearly mapped"). Fourth row: Significance of the yearly mapped CO_2 signal ("Yearly signific."). The mapped signal is the difference between the mapped perturbation CO_2 concentration and the mapped baseline CO_2 concentration. The significance is the mapped signal divided by the uncertainty of the mapped signal. The values are discretized for improved visualization. Yellow, orange and dark red (light, medium and dark blue) represent areas where the mapped perturbation concentration is larger (smaller) than the mapped baseline concentration by more than one, two or three standard deviations, respectively, of the uncertainty of the mapped signal.

This is in contrast to the other two experiments (see Figures 5.2d and 5.5d) where the detailed spatial signatures are largely lost and the yearly signals represent primarily zonal increases. Another feature that these plots illustrate is that the magnitude of the weak fossil fuel perturbation signal is very low. The low magnitude, combined with its small spatial extent, renders the weak fossil fuel signal the most difficult to detect among the investigated scenarios, which exemplifies the challenge of detecting small and localized concentration changes from satellite observations.

Figure 5.7 shows a summary of the detection results for the higher fossil fuel scenario. Rows one and two show the mapped concentrations and the significance of the difference to the baseline run for August through October, respectively. Rows three and four show the analogous results for the year. Figure 5.8 shows the same results for the lower fossil fuel scenario. One aspect that these results highlight, and which makes intuitive sense given the nature of the fossil fuel signal, is that averaging over longer time periods improves detectability. Compared to the other two investigated scenarios, the fossil fuel signal is fairly steady in space and time. Although atmospheric transport clearly plays a role, the atmospheric signal remains indicative of the source region of the perturbation flux throughout the seasons. Figures 5.7k and 5.7l, for example, show evidence that areas are being detected as significant other than the source regions of the emissions. However, given the higher significance of the source region and the characteristic patterns, this does not obscure the source region of the perturbation fluxes.

The effect of varying measurement noise levels on the detectability is as expected; increasing measurement noise leads to higher noise and decreased significance in the results and requires in turn longer averaging periods. For the higher signal all three noise levels capture the signal in the yearly results, which is not the case for the lower signal, where only the no error case clearly captures the signal. There is some evidence that a significant signal is starting to emerge in the yearly medium and high

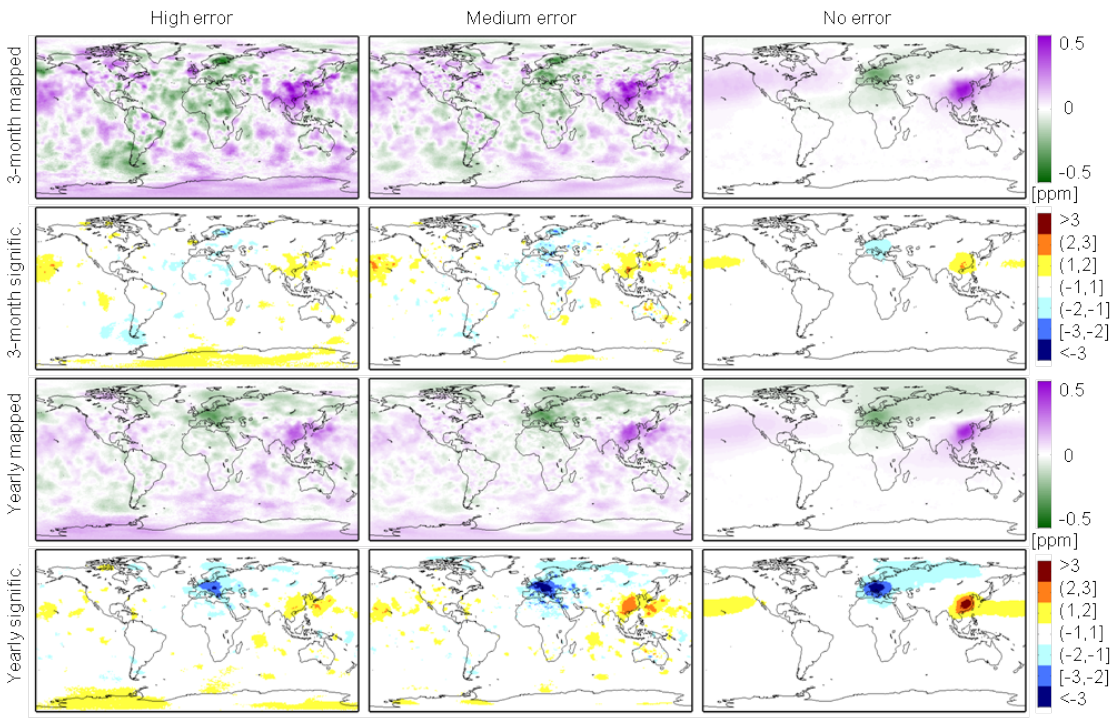

Figure 5.7: Results for the higher fossil fuel experiment. First row: 3-month mapped CO_2 signal ("3-month mapped"). Second row: Significance of the 3-month mapped CO_2 signal ("3-month signific."). Third row: Yearly mapped CO_2 signal ("Yearly mapped"). Fourth row: Significance of the yearly mapped CO_2 signal ("Yearly signific."). The mapped signal is the difference between the mapped perturbation CO_2 concentration and the mapped baseline CO_2 concentration. The significance is the mapped signal divided by the uncertainty of the mapped signal. The values are discretized for improved visualization. Yellow, orange and dark red (light, medium and dark blue) represent areas where the mapped perturbation concentration is larger (smaller) than the mapped baseline concentration by more than one, two or three standard deviations, respectively, of the uncertainty of the mapped signal.

error measurement noise cases, and given the nature of the signal discussed above, the signal is expected to appear more clearly when averaging over periods exceeding the one year period considered in this study. Overall, these findings imply that ASCENDS can in principle detect anthropogenic signal components, but depending on the strength of the signal, detection might require multiple years. It is hence feasible that ASCENDS can serve to validate anthropogenic emission changes over the course of its mission, but is likely not ideal as the primary monitoring device of such signals.

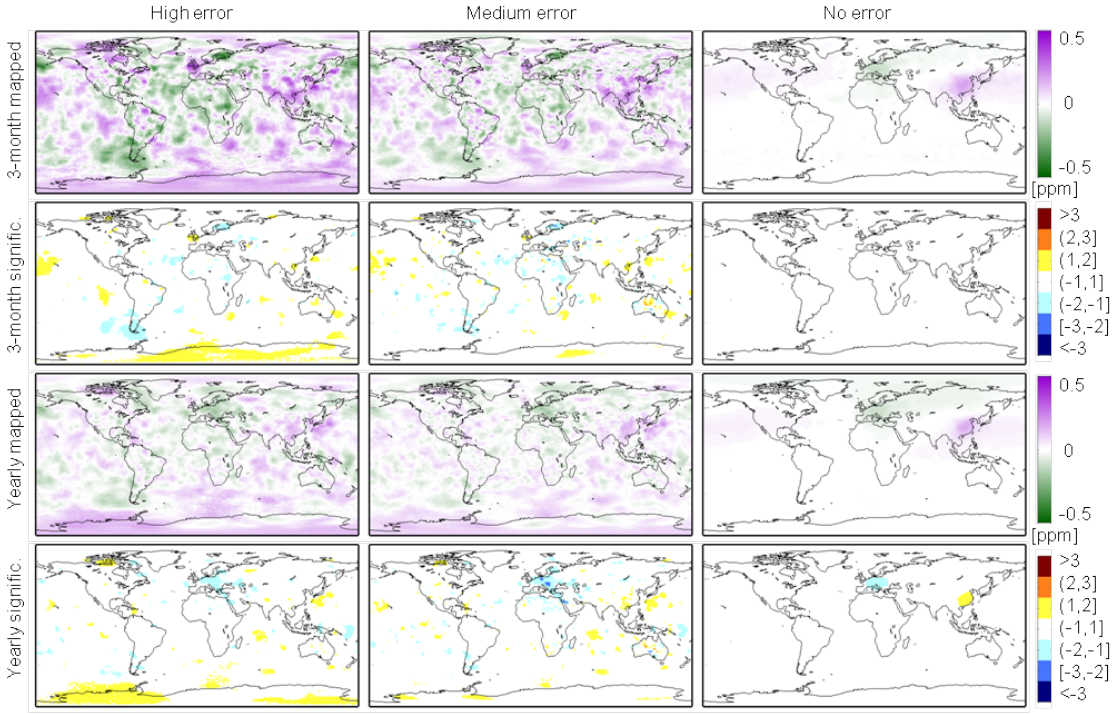

Figure 5.8: Results for the lower fossil fuel experiment. First row: 3-month mapped CO_2 signal ("3-month mapped"). Second row: Significance of the 3-month mapped CO_2 signal ("3-month signific."). Third row: Yearly mapped CO_2 signal ("Yearly mapped"). Fourth row: Significance of the yearly mapped CO_2 signal ("Yearly signific."). The mapped signal is the difference between the mapped perturbation CO_2 concentration and the mapped baseline CO_2 concentration. The significance is the mapped signal divided by the uncertainty of the mapped signal. The values are discretized for improved visualization. Yellow, orange and dark red (light, medium and dark blue) represent areas where the mapped perturbation concentration is larger (smaller) than the mapped baseline concentration by more than one, two or three standard deviations, respectively, of the uncertainty of the mapped signal.

5.4.3 Detectability of changes in Southern Ocean source/sink characteristics

Of all the investigated scenarios, the approach to detect changes in the Southern Ocean source/sink characteristics is the least obvious. This is caused by a confluence of different factors. The overall magnitude of the signal in the Southern Oceans is rather weak, with the absolute value of the signal never exceeding 0.4ppm. In addition to a seasonal pattern in the fluxes and concentrations, there is a spatial and temporal high-frequency change in the anomaly fluxes (and in a damped version in the concentration fields), which adds a component of variability that is not present in the fairly consistent (fossil fuels) or gradually changing (tundra melting) flux or concentration patterns of the other two experiments (Figure A.7).

Atmospheric mixing also plays a role insofar as it obscures the origin of the signal being the Southern Oceans compared to a zonal increase ranging all the way to the pole. This occurrence is analogous to the phenomenon described in Section 5.4.1 regarding the effects of atmospheric mixing on the detectability of the spatial pattern of the permafrost carbon release. However, applying the remedy of using a shorter averaging period before atmospheric mixing hides the origin of the signal, is not as clear-cut for the Southern Ocean scenario as it is for the permafrost carbon release, where the magnitude of the signal is stronger. As can be seen in Figure A.7, which shows year-round time series plots of the monthly flux and atmospheric CO_2 signal, the months, which preserve the origin of the perturbation fluxes best, are the spring and early summer month. Later in the year, although the concentration signal is stronger, the concentration increase has spread pole wards and is less indicative of the origin being the Southern Ocean.

Figure 9 shows a summary of the detection results for the Southern Ocean scenario. For all measurement noise setups, the yearly results clearly indicate a zonal increase in the High Southern Latitudes. However, it is less clear if the pattern is indicative

of the Southern Ocean being the source region within the zonal band. An argument could be made that the spatial pattern of the 3-month results (Figures 5.9d, 5.9e, 5.9f) is more indicative of the Southern Ocean as the source region compared to a zonal increase. The 5-month results (not shown) for April through August are even more indicative of the Southern Oceans being the source region. Conducting analyses over periods of multiple lengths, and drawing conclusions from the joint picture emerging from these analyses, appears to be the most beneficial approach for the Southern Ocean scenario. In summary, ASCENDS can detect a Southern Ocean signal representative of differences due to natural variability in the ENSO climatic mode. Due to the low magnitude and internal small scale variability within the fluxes giving rise to the signal, however, the primary detection is a zonal increase.

5.4.4 Limitations of the study

This study has some important limitations. For each scenario, the only flux component that is varied is the flux component under investigation. All other fluxes are assumed to be known. We introduce some additional variability by adding random noise to both the baseline and perturbation cases, but that might not be adequate compensation for the potential lack of knowledge of the other flux components. In addition to considering all flux components other than the one under investigation known, in the scenarios we only look at the signal from one changing flux component in isolation. In reality, many changes might occur simultaneously and the resulting CO_2 concentration signal patterns might overlap, which makes signal detection more challenging. This could impact the conclusions of this study insofar that it would be more difficult to link detectable signals with the underlying change in fluxes.

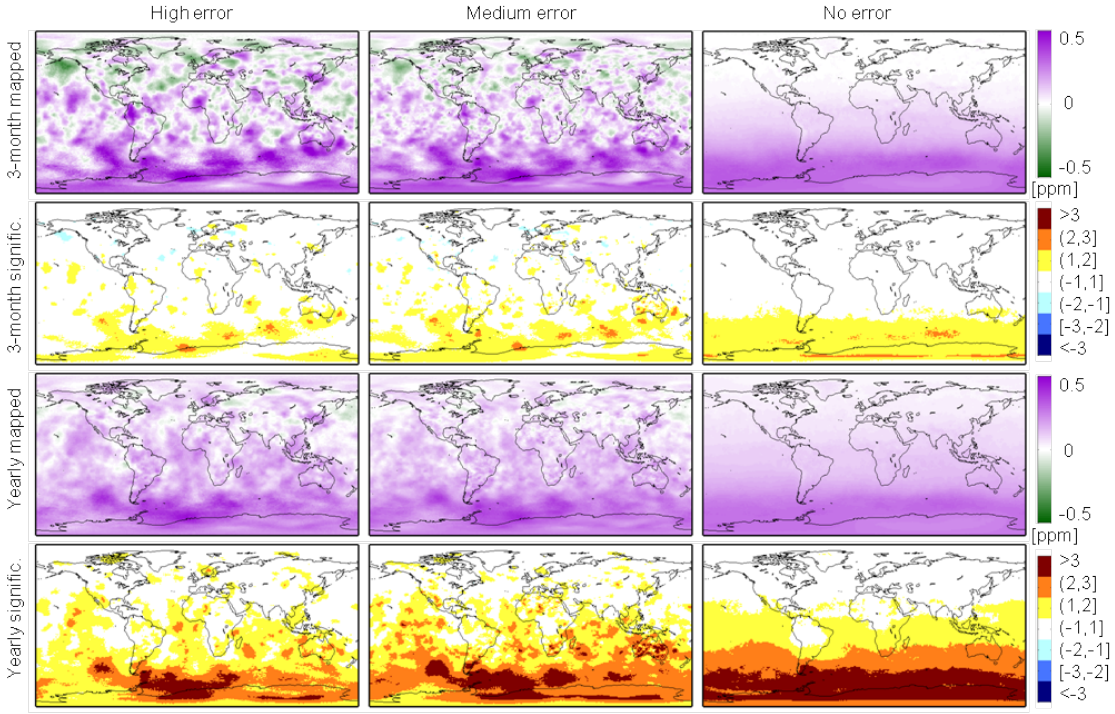

Figure 5.9: Results for the Southern Ocean experiment. First row: 3-month mapped CO_2 signal ("3-month mapped"). Second row: Significance of the 3-month mapped CO_2 signal ("3-month signific."). Third row: Yearly mapped CO_2 signal ("Yearly mapped"). Fourth row: Significance of the yearly mapped CO_2 signal ("Yearly signific."). The mapped signal is the difference between the mapped perturbation CO_2 concentration and the mapped baseline CO_2 concentration. The significance is the mapped signal divided by the uncertainty of the mapped signal. The values are discretized for improved visualization. Yellow, orange and dark red (light, medium and dark blue) represent areas where the mapped perturbation concentration is larger (smaller) than the mapped baseline concentration by more than one, two or three standard deviations, respectively, of the uncertainty of the mapped signal.

5.5 Conclusions

ASCENDS is a planned lidar CO_2 satellite mission which is expected to contribute to improving our understanding of the carbon cycle. To assess some of these expected contributions, three prototypical scenarios of scientific and societal relevance were investigated: the release of carbon due to the melting of permafrost in the high Northern latitudes, the shifting of fossil fuel emissions from Europe to the P.R. of China, and ENSO related changes in the sources/sink characteristics in the Southern Ocean. A common feature of these scenarios is that the CO_2 signal is small; in terms of absolute magnitude the signals strength is approximately one tenth of a percent of the background concentrations. These three scenarios were used to design OSSEs for signal detection studies to investigate if the ASCENDS mission has the ability to detect the unfolding of these scenarios compared to a baseline scenario. Two different levels of measurement noise and a no measurement noise reference case were investigated. The specific signal detection approach applied in this study uses a geostatistical mapping methodology that can leverage the information content of nearby observations, thereby potentially facilitating enhanced signal detection.

The results indicate that the ASCENDS mission can in principle detect the types of signals investigated in this study. The permafrost melting was quite easily detectable in the form of a zonal increase. Spatial gradients were best detected using two or three month aggregation periods in the late spring/early summer. For the Southern Ocean scenario, differences due to the natural variability in the ENSO climatic mode were also detectable as a zonal increase. The magnitude of the signal, however, is much smaller than the permafrost melting signal. Spatial and temporal high-frequency changes in the Southern Ocean anomaly fluxes add an additional component of variability to the signal. Detecting more detailed gradients than a zonal increase proved hence challenging for the Southern Ocean scenario; conducting analyses over periods of multiple lengths and analyzing them jointly provides a possible

strategy to capture them. The fossil fuel emission detectability is directly related to the strength of the signal and the level of measurement noise. As is true for all scenarios, the effect of varying measurement noise levels is as expected: increasing measurement noise levels lead to decreased significance in the results and require in turn longer averaging periods. For the higher fossil fuel emission signal all three noise levels capture the signal, which is not the case for the lower signal, where only the no error case clearly captures the signal. The emergence of a detectable signal, however, indicates that averaging over periods longer than the one-year period considered in this study would also render signals of the magnitude of the lower fossil fuel emission signal detectable.

CHAPTER VI

Conclusions

6.1 Conclusions

Carbon dioxide (CO_2) is the most important anthropogenic greenhouse gas contributing to climate change, which has numerous, and potentially grave, impacts for life on earth. With anthropogenic CO_2 emissions and accumulation rates in the atmosphere still on the rise, understanding the processes that drive the carbon cycle, and their future functioning, is a more important scientific and societal challenge than ever. The advent of satellite observations of CO_2 offers novel and distinctive opportunities for gaining an improved quantitative understanding of the processes driving the carbon cycle. This dissertation contributes to realizing these opportunities.

This dissertation had three specific objectives: 1) Developing and evaluating a mapping methodology for deriving global atmospheric CO_2 concentrations and uncertainties from satellite observations, 2) Deriving high resolution CO_2 concentration maps from GOSAT observations and using the mapped products for model comparison studies and 3) Evaluating the ability of the ASCENDS mission to detect signals in atmospheric CO_2 concentrations resulting from changes in carbon fluxes. The key findings from these three objectives are summarized in the next paragraphs.

The high-level conclusions for objective 1 are that the method developed in this dissertation makes it possible to map CO_2 for time scales consistent with the syn-

optic dynamics of CO_2, and can provide uncertainties that correctly reflect the true uncertainty of the mapped concentrations. The method makes minimal assumptions, namely that the atmospheric CO_2 concentrations exhibit spatial correlation, and that the statistical characteristics of this correlation can be inferred from the observations. The method is hence highly suitable to create observation-based CO_2 mapping products which are independent of carbon flux and transport assumptions. The results of the simulation study indicate that for OCO-2 even one-day maps reproduce the large-scale features of the atmospheric CO_2 concentration field and have realistic uncertainty bounds. Temporal resolutions of two to four days proved to have the most robust prediction performances, assessed in terms of prediction accuracies and uncertainties, over a wide variety of tested scenarios.

The conclusions for objective 2 include that GOSAT-based CO_2 concentration maps for July to December 2009 at six-day resolution capture much of the synoptic scale and regional variability of CO_2, in addition to the overall seasonality. Uncertainties are generally highest in the northern hemisphere in July and August, during the height of the growing season, and lowest in areas with good data coverage and low CO_2 variability in the Southern Hemisphere. A probabilistic comparison to the PCTM/GEOS-5/CASA-GFED model, a state-of-the-art coupled carbon flux and atmospheric transport model, revealed that the most significant discrepancies captured by the GOSAT maps occur in South America in July and August, and central Asia in September to December. The results illustrate how the mapping products developed in this dissertation can be used for direct interpretation of CO_2 satellite observations through probabilistic model comparison studies.

A key conclusion for objective 3 is that the signals associated with all three investigated scenarios can in principal be detected by the ASCENDS mission. The ability to detect these signals, and the strategy to do so, is intrinsically linked to how the carbon flux perturbations translate into atmospheric CO_2 concentrations, and this

translation is highly dependent on the specific characteristics of the perturbations. Permafrost melting and Southern Ocean flux perturbations both resulted in spatially-dispersed zonal increases due to rapid atmospheric mixing in the high latitudes. These zonal increase are fairly easily detectable. The spatial gradients in the atmospheric CO_2 concentrations are what contains the information about the fluxes, so in these cases, the challenge is to detect the signal in such a manner that the spatial gradients of the signal are preserved in addition to a zonal increase. This is best done by using an investigation period of a few months in the spring and early summer rather than an entire year. Applying this strategy, the permafrost carbon release is comparatively easy to detect, while the Southern Ocean perturbation is more difficult. The fossil fuel emissions scenario investigated, a shift from emissions from Europe to the P.R. of China, resulted in locally elevated CO_2 concentrations with little seasonal changes. This due to the fact that the seasonal variations in the perturbation fluxes themselves are comparatively small and the atmospheric mixing is slower in the midlatitudes. In this case the optimal detection strategy is more straightforward: longer averaging periods improve the detectability. A shift of fossil fuel emissions from Europe to China corresponding to a 50% decrease in Europe is clearly captured by ASCENDS observations, a smaller shift corresponding to a 20% decrease in Europe requires an averaging period longer than one year to become detectable. The overall findings are that the ASCENDS will be able to contribute to detecting changes in carbon fluxes in the extreme latitudes and can also potentially corroborate fossil fuel shifts, but such detection will require observations over extended time periods.

Overall, this dissertation has developed a geostatistical mapping method for CO_2 satellite observations and shown that maps of atmospheric CO_2 concentrations from satellite observations can be generated at high spatial and temporal resolution. These maps represent the atmospheric CO_2 concentrations accurately at synoptic time scales and have uncertainties that correctly describe the true uncertainty of the mapped

concentrations. This represents a significant improvement over current mapping approaches that rely on binning, which typically have monthly or lower temporal resolutions and lack uncertainties. Geostatistical mapping infers observation-derived mapping products based on spatial correlation without invoking carbon flux and atmospheric transport model assumptions. Given the large gaps and high measurement errors of the satellite observations, the choice of carbon flux and atmospheric transport model can easily dominate the resulting products in approaches that use such assumptions, and render them hence dependent on these choices. The geostatistical mapping products developed here are independent of any carbon flux and atmospheric transport assumptions, which is critical if the mapping products are used to validate, and conduct comparisons with, such models.

The resulting high resolution mapping products are a direct way to utilize the information content of the satellite observations to address some of the open questions in carbon cycle science. The mapping products can be used directly to understand the structure and regional and temporal variations of the atmospheric CO_2 concentration field and they can be used in intercomparison studies with carbon-cycle models to assess the consistency of these models with the satellite observations. The intercomparison conducted using GOSAT observations has shown that the mapping products provide some constraint to inform where and in which seasons models are not consistent with the information contained in the GOSAT observations. Such a comparison could not have been done in a spatially comprehensive way using the GOSAT observations directly, as individual GOSAT CO_2 observations feature many gaps and have very large uncertainties, which essentially preclude comparisons that could provide new insights. The developed mapping methodology has the ability to leverage the information content of many observations concurrently and to use the noisy gap-ridden observations to derive spatially continuous global concentration fields with comparatively lower uncertainties, which in turn enables more meaningful

comparisons. This ability was also vital to conduct the study to assess the expected contributions to carbon cycle science of the ASCENDS mission. More broadly, the ability to map at high spatial and temporal resolution is beneficial in a wide variety of studies, where independent data-driven high resolution CO_2 mapping products are of essence to gain new insights into the carbon cycle.

6.2 Future Work

The following paragraphs describe directions for future work resulting from the research conducted as part of this dissertation.

6.2.1 Extending GOSAT mapping and model comparison

Immediate future work includes extending the analysis of comparing the mapped GOSAT CO_2 observations to the PCTM/GEOS-5/CASA-GFED model presented in chapter III to three years by analyzing observations from July 2009 through June 2012. This a direct way to capitalize on the information content of the GOSAT CO_2 observations to inform carbon cycle science while doing so in a way that potential remaining problems in the retrieval algorithm such as regional biases [e.g. *Butz et al.*, 2011] will be noticeable. The proposed analysis uses the information from the satellite observations by assessing if the atmospheric CO_2 concentrations as predicted by the PCTM/GEOS-5/CASA-GFED model are consistent with the satellite observations.

Conducting this analysis will make it possible to investigate if and where seasonal areas of discrepancies are persistent over the three-year investigation period, or why the might vary due to interannual variabilities not fully captured in the model. The idea is that once these areas of discrepancies are identified, the potential sources of these discrepancies can be investigated and traced to their root causes by identifying which aspect of the model or retrieval algorithms leads to the discrepancies. These root causes could be on the retrieval or the modeling side. To correctly identify these

causes, this study should be conducted in collaboration with members of the modeling and the retrieval algorithm teams by getting input from both sides at progressing stages of the analysis. If the root causes are found to be on the retrieval side, this knowledge can be used to improve the underlying retrieval algorithm. On the model side, areas of discrepancies can point towards incorrectly modeled transport or carbon exchange processes that might be specified incorrectly in the model based on a lack of knowledge about the flux contribution of these processes.

There are many open question in carbon cycle science on the locations and magnitudes of carbon fluxes, and the underlying exchange processes driving them [e.g. *Michalak et al.*, 2011]. For example, the distribution of carbon sinks in the terrestrial biosphere has large uncertainties, and through a comparison study, such as the one proposed here, the information from the satellite observations can be used to assess if the carbon fluxes specified in the model result in predictions of atmospheric CO_2 concentrations that are consistent with the satellite observations. Persistent discrepancies and their seasonal evolution, which were identified as stemming from the model, can then be used to drill deeper and to identify which of the individual carbon exchange processes in the model of the terrestrial biosphere could have lead to the discrepancies. This can be approached by testing a range of possible specifications of the individual carbon exchange processes. This can ultimately result in both a better understanding of the carbon exchange processes and an improved representation of these processes in models. Based on the analysis conducted in chapter III, areas of special interest are the Amazon region and central Asia.

6.2.2 Comparison of CO_2 maps from different retrieval algorithms

Future work includes extending the application of the mapping and comparison methodology to comparisons of different retrievals of the same measurements of atmospheric CO_2 from GOSAT. The proposed work will provide a regional and seasonal

analysis of where, and to which degree, the retrieved CO_2 values differ. For GOSAT, there are currently at least three different retrieval algorithms in place [*Butz et al.*, 2011; *Crisp et al.*, 2012; *Yoshida et al.*, 2011]. They differ in the underlying modeling assumptions, e.g. which radiative transfer and spectroscopic models are employed, and lead to different retrieved CO_2 values, as well as difference in the spatial distribution, i.e. at which locations CO_2 values are retrieved varies as a function of the retrieval algorithm. Ultimately the products of these retrieval algorithms, the retrieved CO_2 concentrations, are intended to be used as inputs in further analyses to improve knowledge about the carbon cycle. Clearly, the findings from further analyses should be driven by the information content of the observations and ideally not depend on differences in retrieval algorithms. Comparing these products from different retrieval algorithms, and quantifying their regional and seasonal differences in a probabilistic way, is hence important for three main reasons: 1) It can provide guidance for improvement measures to the retrieval algorithm development teams, 2) it can guide the user of satellite CO_2 observations in their interpretation by identifying in which regions and seasons observations are most dependent on the choice of retrieval algorithm, and 3) as a further step, it can provide a quantitative measure to assess the uncertainty resulting from different retrieval algorithms.

By comparing maps, which are based on different retrieval algorithms, using the comparison methodology developed in Chapter V, regions where the resulting CO_2 concentrations differ significanlty can be identified. This can be done over the seasons, so such a comparison leads to an assessment of seasonally varying regional discrepancies based on different retrieval algorithms, which is crucial knowledge to the users of retrieved products. Mapping is well suited for such an application as it makes global comparisons at synoptic scales possible, which is not the case for comparisons of individual observations. Mapping brings individual observations into a spatially coherent framework, where the information content of all observations, also the ones

that are not collocated, is incorporated. It further does so without using any assumptions that could bias the comparison towards one retrieval algorithm, e.g. the same or similar a priori assumptions of the CO_2 concentration field. Mapping relies purely on assumptions about the existence of, and ability to infer, spatial correlation in the CO_2 concentration fields. Once the comparisons have been conducted, the knowledge of where, and in which seasons, regional discrepancies between retrieval algorithms exist, can guide the retrieval algorithm teams where to focus their attention to further develop and improve the retrieval algorithms.

Focusing on the user of retrieved CO_2 products, if the application of different retrieval algorithms leads to large differences in the observed values in certain regions and/or seasons, that indicates that caution should be used in the interpretation of observations in these locations and their use in subsequent modeling steps. One of the key motivations to obtain satellite observations of atmospheric CO_2 is to infer carbon fluxes globally at regional scales [e.g. *Crisp et al.*, 2004] to ultimately gain a better quantitative understanding of the underlying processes driving carbon exchange. To do that, the atmospheric CO_2 observations are most commonly used in inversion models to infer fluxes. In this setup, to account for measurement and other errors, uncertainties are assigned to each observation. These uncertainties specify partially to which degree each observation influences the estimated carbon fluxes. When using satellite observations these uncertainties are typically obtained from internal measures of uncertainty as obtained from the retrieval algorithm. However, this measure does not cover the full uncertainty [e.g. *O'Dell et al.*, 2012]. One meaningful (and practical) way to account for a broader range of uncertainties would be by using systematic adjustments as a function of how consistent observations from different retrieval algorithms are regionally and seasonally. The analysis proposed here to compare products of different retrieval algorithm in a probabilistic framework would aid in defining these adjustments. Applying such adjustments would lead to

carbon flux estimates from inversion studies that are less sensitive to the choice of retrieval algorithm.

6.2.3 Mapping using other spatial statistical approaches

The mapping methodology for atmospheric CO_2 observations developed in this dissertation can potentially be improved by using a mapping methodology that can incorporate temporal covariances to benefit from the information content of satellite observations from time periods before and after the mapping period, that would allow for scaling (i.e. change of spatial support), and would be based on a globally valid covariance model. These are all limitations of the methodology developed in this dissertation. The key question is if alleviating some or all of these limitations would indeed lead to improved CO_2 satellite mapping products. Improvement in this context is defined as resulting in better prediction accuracies and lower, but still realistic, uncertainties. It seems likely that such an improved methodology would still come from the area of spatial statistics, a field within statistics that has advanced significantly over the last decade, especially regarding the development of models that are applicable to large data sets such as satellite observations of CO_2. Characteristics need to include that the methodology is applicable to large data sets and valid globally, i.e. have support on the sphere. Methodologies with these characteristics have been developed, among others, by *Stein* [2008], *Jun and Stein* [2008], and *Cressie and Johannesson* [2008]. One of these spatial statistical models, and different variants of it, has been specifically applied to map satellite observations of CO_2 [e.g. *Katzfuss and Cressie*, 2012]. However, these applications were limited to example cases and were not focused on answering carbon cycle science questions, nor has the mapping performance been assessed for realistic scenarios for different seasons and under varying conditions.

Future work includes identifying which of existing spatial statistical methodologies

are best suited for mapping satellite CO_2 observations and to adapt, modify or further develop these methodologies to optimize their mapping performance given the specific characteristics of satellite CO_2 observations. As a next step the mapping performance of a candidate to represent an improved methodology needs to be assessed rigorously in terms of prediction accuracies and uncertainties for realistic conditions and for different satellites. The overall goal is to advance mapping methodologies for satellite CO_2 observations such that the mapping products have improved accuracies and uncertainties and/or spatial and temporal resolutions, which would make them more valuable tools to answer carbon cycle questions.

APPENDIX

APPENDIX A

Auxiliary Figures

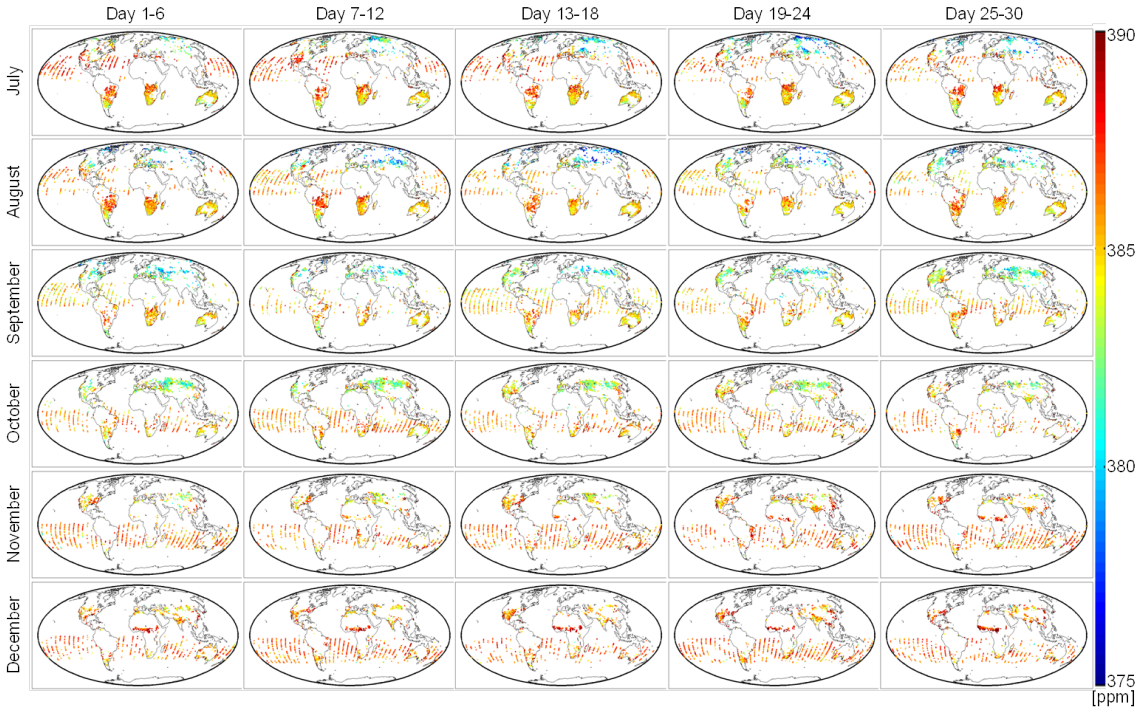

Figure A.1: ACOS X_{CO_2} Level 2 observations for 6-day periods from July through December 2009.

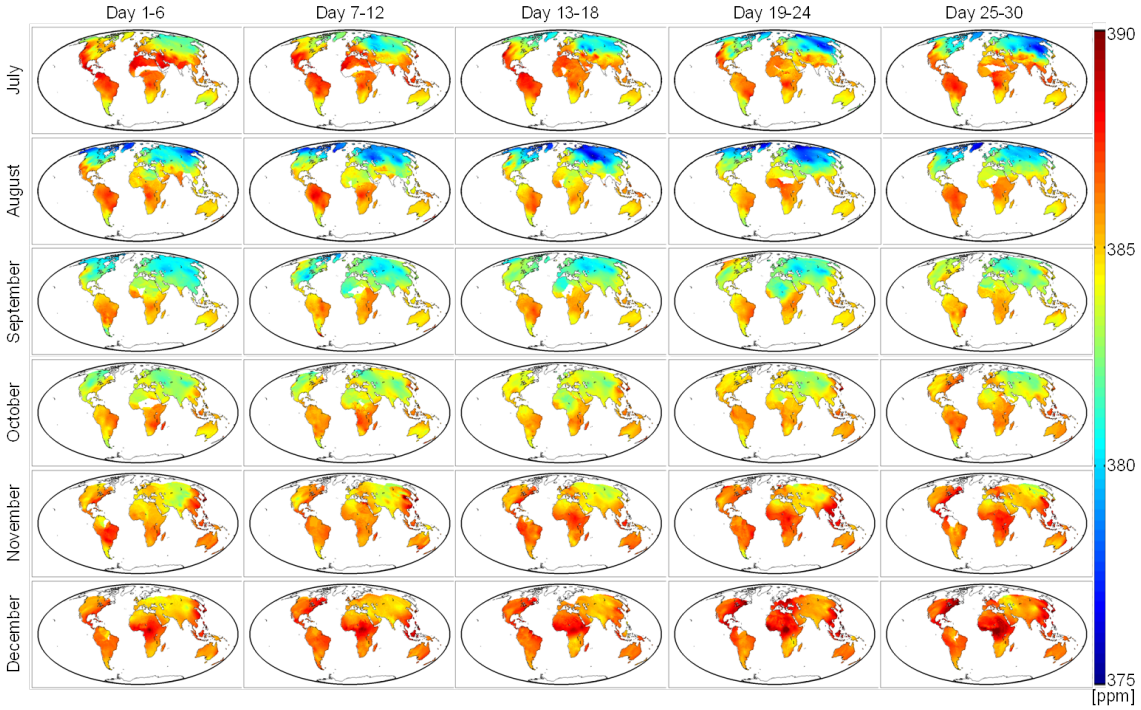

Figure A.2: ACOS X_{CO_2} Level 3 predictions for 6-day periods from July through December 2009.

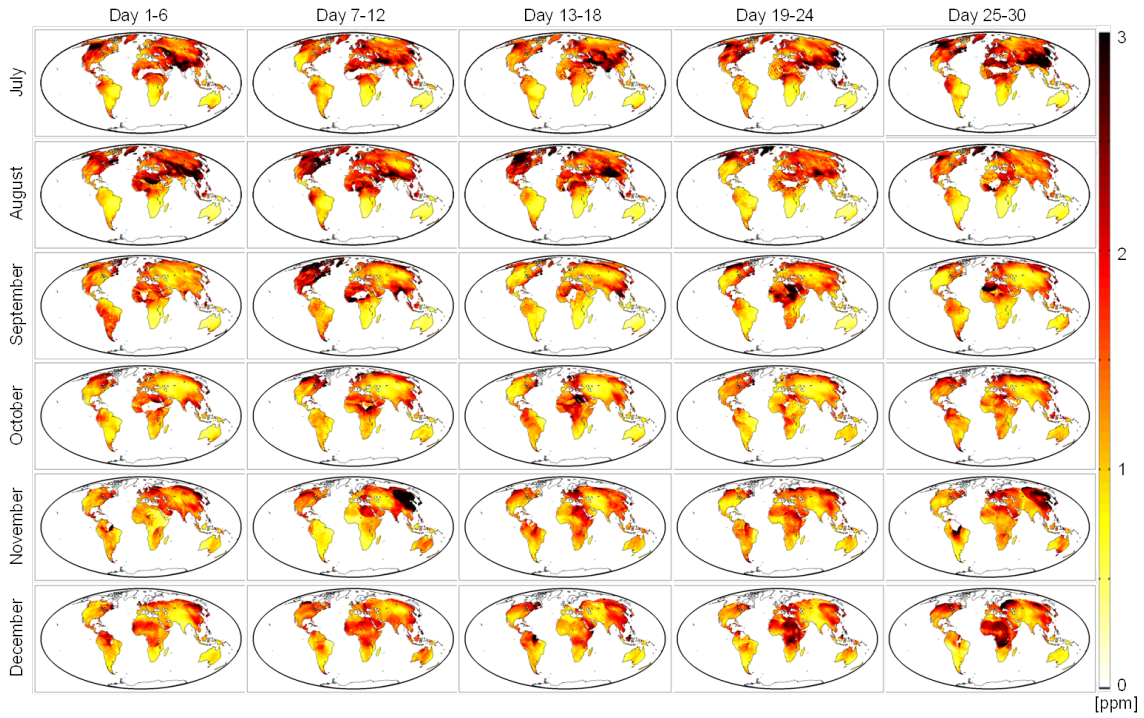

Figure A.3: ACOS X_{CO_2} Level 3 prediction uncertainties expressed as standard deviation for 6-day periods from July through December 2009.

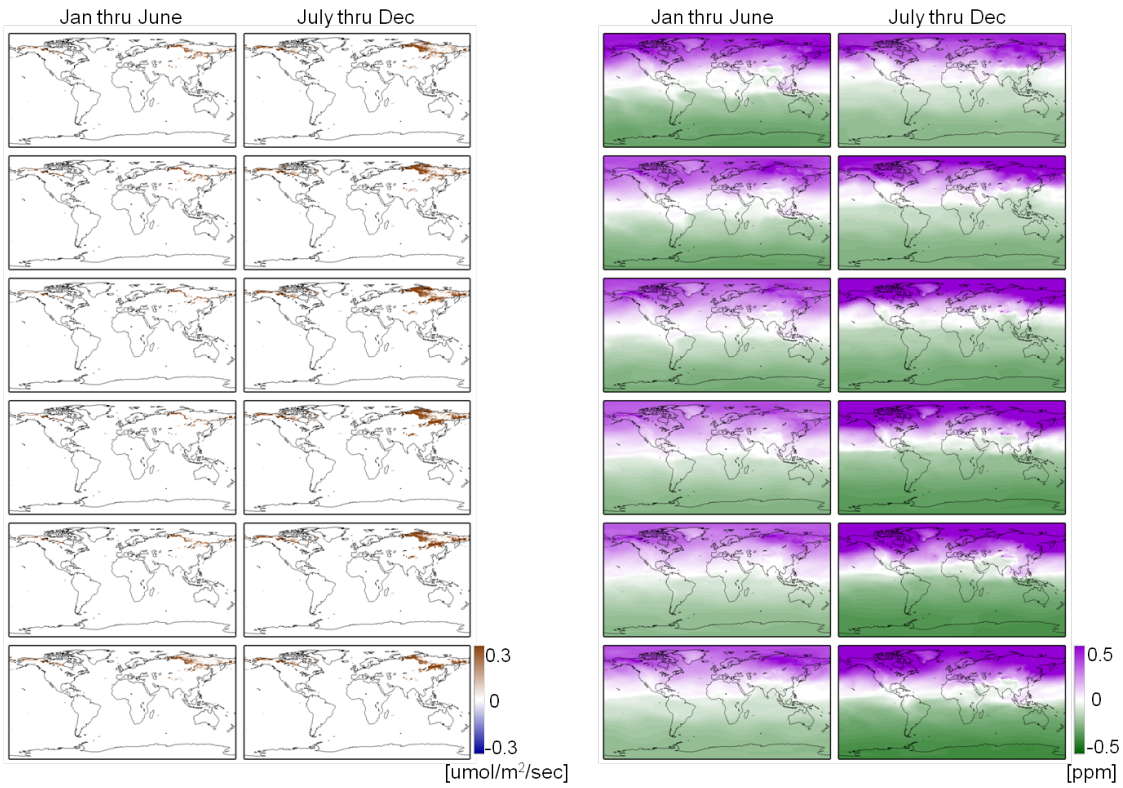

Figure A.4: Year-round monthly fluxes and atmospheric CO_2 concentrations for the permafrost carbon release experiment.

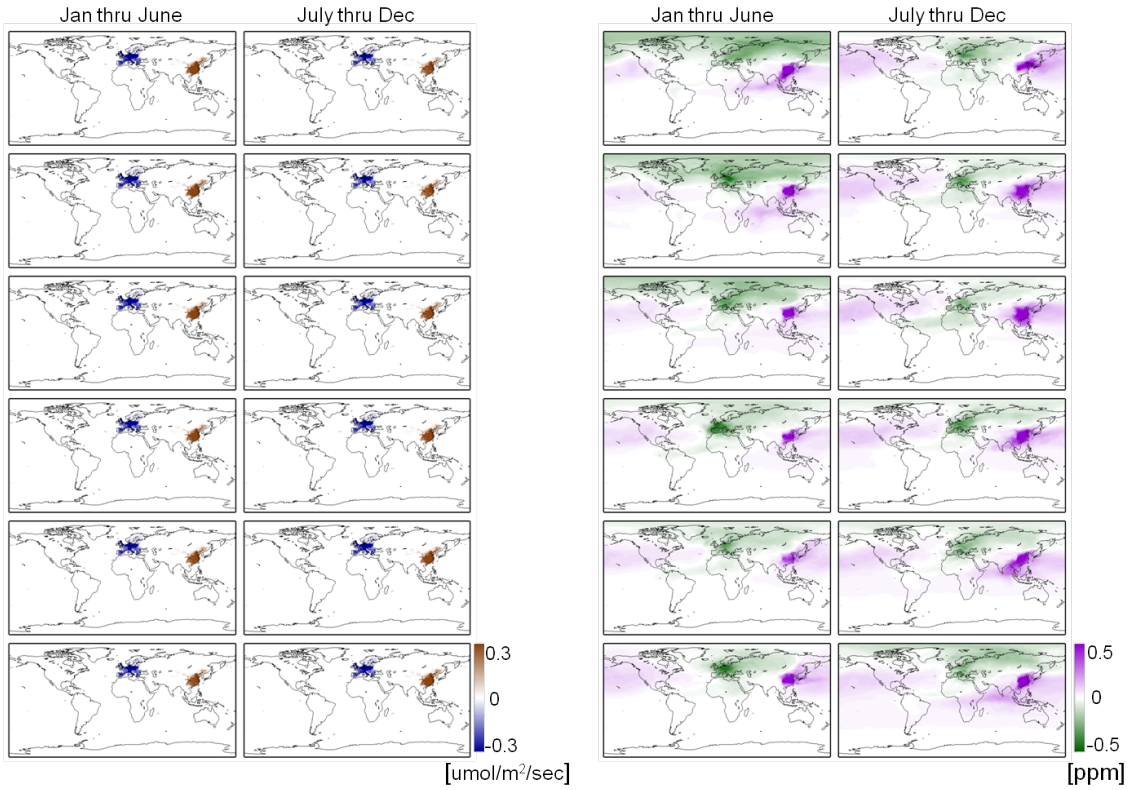

Figure A.5: Year-round monthly fluxes and atmospheric CO_2 concentrations for the higher signal fossil fuel experiment.

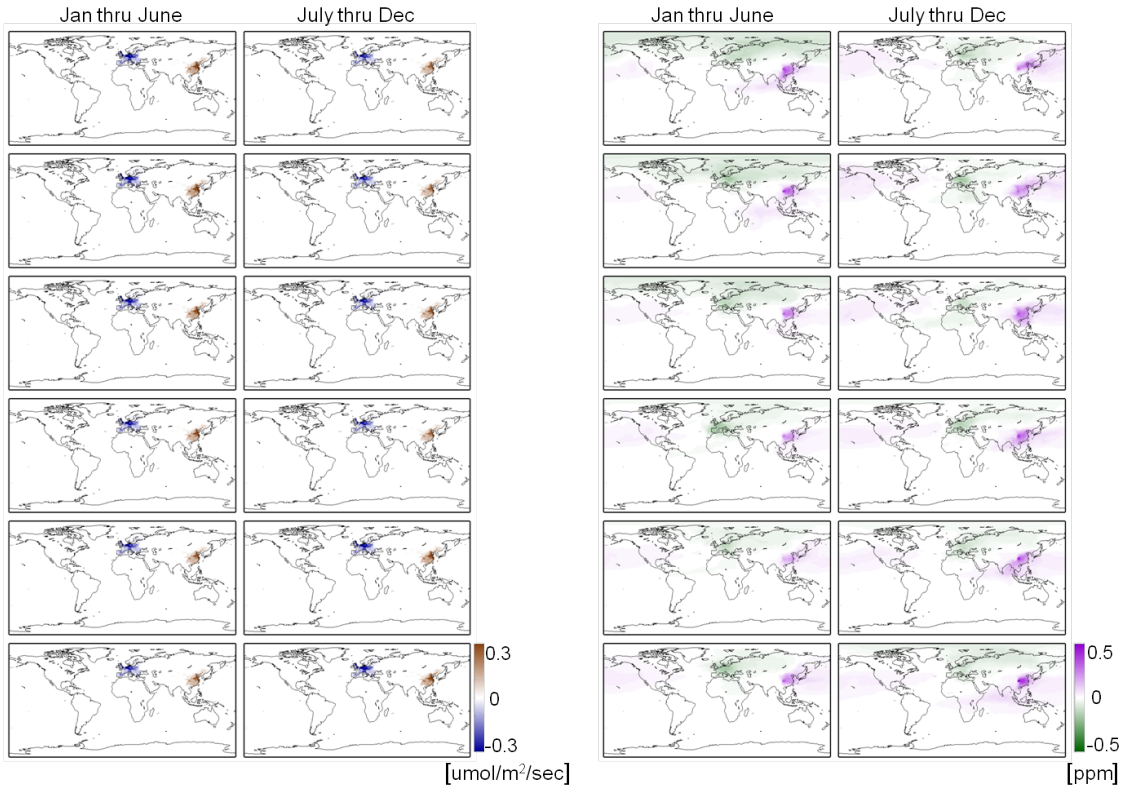

Figure A.6: Year-round monthly fluxes and atmospheric CO_2 concentrations for the lower signal fossil fuel experiment.

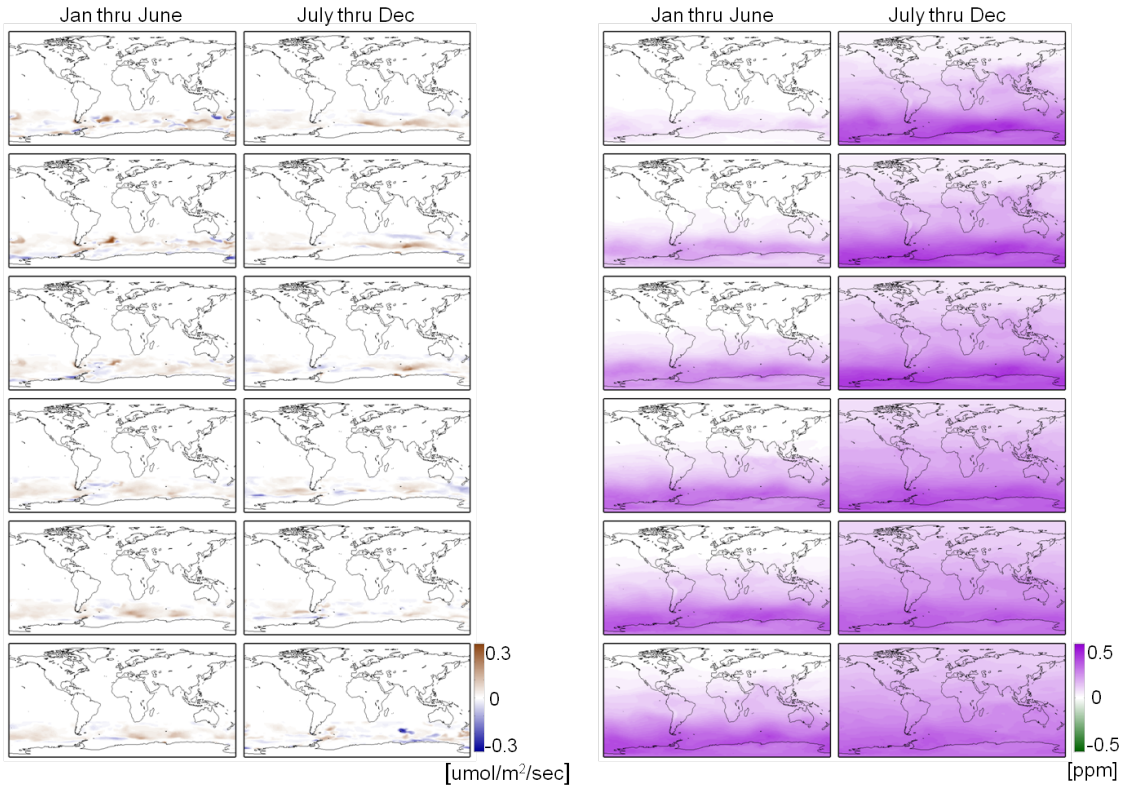

Figure A.7: Year-round monthly fluxes and atmospheric CO_2 concentrations for the Southern Ocean experiment.

BIBLIOGRAPHY

BIBLIOGRAPHY

Abshire, J. B., H. Riris, G. R. Allan, C. J. Weaver, J. Mao, X. Sun, W. E. Hasselbrack, S. R. Kawa, and S. Biraud (2010), Pulsed airborne lidar measurements of atmospheric CO_2 column absorption, *Tellus B*, *62*(5), 770–783.

Alkhaled, A., A. M. Michalak, S. R. Kawa, S. Olsen, and J.-W. Wang (2008), A global evaluation of the regional spatial variability of column integrated CO_2 distributions, *J. Geophys. Res.*, *113*, D20303.

American Meteorological Society (2012), Climate change: An information statement of the American Meteorological Society.

Andres, R. J., T. A. Boden, and G. Marland (2009), Monthly fossil-fuel CO_2 emissions: Mass of emissions gridded by one degree latitude by one degree longitude, Carbon Dioxide Information Analysis Center, Environmental Sciences Division, Oak Ridge National Laboratory, Oak Ridge, TN.

Andres, R. J., J. S. Gregg, I. Losey, G. Marland, and T. A. Boden (2011), Monthly, global emissions of carbon dioxide from fossil fuel consumption, *Tellus B*, *63*(3), 309–327.

ASCENDS Workshop Steering Committee (2008), Active Sensing of CO_2 Emissions over Nights, Days, and Seasons (ASCENDS), Mission NASA Science Definition and Planning Workshop Report.

Aumann, H., and D. G. S. Gaiser (2005), Airs hyper-spectral measurements for climate research: Carbon dioxide and nitrous oxide effects, *Geophys. Res. Lett.*, *32*(5).

Baker, D. F., H. Bösch, S. C. Doney, D. M. O'Brien, and D. S. Schimel (2010), Carbon source/sink information provided by column CO_2 measurements from the Orbiting Carbon Observatory, *Atmos. Chem. Phys.*, *10*(9), 4145.

Baker, D. F., et al. (2006), Transcom 3 inversion intercomparison: Impact of transport model errors on the interannual variability of regional CO_2 fluxes, 1988-2003, *Global Biogeochem. Cycles*, *20*.

Banerjee, S., B. P. Carlin, and A. E. Gelfand (2004), *Hierarchical modeling and analysis for spatial data*, 452 pp., Chapman & Hall/CRC, Boca Raton, FL.

Battin, T. J., S. Luyssaert, L. A. Kaplan, A. K. Aufdenkampe, A. Richter, and L. J. Tranvik (2009), The boundless carbon cycle, *Nature Geosci.*, *2*(9), 598–600.

Bian, H., S. R. Kawa, M. Chin, S. Pawson, Z. Zhu, P. Rasch, and S. Wu (2006), A test of sensitivity to convective transport in a global atmospheric CO_2 simulation, *Tellus B*, *58*(5), 463–475.

Blunden, J., and D. S. Arndt (2012), State of the climate in 2011, *Bull. Amer. Meteor. Soc.*, *93*(7), S1–S264.

Boland, S., et al. (2009), The need for atmospheric carbon dioxide measurements from space : Contributions from a rapid reflight of the Orbiting Carbon Observatory, Technical Report, OCO Science Team, NASA Jet Propulsion Labaratory.

Buchwitz, M., O. Schneising, J. P. Burrows, H. Bovensmann, M. Reuter, and J. Notholt (2007), First direct observation of the atmospheric CO_2 year-to-year increase from space, *Atmos. Chem. Phys.*, *7*, 4249–4256.

Butz, A., et al. (2011), Toward accurate CO_2 and CH_4 observations from GOSAT, *Geophys. Res. Lett.*, *38*(14).

Canadell, J., D. Pataki, R. Gifford, R. Houghton, Y. Lou, M. Raupach, P. Smith, and W. Steffen (2007a), Saturation of the terrestrial carbon sink, in *Terrestrial Ecosystems in a Changing World*, edited by J. Canadell, D. Pataki, and L. Pitelka, pp. 59–78, Cambridge Univ. Press, Cambridge, UK.

Canadell, J. G., et al. (2007b), Contributions to accelerating atmospheric CO_2 growth from economic activity, carbon intensity, and efficiency of natural sinks, *PNAS*, *104*(47).

Canadell, J. G., et al. (2010), Carbon sciences for a new world, *Current Opinion in Environmental Sustainability*, *2*(209).

Chahine, M., L. Chen, P. Dimotakis, X. Jiang, Q. Li, E. T. Olsen, T. Pagano, J. Randerson, and Y. L. Yung (2008), Satellite remote sounding of mid-tropospheric CO_2, *J. Geophys. Res.*, *35*, L17807.

Chen, L., M. Fuentes, and J. Davis (2006), Spatial-temporal statistical modeling and prediction of environmental processes, in *Hierarchical Modelling for the Environmental Sciences: Statistical Methods and Applications*, edited by J. S. Clark and A. E. Gelfand, pp. 121–144, Oxford Univ. Press, New York.

Chevallier, F., R. J. Engelen, C. Carouge, T. J. Conway, P. Peylin, C. Pickett-Heaps, M. Ramonet, P. J. Rayner, and I. Xueref-Remy (2009), AIRS-based versus flask-based estimation of carbon surface fluxes, *J. Geophys. Res.*, *114*, doi: 10.1029/2009JD012311, D20303.

Chevallier, F., et al. (2011), Global CO_2 fluxes inferred from surface air-sample measurements and from TCCON retrievals of the CO_2 total column, *Geophys. Res. Lett.*, *38*(24), 1–5, doi:10.1029/2011GL049899.

Chiles, J.-P., and P. Delfiner (1999), *Geostatistics: Modeling Spatial Uncertainty*, 695 pp., J. Wiley, New York.

Clark, J. S., and A. E. Gelfand (2006), *Hierarchical modelling for the environmental sciences: statistical methods and applications*, 205 pp., Oxford Univ. Press, New York.

Committee on Methods for Estimating Greenhouse Gas Emissions, National Research Council (2010), Verifying greenhouse gas emissions: Methods to support international climate agreements.

Cressie, N. A. C. (1993), *Statistics for Spatial Data*, rev. ed., 900 pp., J. Wiley, New York.

Cressie, N. A. C., and G. Johannesson (2008), Fixed rank kriging for very large spatial data sets, *J. Royal Stat. Soc.: Ser. B (Stat. Method.)*, *70*(1), 209–226.

Crevoisier, C., S. Heilliette, A. Chédin, S. Serrar, R. Armante, and N. A. Scott (2004), Midtropospheric CO_2 concentration retrieval from airs observations in the tropics, *Geophys. Res. Letters*, *31*(17), L17106.

Crevoisier, C., A. Chédin, H. Matsueda, T. Machida, R. Armante, and N. A. Scott (2009), First year of upper tropospheric integrated content of CO_2 from IASI hyperspectral infrared observations, *Atmos. Chem. Phys.*, *9*(14), 4797–4810.

Crisp, D., et al. (2004), The Orbiting Carbon Observatory (OCO) mission, *Adv. Space Res.*, *34*(4), 700–709.

Crisp, D., et al. (2012), The ACOS CO_2 retrieval algorithm—Part II: Global X_{CO_2} data characterization, *Atmos. Meas. Tech.*, *5*(4), 687–707.

Denman, K., et al. (2007), Couplings between changes in the climate system and biogeochemistry., in *Climate Change 2007: The physical science basis: Contribution of Working Group I to the Fourth Assessment Report of the Intergovernmental Panel on Climate Change*, edited by S. Solomon, D. Qin, M. Manning, Z. Chen, M. Marquis, K. Averyt, M. Tignor, and H. Miller, Cambridge Univ. Press, Cambridge, UK.

Disney, M. I., P. E. Lewis, M. Bouvet, A. Prieto-Blanco, and S. Hancock (2009), Quantifying surface reflectivity for spaceborne lidar via two independent methods, *IEEE Transactions on Geoscience and Remote Sensing*, *47*(9), 3262–3271.

Doney, S. C., I. Lima, R. A. Feely, D. M. Glover, K. Lindsay, N. Mahowald, J. K. Moore, and R. Wanninkhof (2009), Mechanisms governing interannual variability in upper-ocean inorganic carbon system and air-sea CO_2 fluxes: Physical climate and atmospheric dust, *Deep Sea Research Part II: Topical Studies in Oceanography*, *56*(8-10), 640–655.

Ehret, G., C. Kiemle, M. Wirth, A. Amediek, A. Fix, and S. Houweling (2008), Space-borne remote sensing of CO_2, CH_4, and N_2O by integrated path differential absorption lidar: a sensitivity analysis, *Appl. Phys. B: Lasers and Optics*, *90*, 593–608.

Engelen, R. J., A. Denning, and K. Gurney (2002), On error estimation in atmospheric CO_2 inversions, *J. Geophys. Res.*, *107*, 4635.

Engelen, R. J., S. Serrar, and F. Chevallier (2009), Four-dimensional data assimilation of atmospheric CO_2 using AIRS observations, *J. Geophys. Res.*, *114*, D03303.

Enting, I. (2002), *Inverse Problems in Atmospheric Constituent Transport*, Cambridge Univ. Press, Cambridge, UK.

Feng, L., P. I. Palmer, H. Bösch, and S. Dance (2009), Estimating surface CO_2 fluxes from space-borne CO_2 dry air mole fraction observations using an ensemble Kalman filter, *Atmos. Chem. Phys.*, *9*(8), 2619–2633.

Field, C., J. Sarmiento, and B. Hales (2007), The carbon cycle of north america in a global context., in *The First State of the Carbon Cycle Report (SOCCR): The North American Carbon Budget and Implications for the Global Carbon Cycle. A Report by the U.S. Climate Change Science Program and the Subcommittee on Global Change Research*, edited by A. King, L. Dilling, G. Zimmerman, D. Fairman, R. Houghton, G. Marland, A. Rose, and T. Wilbanks, pp. 21–28, National Oceanic and Atmospheric Administration, National Climatic Data Center, Asheville, NC.

Field, C., V. Barros, T. Stocker, D. Qin, K. Mach, G.-K. Plattner, M. Mastrandrea, M. Tignor, and K.L. Ebi (Eds.) (2011), *IPCC 2011: Workshop Report of the Intergovernmental Panel on Climate Change Workshop on Impacts of Ocean Acidification on Marine Biology and Ecosystems*, 164 pp., Working Group II Technical Support Unit, Carnegie Institution, Stanford, CA.

Forster, P., et al. (2007), Changes in atmospheric constituents and in radiative forcing, in *Climate Change 2007: The physical science basis: Contribution of Working Group I to the Fourth Assessment Report of the Intergovernmental Panel on Climate Change*, edited by S. Solomon, D. Qin, M. Manning, Z. Chen, M. Marquis, K. Averyt, M. Tignor, and H. Miller, pp. 129–234, Cambridge Univ. Press, Cambridge, UK.

Friedlingstein, P., et al. (2006), Climate-carbon cycle feedback analysis: Results from the C4MIP model intercomparison, *J. Clim.*, *19*(14), 3337–3353.

Gelfand, A. E. (2010), *Handbook of Spatial Statistics*, 607 pp., CRC Press, Boca Raton, Fla.

Gourdji, S. M., et al. (2012), North American CO_2: inter-comparison of modeled estimates with results from a fine-scale atmospheric inversion, *Biogeosciences*, *9*(1), 457–475, doi:10.5194/bg-9-457-2012.

Gruber, N., et al. (2009), Oceanic sources, sinks, and transport of atmospheric CO_2, *Global Biogeochem. Cycles*, *23*.

Gurney, K. R., D. F. Baker, P. J. Rayner, and A. S. Denning (2008), Interannual variations in continental-scale net carbon exchange and sensitivity to observing networks estimated from atmospheric CO_2 inversions for the period 1980 to 2005, *Global Biogeochemical Cycles*, *22*.

Gurney, K. R., et al. (2003), TransCom 3 CO_2 inversion intercomparison: 1. Annual mean control results and sensitivity to transport and prior flux information, *Tellus B*, *55*, 555–579.

Haas, T. C. (1990), Kriging and automated variogram modeling within a moving window, *Atmos. Environ., Part A*, *24*(7), 1759–1769.

Hamazaki, T., Y. Kaneko, and A. Kuze (2004), Carbon dioxide monitoring from the GOSAT satellite, paper presented at the XXth ISPRS Conference, ISPRS, Istanbul, Turkey.

Hammerling, D. M., A. M. Michalak, and S. R. Kawa (2012), Mapping of CO_2 at high spatiotemporal resolution using satellite observations: Global distributions from OCO-2, *J. Geophys. Res.*, *117*, D06306.

Heimann, M. (2009), Searching out the sinks, *Nat. Geosci.*, *2*(1), 3–4.

Higdon, D. M., J. Swall, and J. Kern (1998), Non-stationary spatial modelling, Oxford Univ. Press.

Houweling, S., et al. (2010), The importance of transport model uncertainties for the estimation of CO_2 sources and sinks using satellite measurements, *Atmos. Chem. Phys.*, *10*(20), 9981–9992.

Hu, Y., et al. (2008), Sea surface wind speed estimation from space-based lidar measurements, *Atmos. Chem. Phys.*, *8*(13), 3593–3601.

Huang, C., H. Zhang, and S. Robeson (2009), On the validity of commonly used covariance and variogram functions on the sphere, *Math. Geosci.*, *43*(6), 721–733.

Hungershoefer, K., F.-M. Breon, P. Peylin, F. Chevallier, P. Rayner, A. Klonecki, S. Houweling, and J. Marshall (2010), Evaluation of various observing systems for the global monitoring of co_2 surface fluxes, *Atmos. Chem. Phys.*, *10*(21), 10,503–10,520.

Huntzinger, D., et al. (2012), North American Carbon Program (NACP) regional interim synthesis: Terrestrial biospheric model intercomparison, *Ecological Modelling*, *232*, 144–157.

IPCC (2007), Summary for policymakers, in *Climate Change 2007: The physical science basis: Contribution of Working Group I to the Fourth Assessment Report of the Intergovernmental Panel on Climate Change*, edited by S. Solomon, D. Qin, M. Manning, Z. Chen, M. Marquis, K. Averyt, M. Tignor, and H. Miller, Cambridge Univ. Press, Cambridge, UK.

Jun, M., and M. L. Stein (2008), Nonstationary covariance models for global data, *Ann. Appl. Stat.*, *2*(4), 1271–1289.

Katzfuss, M., and N. Cressie (2012), Bayesian hierarchical spatio-temporal smoothing for massive datasets, *Environmetrics*, *23*, 94–107.

Kawa, S. R., D. J. Erickson III, S. Pawson, and Z. Zhu (2004), Global CO_2 transport simulations using meteorological data from the NASA data assimilation system, *J. Geophys. Res.*, *109*, D18312.

Kawa, S. R., J. Mao, J. B. Abshire, G. J. Collatz, X. Sun, and C. J. Weaver (2010), Simulation studies for a space-based CO_2 lidar mission, *Tellus B*, *62*(5).

Keeling, C., R. Bacastow, A. Bainbridge, C. Ekdahl, P. Guenther, and L. Waterman (1976), Atmospheric carbon dioxide variations at Mauna Loa Observatory, Hawaii, *Tellus*, *28*, 538–551.

King, A., L. Dilling, G. Zimmerman, D. Fairman, R. Houghton, G. Marland, A. Rose, and T. Wilbanks (2004), Current status and past trends of the global carbon cycle, in *The global carbon cycle: integrating humans, climate and the natural world*, edited by C. B. Field and M. R. Raupach, pp. 17–44, Island Press, Washington, DC, USA.

King, A., L. Dilling, G. Zimmerman, D. Fairman, R. Houghton, G. Marland, A. Rose, and T. Wilbanks (2007), What is the carbon cycle and why care?, in *The First State of the Carbon Cycle Report (SOCCR): The North American Carbon Budget and Implications for the Global Carbon Cycle. A Report by the U.S. Climate Change Science Program and the Subcommittee on Global Change Research*, edited by A. King, L. Dilling, G. Zimmerman, D. Fairman, R. Houghton, G. Marland, A. Rose, and T. Wilbanks, pp. 15–20, National Oceanic and Atmospheric Administration, National Climatic Data Center, Asheville, NC.

Kitanidis, P. K. (1997), *Introduction to Geostatistics: Applications to Hydrogeology*, 249 pp., Cambridge Univ. Press, New York.

Kulawik, S. S., et al. (2010), Characterization of Tropospheric Emission Spectrometer (TES) CO_2 for carbon cycle science, *Atmos. Chem. Phys.*, *10*(12), 5601–5623.

Kuze, A., H. Suto, M. Nakajima, and T. Hamazaki (2009), Thermal and near infrared sensor for carbon observation Fourier-transform spectrometer on the Greenhouse Gases Observing Satellite for greenhouse gases monitoring, *Appl. Opt.*, *48*, 6716–6733.

Law, R. M., R. J. Matear, and R. J. Francey (2008a), Comment on "Saturation of the Southern Ocean CO_2 sink due to recent climate change", *Science*, *319*(5863), 570.

Law, R. M., et al. (2008b), TransCom model simulations of hourly atmospheric CO_2: Experimental overview and diurnal cycle results for 2002, *Global Biogeochem. Cycles*, *22*(3), GB3009.

Le Quéré, C., M. R. Raupach, J. G. Canadell, and et al Marland (2009), Trends in the sources and sinks of carbon dioxide, *Nature Geosci.*, *2*(12), 831–836.

Le Quéré, C., et al. (2007), Saturation of the southern ocean CO_2 sink due to recent climate change, *Science*, *316*(5832), 1735–1738.

L'Ecuyer, T., and J. Jiang (2010), Touring the atmosphere aboard the A-Train, *Phys. Today*, *63*(7), 36.

Lemke, P., et al. (2007), Changes in snow, ice and frozen ground, in *Climate Change 2007: The physical science basis: Contribution of Working Group I to the Fourth Assessment Report of the Intergovernmental Panel on Climate Change*, edited by S. Solomon, D. Qin, M. Manning, Z. Chen, M. Marquis, K. Averyt, M. Tignor, and H. Miller, Cambridge Univ. Press, Cambridge, UK.

Machida, T., et al. (2008), Worldwide measurements of atmospheric coother trace gas species using commercial airlines, *J. Atmos. Oceanic. Technol.*, *25*(10), 1744–1754.

Mao, J., and S. R. Kawa (2004), Sensitivity Study for Space-based Measurement of Atmospheric Total Column Carbon Dioxide by Reflected Sunlight, *Appl. Opt.*, *43*, 914927.

Meredith, M. P., A. C. N. Garabato, A. M. Hogg, and R. Farneti (2012), Sensitivity of the Overturning Circulation in the Southern Ocean to Decadal Changes in Wind Forcing, *J. Climate*, *25*(1), 99–110.

Michalak, A., L. Bruhwiler, and P. Tans (2004), A geostatistical appraoch to surface flux estimation of atmospheric trace gases, *J. Geophys. Res.*, *109*, D14109.

Michalak, A., R. Jackson, G. Marland, C. Sabine, and the Carbon Cycle Science Working Group (2011), *A U.S. Carbon Cycle Science Plan*, 69 pp., University Cooperation for Atmospheric Research.

Nassar, R., et al. (2011), Inverse modeling of CO_2 sources and sinks using satellite observations of CO_2 from TES and surface flask measurements, *Atmos. Chem. Phys.*, *11*(12), 6029–6047, doi:10.5194/acp-11-6029-2011.

National Research Council (2007), *Earth Science and Applications from Space: National Imperatives for the Next Decade and Beyond*, 456 pp., The National Academies Press, Washington, DC 2001.

Nevison, C. D., N. M. Mahowald, S. C. Doney, I. D. Lima, G. R. van der Werf, J. T. Randerson, D. F. Baker, P. Kasibhatla, and G. A. McKinley (2008), Contribution of ocean, fossil fuel, land biosphere, and biomass burning carbon fluxes to seasonal and interannual variability in atmospheric CO_2, *J. Geophys. Res.*, *113*, G01010.

Nicholls, R.J., P. Wong, V. Burkett, J. Codignotto, J. Hay, R. McLean, S. Ragoonaden, and C. Woodroffe (2007), Coastal systems and low-lying areas, in *Climate Change 2007: Impacts, Adaptation and Vulnerability. Contribution of Working Group II to the Fourth Assessment Report of the Intergovernmental Panel on Climate Change*, edited by M. Parry, O. Canziani, J. Palutikof, P. van der Linden, and C. Hanson, Cambridge Univ. Press, Cambridge, UK.

Nisbet, E., and R. Weiss (2010), Top-down versus bottom-up, *Science*, *328*(5983), 1241–1243.

O'Dell, C. W., et al. (2012), The ACOS CO_2 retrieval algorithm—Part 1: Description and validation against synthetic observations, *Atmos. Meas. Tech.*, *5*(1), 99–121.

Olivier, J., G. Janssens-Maenhout, and J. Peters (2012), *Trends in global CO_2 emissions; 2012 Report*, PBL Netherlands Environmental Assessment Agency; Ispra: Joint Research Centre, The Hague, Netherlands.

Olsen, S. C., and J. T. Randerson (2004), Differences between surface and column atmospheric CO_2 and implications for carbon cycle research, *J. Geophys. Res.*, *109*, D02301.

Pacala, S., et al. (2007a), Eddy-covariance measurements now confirm estimates of carbon sinks from forest inventories, in *The First State of the Carbon Cycle Report (SOCCR): The North American Carbon Budget and Implications for the Global Carbon Cycle. A Report by the U.S. Climate Change Science Program and the Subcommittee on Global Change Research*, edited by A. King, L. Dilling, G. Zimmerman, D. Fairman, R. Houghton, G. Marland, A. Rose, and T. Wilbanks, pp. 169–170, National Oceanic and Atmospheric Administration, National Climatic Data Center, Asheville, NC.

Pacala, S., et al. (2007b), The North American carbon budget past and present, in *The First State of the Carbon Cycle Report (SOCCR): The North American Carbon Budget and Implications for the Global Carbon Cycle. A Report by the U.S. Climate Change Science Program and the Subcommittee on Global Change Research*, edited by A. King, L. Dilling, G. Zimmerman, D. Fairman, R. Houghton, G. Marland, A. Rose, and T. Wilbanks, pp. 29–36, National Oceanic and Atmospheric Administration, National Climatic Data Center, Asheville, NC.

Parazoo, N. C., A. S. Denning, S. R. Kawa, K. D. Corbin, R. S. Lokupitiya, and I. T. Baker (2008), Mechanisms for synoptic variations of atmospheric CO_2 in North America, South America and Europe, *Atmos. Chem. Phys.*, *8*(23), 7239–7254.

Peters, G., G. M. G, C. L. Qur, T. Boden, J. G. Canadell, and M. Raupach (2011), Rapid growth in CO_2 emissions after the 2008-2009 global financial crisis, *Nature Climate Change*, *2*, 2–4.

Prentice, I., et al. (2001), The carbon cycle and atmospheric carbon dioxide, in *Climate Change 2001: The Scientific Basis. Contribution of Working Group I to the Third Assessment Report of the Intergovernmental Panel on Climate Change*, edited by J. T. Houghton, Y. Ding, D. J. Griggs, M. Noguer, P. J. der Linden, X. Dai, K. Maskell, and C. A. Johnson, pp. 183–237, Cambridge Univ. Press, Cambridge, UK.

Randerson, J. T., M. V. Thompson, C. M. Malmstrom, C. B. Field, and I. Y. Fung (1996), Substrate limitations for heterotrophs: Implications for models that estimate the seasonal cycle of atmospheric CO_2, *Global Biogeochem. Cycles*, *10*(4), 585–602.

Rienecker, M. M., et al. (2011), Merra: NASA's modern-era retrospective analysis for research and applications, *J. Climate*, *24*(14), 3624–3648.

Sampson, P. D., and P. Guttorp (1992), Nonparametric estimation of nonstationary spatial covariance structure, *J. Amer. Stat. Assoc.*, *87*(417), 108–119.

Schaaf, C. B., et al. (2002), First operational BRDF, albedo nadir reflectance products from modis, *Remote Sensing of Environment*, *83*(12), 135–148.

Schaeffer, K., T. Zhang, L. Bruhwiler, and A. P. Barrett (2011), Amount and timing of permafrost carbon release in response to climate warming, *Tellus B*, *63*(2), 165–180.

Schneising, O., M. Buchwitz, J. P. Burrows, H. Bovensmann, M. Reuter, J. Notholt, R. Macatangay, and T. Warneke (2008), Three years of greenhouse gas column-averaged dry air mole fractions retrieved from satellite—Part 1: Carbon dioxide, *Atmos. Chem. Phys.*, *8*(14), 3827–3853.

Schuh, A. E., A. S. Denning, K. D. Corbin, I. T. Baker, M. Uliasz, N. Parazoo, A. E. Andrews, and D. E. J. Worthy (2010), A regional high-resolution carbon flux inversion of North America for 2004, *Biogeosciences*, *7*(5), 1625–1644, doi: 10.5194/bg-7-1625-2010.

Solomon, S., D. Qin, M. Manning, Z. Chen, M. Marquis, K. B. Averyt, M. Tignor, and H. L. Miller (2007), *IPCC, 2007: Climate Change 2007: The Physical Science Basis. Contribution of Working Group I to the Fourth Assessment Report of the Intergovernmental Panel on Climate Change*, 996 pp., Cambridge Univ. Press, New York.

Spiers, G. D., R. T. Menzies, J. Jacob, L. E. Christensen, M. W. Phillips, Y. Choi, and E. V. Browell (2011), Atmospheric CO_2 measurements with a 2μm airborne laser absorption spectrometer employing coherent detection, *Appl. Opt.*, *50*(14), 2098–2111.

Stein, M. L. (1999), *Interpolation of Spatial Data: Some Theory for Kriging*, Springer, New York, NY.

Stein, M. L. (2005), Space-time covariance functions, *J. Amer. Stat. Assoc.*, *100*, 310–321.

Stein, M. L. (2008), A modeling approach for large spatial datasets, *J. Korean Stat. Soc.*, *37*(1), 3.

Stephens, B. B., et al. (2007), Weak northern and strong tropical land carbon uptake from vertical profiles of atmospheric CO_2, *Science*, *316*(5832), 1732–1735, doi: 10.1126/science.1137004.

Takahashi, T., et al. (2002), Global sea-air CO_2 flux based on climatological surface ocean pCO_2, and seasonal biological and temperature effects, *Deep Sea Research Part II: Topical Studies in Oceanography*, *49*(910), 1601–1622.

Tans, P. P., and T. J. Conway (2005), *Monthly Atmospheric CO_2 Mixing Ratios from the NOAA CMDL Carbon Cycle Cooperative Global Air Sampling Network, 1968–2002*, Trends: A Compendium of Data on Global Change. Carbon Dioxide Information Analysis Center, Oak Ridge National Laboratory, U.S. Department of Energy, Oak Ridge, TN.

Tarantola, A. (1987), *Inverse Problem Theory: Methods for Data Fitting and Model Parameter Estimation*, 630 pp., Elsevier, New York.

Thompson, D. R., et al. (2012), Atmospheric validation of high accuracy co_2 absorption coefficients for the OCO-2 mission, *J. Quantitative Spectroscopy and Radiative Transfer*, *113*(17), 2265–2276.

Tiwari, Y. K., M. Gloor, R. J. Engelen, F. Chevallier, C. Rödenbeck, S. Körner, P. Peylin, B. H. Braswell, and M. Heimann (2006), Comparing CO_2 retrieved from Atmospheric Infrared Sounder with model predictions: Implications for constraining surface fluxes and lower-to-upper troposphere transport, *J. Geophys. Res.*, *111*, D17106.

Trenberth, K., et al. (2007), Observations: Surface and atmospheric climate change, in *Climate Change 2007: The physical science basis: Contribution of Working Group I to the Fourth Assessment Report of the Intergovernmental Panel on Climate Change*, edited by S. Solomon, D. Qin, M. Manning, Z. Chen, M. Marquis, K. Averyt, M. Tignor, and H. Miller, Cambridge Univ. Press, Cambridge, UK.

van der Werf, G. R., et al. (2010), Global fire emissions and the contribution of deforestation, savanna, forest, agricultural, and peat fires (1997–2009), *Atmos. Chem. Phys.*, *10*(23), 11,707–11,735.

Wackernagel, H. (2003), *Multivariate Geostatistics: An Introduction with Applications*, 3rd ed., 387 pp., Springer, Berlin.

Winker, D. M., J. R. Pelon, and M. P. McCormick (2003), The CALIPSO mission: spaceborne lidar for observation of aerosols and clouds, *Lidar Remote Sensing for Industry and Environment Monitoring III*, *4893*(1), 1–11.

Yang, Z., R. A. Washenfelder, G. Keppel-Aleks, N. Y. Krakauer, J. T. Randerson, P. P. Tans, C. Sweeney, and P. O. Wennberg (2007), New constraints on Northern Hemisphere growing season net flux, *Geophys. Res. Lett.*, *34*(12), L12807.

Yokota, T., Y. Yoshida, N. Eguchi, Y. Ota, T. Tanaka, H. Watanabe, and S. Maksyutov (2009), Global Concentrations of CO_2 and CH_4 retrieved from GOSAT: First preliminary results, *SOLA*, *5*, 160–163.

Yoshida, Y., Y. Ota, N. Eguchi, N. Kikuchi, K. Nobuta, H. Tran, I. Morino, and T. Yokota (2011), Retrieval algorithm for CO_2 and CH_4 column abundances from short-wavelength infrared spectral observations by the greenhouse gases observing satellite, *Atmospheric Measurement Techniques*, *4*(4), 717–734.

Zhu, Z., and Y. Wu (2010), Estimation and prediction of a class of convolution-based spatial nonstationary models for large spatial data, *J. Comput. Graph. Stat.*, *19*(1), 74–95.